A STUDY OF d-He^4 ELASTIC SCATTERING

Thesis by

L. S. Senhouse, Jr.

In Partial Fulfillment of the Requirements

for the Degree of

Doctor of Philosophy

California Institute of Technology

Pasadena, California

1964

ACKNOWLEDGMENTS

The author is immensely grateful for the inspiration and guidance given him by Dr. Thomas A. Tombrello through the crucial part of this work. The author would, in addition, like to thank Professors Thomas Lauritsen and Charles A. Barnes for having suggested the problem and rendering assistance on many occasions. And finally, the author would like to extend his appreciation to the entire Kellogg staff and personnel and, in particular, to Dr. Peter D. M. Parker and Dr. Phillip A. Seeger for valuable help and suggestions throughout the duration of this project.

Paul E. Lloyd and Hughes Aircraft Company, in having supported the author by means of fellowships through his course of study, and the Office of Naval Research and the U. S. Atomic Energy Commission, in having supported the project, are all very much deserving of the accolades the author would hereby bestow.

ABSTRACT

Angular distributions ($17.97° \leq \theta_{c.m.} \leq 156.0°$) of $He^4(d,d)He^4$ have been obtained, using a gas scattering chamber, for deuteron bombarding energies from 2.935-11.475 MeV at half-MeV intervals. A lithium drifted solid-state detector was used to detect the scattered deuterons and recoil alpha particles. The phase shift and single level analyses performed with the data result in energy levels in Li^6 at excitation energies of $E_x = 4.57$, 4.62 and 7.19 MeV, and have respective J^π assignments of 2^+, 1^+ and 1^-. There is a great degree of confidence in the assignments for the first two levels; however, further analysis is necessary to confirm the assignments to the third level.

TABLE OF CONTENTS

TABLE OF CONTENTS (2)

I. INTRODUCTION

This study is an extension to higher energies of the investigation of the Li^6 nucleus by means of the $He^4(d,d)He^4$ reaction. This investigation was made possible through the use of the ONR EN Tandem Van de Graaff constructed by High Voltage Engineering Corporation.

The lowest unbound T= 0 level (Fig. 1) with spin, parity and excitation energy assignments of 3^+, $E_x = 2.184$ MeV was originally investigated by Lauritsen et al. (1953) and further confirmed by Galonsky et al. (1955). The levels studied in this experiment were the T = 0 levels with published assignments of spins, parities and excitation energies of (Ajzenberg-Selove and Lauritsen 1959)

1. 2^+; $E_x = 4.52$ MeV
2. 1^+; $E_x \approx 5.5$ MeV
3. ? ; $E_x = 7.4$ MeV

The existence of the first two levels was necessary in the single level parameterization made by Galonsky and McEllistrem (1955a) of data taken up to a center of mass excitation energy of 4.55 MeV. In that the data were taken essentially at the resonance energy of the first level, one would feel confident of level assignments of the first level. The energies of the first and third levels are obtained from the $Li^7(He^3,\alpha)Li^6$ reaction (Allen et al. 1960). The spectrum of this

reaction had rather salient peaks at the energies corresponding to the first and third levels and, therefore, one would expect these energy assignments to be reliable.

The assignments of the second level, however, remain to be confirmed, because this state does not appear strongly in the $Li^7(He^3,\alpha)Li^6$ experiment. The state was obtained from the alpha particle spectrum of the experiment after subtracting close-lying prominent levels (especially $E_x = 5.35$ MeV). The state was also inferred from the $He^4(d,d)He^4$ experiment (Galonsky et al. 1955) by the interpretation of data removed from the excitation energy of the level by an MeV.

There is, on the other hand, considerable evidence of a theoretical nature for the first two states. The states have resulted from intermediate coupling models by Inglis (1952, 1953) and Balashov (1959). The states have also resulted from the cluster model of Wildermuth et al. (1961) and the three-particle model of Wackman and Austern (1962).

The experimental investigation of these three levels was complicated by the existence of a three-particle reaction channel, which can proceed in one or more of three possible ways (Lauritsen and Ajzenberg-Selove 1962).

1. $He^4 + d \rightarrow He^5 + p \rightarrow He^4 + p + n$ $\quad Q_m = -3.182$ MeV

2. $He^4 + d \rightarrow Li^5 + n \rightarrow He^4 + p + n$ $\quad Q_m = -4.192$ MeV

3. $He^4 + d \rightarrow He^4 + p + n$ $\quad Q_m = -2.225$ MeV

There is reason to believe, from an analysis of the neutron yield (Lefevre et al. 1962), that the first two predominate, while the last probably involves the ^1S state for p + n (Rybakov et al. 1961), which would make the reaction isotopic spin forbidden. Further proof for the predominance of the first two and the absence of the third is found in the threshold for He^4(d, pn)He^4 being 0.4 MeV above the calculated threshold in the center of mass (Henkel et al. 1955) for the third reaction. The value for the total reaction cross-section is 0.3 ± 0.1 barn at an incident energy of 10.3 MeV for the deuterons (Allred et al. 1951).

This dissertation presents the reduction of the elastic scattering data as angular distributions and excitation curves after first discussing the design, construction, assembly and testing of the gas scattering chamber with which the data were obtained. Subsequently, the experimental cross-sections are compared with those of a phase shift analysis. The program used for this analysis appears in its entirety in Appendix G and is presented schematically in Figure 12. The program, in addition to performing a phase shift analysis, calculates tensor polarization parameters and values for the total reaction cross-section. Finally, a single level parameterization of the phase shifts yields single level parameters for the three levels investigated.

In addition to the intrinsic worth of an extension to higher energies of the investigation of the Li^6 nucleus by means of the $He^4(d,d)He^4$ reaction, this study performs other functions. It corroborates the angular distribution data taken on a cyclotron by Stewart et al. (1962) but disagrees with the 8.0 MeV data of Burge et al. (1952). Also, the analysis of the data enables one to investigate the usefulness of a phase shift analysis involving a large number of parameters at high energies. It might, in addition, be hoped that one day, in the not too distant future, a more comprehensive theory of the nucleus will evolve, imparting more meaning to this and the many other efforts that are continually being undertaken.

II. GAS SCATTERING CHAMBER

A. Design and Construction

Gas scattering chambers are found in the literature in two basic types: those that use foils to separate the target gas from the high vacuum in the beam tube and in the Faraday cup, and those that use differential pumping to maintain the pressure gradient between the high vacuum in the beam tube and the target gas, retaining the foil between the gas and the Faraday cup. The sizes of gas scattering chambers also vary; one of the largest in the literature has an inside diameter of 36 inches (Worthington et al. 1953), and one of the smallest used in a scattering experiment is about 3 inches with fixed angles of observation (Huntoon et al. 1940). The size of the scattering chamber is determined mainly by the detectors and by consideration of wall scattering. In this experiment, the decision was made to use solid state detectors, which are rather compact (7/8" O.D. x 1 mm. thick) in comparison to proportional counters (Worthington 1953). Furthermore, it was possible through the use of antiscattering slits in the detector collimators to shield from wall scattering, permitting the use of a chamber of only $11\frac{1}{2}$" inside diameter and yet retaining a detector with a continuously variable angular position.

The gas scattering chamber constructed for the present experiment is shown in Figure 2. A steel cylinder is provided with an entrance beam collimator (3) and a beam collector (16) located on a diameter. Located within the chamber are two detector assemblies (9) and (10), one fixed and the other (10) movable in angle. The entire chamber is filled with the scattering gas, and the scattering volume is defined by the beam collimator and the slit system attached to the detectors. Vacuum seals are effected by foils (2) and (12) at the entrance to the collimator and the collector respectively. The collector volume is connected by vacuum plumbing (not shown) to the main vacuum system of the beam tube.

The main body of the chamber is a welded fabrication made from 12" steel tubular stock with a bottom plate 1" thick. Electrical connections are brought into the vacuum through kovar glass-to-metal seals and O-rings are used as mechanical vacuum seals. The chamber has an entrance port in which the beam collimator is mounted, an exit port on which a Faraday cup is mounted, and a hole in the base for the rotating hub on which the adjustable platform is mounted. In addition, there are ports for evacuation, gas handling and impurity trapping.

The chamber was rough drilled, welded, and then stress relieved before the finish cuts on a milling machine. In this way, it was possible to hold the orthogonality of the center line of the entrance port to that of the detector platform to within $\pm$ 0.05°. Under normal operating

conditions, the chamber is separated from high vacuum by a 2500 Å or 5000 Å nickel entrance foil before the beam collimator and a 10,000 Å nickel exit foil before the Faraday cup. This enables one to maintain a gas pressure in the chamber of about 20 cm.-oil, while the high vacuum side is on the order of 10^{-6} mm. of Hg.

1. Beam Collimator

In order to provide an accurately collimated beam with a minimum of scattering, the beam collimator ((3) in Fig. 2) is provided with a series of disc apertures, made of .020" thick tantalum. The directionality of the collimator was insured by drilling and boring the inner dimensions for the apertures and then turning the outer chamber mating diameters concentric with the inside diameters. The apertures were first drilled, then mounted on small arbors for $\pm$ 0.001" concentric turning on the outer diameter. Six apertures are provided; two ((4) of Fig. 2) have 0.052" diameter holes and serve to define the beam; the remaining four have 0.0635" diameter holes and serve to stop scattered particles.

2. Faraday Cup

The beam collector cup ((12-16) in Fig. 2) is provided with a $\frac{1}{2}$" hole, sealed with a nickel foil. Graphical checks of the geometry by the method of Dickinson and Dodder (1953) indicated that less than 0.2% of the beam should be scattered to larger diameter than $\frac{1}{2}$", at the

highest helium pressure used. Charge collection is accomplished by an insulated cup ((16) in Fig. 2), which is provided with an electron suppression ring ((15) in Fig. 2). The collecting cup is maintained at +67½ V. with respect to the grounded chamber, and the suppressor at -300 V. Although the geometrical arrangement was by no means ideal, checks of a mock-up in an electrolytic bath indicated that with sufficient potential on the suppressor the system should be effective in stopping secondary electrons. Later checks with an alpha particle beam indicated that the suppression was not complete, and in the final runs, an Alnico magnet ((13) in Fig. 2) was added. With this arrangement, it is believed that the charge collection was accurate to better than 0.2%.

3. Foils

As previously noted, foils were used to isolate the scattering chamber from the main vacuum system. As compared with a differential pumping channel, foils introduce somewhat larger energy loss and straggling in the beam, but in view of the large breadth of the levels observed, this difference was of no importance. In order to permit easy replacement of the entrance foils, they were mounted in inserts in a modified plug shutoff valve, as shown in Figure 2 (1, 2).

The quarter-inch diameter of the orifice in the entrance-foil mount was determined by the diameter of the focused beam at that point. The half-inch diameter orifice in the exit-foil mount was decided on by considering the diameter of the multiply scattered beam. The gas

pressure of about 20 cm.-oil in the chamber was decided on by a consideration of energy loss in the gas and rate of the scattered-particle yield. With these constraints, the choice of 2500 Å or 5000 Å nickel entrance foils and 10,000 Å nickel exit foils proved suitable. From a strength consideration, even thinner foils could have been mounted at the entrance. However, thinner foils obtained from the supplier (Chromium Corporation of America) had an abnormal propensity for holes.

The mounts for the foils were deburred of sharp edges and were so designed that the pressure in the chamber would push the foils against their mounts. The reason for this is to reduce the possibility of insufficient adherence of the bonding agent, which in this case is solder. Solder was chosen because of its reliability and its ease of use as a bond. The foils were mounted by heating the mounts on a hot plate, tinning with the solder and affixing the foils.

The 5000 Å and 10,000 Å foils were self-supporting and consequently could be inspected for holes before mounting. The 2500 Å foil was not self-supporting, but was obtained from the supplier on an opaque copper backing. This backing was removed with a solution of equal parts trichloroacetic acid, ammonium hydroxide and water. Upon removal of the backing, a flashlight was used to illuminate the back of the foil, while the passage of light through possible holes was viewed from the front. Invariably, this test was sufficient.

4. Gas Handling and Manometer

The gas handling consists of a network of quarter-inch copper tubing linking one or two gas bottles with the chamber proper through quarter-inch Hoke needle valves. In addition, there is a compound gauge that monitors the pressure in the gas line.

The manometer is connected between the chamber proper and the high vacuum through 3/8" copper tubing. The fluid used is n-butyl sebacate (Russell et al. 1956), because of its low vapor pressure. Its specific gravity was measured to be 0.927 ± 0.003. The manometer, being in excess of one meter, was long enough for the pressures used. A cathetometer was used for accuracy in making the pressure readings. Although the cathetometer can be read to within 0.001 cm., the process used in setting it up reduced the accuracy to approximately $\pm$ 0.03 cm.

5. Charcoal Trap

In order to remove significant contaminants, e.g. oxygen and nitrogen, a 2" diameter charcoal trap is mounted in the bottom of the chamber. At liquid nitrogen temperatures, this trap sufficed to keep the total contaminant yield below 1% of the scattered or recoil-particle yield at all angles. Because the trap absorbs deuterium, it was not cooled when deuterium was in the chamber.

6. Detection of Scattered Particles

Two detectors were used: one was capable of motion for angular distributions and the second was stationary for monitoring the beam as

a check on the consistency of the current measurement. The moving detector was a 1 mm. thick lithium drifted solid state detector with a 5/8" diameter active area and overall diameter of 7/8". The lithium drifted detector had a resolution of 1.5% for 8.778 MeV Pb^{212} alpha particles, using the electronic setup described in "Experimental Procedure."

The lithium drifted detector is an extension of the p-n diffused junction (Pell 1960). The drawback with a normal p-n detector is the need for high reverse bias voltages in order to acquire a thick enough depletion depth for complete energy collection from fast particles. The lithium drifted detector, on the other hand, does not need a large reverse bias for a thick depletion depth, for the detector--by virtue of being a drifted p-i-n junction--is inherently deep and only needs bias for ion pair collection.

The fabrication* of the p-i-n junction is accomplished by first depositing lithium on a slab of low resistivity (100 Ω-cm.)p-type silicon. The lithium is then diffused and subsequently heated with reverse vias on the silicon. What happens at this point is believed to be a compensation for the p acceptor type silicon by a deposition of the lithium donor atoms interstitially. The result is an intrinsic region, the depth of which depends on the voltage, temperature and time elapsed in drifting.

---

* The detector was made by J. R. Yvon Cusson from a method developed by M. Emery Nordberg, Jr. and J. R. Yvon Cusson.

It is only possible to compensate the material, at most, and not possible to change the n-type region to p or the p-type region to n in that reverse fields would set up a reverse drift, if over-compensation were imminent. On completion of the drift process, the back of the detector is carefully etched and used as the exposed surface for particle entry, using a gold evaporation for electrical contact.

The monitor was an 8500 Ω-cm. surface barrier detector, fabricated by the author. Although the effective thickness was somewhat less (6-7 MeV protons) than that of the movable detector, the resolution was quite adequate for the purpose.

Both detectors were provided with collimators, consisting of rectangular openings milled in 1/16" steel. The shapes of the openings for the moving detector were chosen in such a way as to simplify the data reduction (Appendix A) and to minimize second order corrections. The dimensions, as determined finally by measurements on a comparator, were

Front slit: $0.08145'' \pm 0.4\%$ wide

Rear slit: $0.04088 \pm 0.5\%$ inch^2 area; $0.0825''$ wide

$h = 2.3325'' \pm 0.005\%$ (Figure 10)

$R_o = 4.79'' \pm 0.1\%$ (Figure 10)

The monitor detector, with its collimating assembly, was affixed to the chamber cover plate ((9) in Fig. 2), at an angle of about 30° to the incident beam. The movable detector was mounted on a carefully

machined hub ((18) in Fig. 2) which could be rotated from outside the chamber. A vernier protractor permitted angle settings accurate to 6' of arc. A sliding post in the center of the hub establishes the geometrical center of the rotating system.

B. Assembly and Testing

1. Alignment

The philosophy of the assembling of the chamber was to be as careful and precise as possible, then check by repeating some well-known gas scattering experiments. The first step in the assembly was to mount the moving detector and collimator on the adjustable platform in the proper orientation. This was accomplished by making the sub-assembly in a mill, using a dial indicator to ascertain that the slit was vertical. The counter mount was then assembled in the chamber, setting the distance from a vertical flat on the center post to the front slit to 2.46".

After assembly, the chamber was aligned with respect to the optical axis of the beam tube. This optical axis had been defined by the zero position of two pairs of orthogonal adjustable slits in the beam tube and a bench mark on the wall of the target room. A Brunson telescope was set on the upstream end of the beam tube collinear with the optical axis; then the chamber was positioned while viewing the defining apertures of the beam collimator to insure collinearity. The

moving counter collimator was then lined up with the detector removed by sighting the pattern made by the slits of the collimator, the point of the center post and the apertures of the beam collimator.

2. Experimental Checks on the Accuracy of the Chamber

In a first attempt at designing and constructing any apparatus with a measure of complexity, there are inevitably flaws in the resulting product. To enumerate the extent and degree of that imperfection in this tome would not only enlarge it significantly, but would be to a great extent embarrassing in the recounting. Suffice it to say, there were numerous preliminary runs on the chamber that pointed up numerous imperfections, which were corrected. The presentation here will discuss the chamber as a finished product and the final tests that exude an air of respectability in their relating.

a. Faraday Cup Voltages

The Faraday cup was run positively biased and the suppressor or guard ring was run negatively biased. Electrostatic suppression proved sufficient in the case of deuterons as incident particles, but it was necessary to introduce magnetic suppression in the case of alpha particles below 6 MeV (Section II-B-b). The necessary value for the voltage on the suppressor to stop electrons from the exit foil and the necessary value for the voltage on the cup to prevent electrons from leaving the cup were obtained by connecting the monitor to a scaler

and noting the variation in counts for a prescribed total charge. It can be seen from Figure 3 that the charge collection is independent of the voltage on the cup and becomes independent of that on the suppressor at about -80 volts. Typical running values were -300 volts on the suppressor and +67½ volts on the cup with the additional aid of the magnetic suppression.

b. Rutherford Scattering

The chamber was filled with tank argon of 99.5% purity, and the elastic scattering of 4.5-MeV alpha particles determined for $\theta_{c.m.} \approx 30\text{-}160°$. The first experiments, carried out with only electrostatic electron suppression in the beam collector, showed consistent deviations from Rutherford scattering of about 15%. After installation of a magnetic suppressor (Section II-A-2), data were taken at 30° and 60°. The ratio of the cross-section to Rutherford was 1.03 at 30° and 1.06 at 60°, in keeping with the accuracy of the experiment.

c. Multiple Scattering

The chamber was checked for multiple scattering at 12° laboratory angle for $He^4(\alpha,\alpha)He^4$ at 4 MeV and for $He^4(d,d)He^4$ at 3 MeV, by varying the pressure of the chamber from about 6 cm.-oil to about 25 cm.-oil. The results are shown in Figures 4 and 5, and indicate that multiple scattering corrections to our data would in all cases have been less than 1.0%.

d. Miscellaneous

In addition to the above tests, there were several others checking minor features of the chamber. These included verification of the assumption that the thermometer in the chamber measured the temperature in the scattering volume. If the temperature throughout the chamber is not uniform, one would expect to see variations in monitor counts when the beam current is changed. This test was run with alpha particle beams from 0.075 μa. to 0.025 μa. and the counts for a given integrated charge showed no systematic variation, validating our assumption.

It was also found necessary during our runs to eliminate background arising mainly from neutron reactions in the silicon detectors. These neutrons were caused primarily by the stripping of deuterons on the first slit and the entrance foil. In order to minimize the effect of these neutrons, a heavily shielded slit was placed before the foil to stop excess beam and the forward half of the scattering chamber was filled with steel, the most effective neutron shielding for a small volume.

III. EXPERIMENTAL PROCEDURE

A schematic drawing of the experimental setup is given in Figure 6. The beam of accelerated particles--in this instance deuterons, He^{4+} or He^{4++} with energies from 3-11.5 MeV--is provided by the tandem accelerator. After energy analysis in the 90° deflecting magnet, focusing and collimation, the beam passes through the entrance foil, the entrance collector, through the chamber and into the Faraday cup. Within the chamber, particles scattered in a volume of the gas defined by the cross-section of the beam and the geometry of the counter collimators are detected in the movable and fixed solid-state counters.

The signals from the counters are amplified by Tennelec model #100 fast ($\sim 0.1\ \mu s.$) charge-sensitive cascade preamplifier (Fig. 7) and Hamner model N328 non-overloading, double delay line, clipped linear amplifier and finally into a Radiation Instrument Development Laboratory 400 channel analyzer. Pulses from the fixed (monitor) counter are fed into an Eldorado model SC-700 decimal scaler.

The beam collected in the Faraday cup was integrated with an Eldorado model CI-110 current integrator, which is calibrated with a test current supplied by a standard cell that is measured with a galvanometer and a $0.9985 \pm 0.1\%$ M Ω resistor (see Fig. 8). The clock used for timing the total charge is accurate to within $\pm$ 0.1%.

Since the integrator was calibrated at the same current as that of the beam, the error due to leakage currents, internal to the integrator, was minimized.

The typical procedure in collecting experimental data is as follows. The chamber is opened to the roughing pump of the main pumping station, while the charcoal trap is heated. During this time, bias voltages are applied to the detectors and they are checked out on the oscilloscope to see whether they are excessively noisy. In addition, the current integrator is set, and the total charge determined by running a known current, calculated from a galvanomter reading and a resistor, against a prescribed time to accumulate the desired amount of charge.

After the charcoal trap has been heated sufficiently, the diffusion pump is connected to the system, which is pumped until a pressure of 10^{-6} mm. Hg. is reached. At this time, the center part of the chamber is closed off and filled with gas. The charcoal trap is then cooled to liquid nitrogen temperatures and kept cold throughout the experiment unless deuterium is the gas in the chamber, in which case the trap is left at room temperature. Both temperature and pressure are measured at frequent intervals during the run.

The chamber is now ready for beam. The beam alignment is accomplished by a trial and error procedure with the aid of electrostatic and magnetic steering throughout the tandem system, focusing with quadrupole magnets on a viewing quartz interposed just before the entrance

foil. The quartz is then removed and the beam maximized in the Faraday cup by again adjusting the steering and focusing of the beam.

The runs are now made, with a running check on the pressure, temperature, clock time and live time of the analyzer. Changes in counter angle are accomplished manually. Upon completion of the runs, the integrator is again checked and is found to remain stable to within the accuracy of the measurements.

The preponderance of data are those obtained from $He^4(d,d)He^4$, although for a few of the low energy runs, data from $H^2(\alpha,\alpha)H^2$ are used. A typical pulse-height spectrum obtained with deuteron bombardment is shown in Figure 11 (E_d = 5 MeV, θ_{lab} = 35°). In this spectrum may be seen the deuteron peak at channel number 61 and the alpha particle peak at channel number 41. Background counts are superimposed on these peaks, starting off with a relatively high value at low channel numbers and rapidly falling to zero at higher channel numbers. The contaminant spectrum is above channel 64, but does not appear in the figure, since there are only about 10 counts in the peak. At higher energies, the peaks both decrease in size with the number of counts in the deuteron peak falling below the number of counts in the alpha peak. At larger laboratory angles, the peaks appear at lower channel numbers and finally are absorbed in the background. The information from the alpha peak can no longer be resolved from the background at θ_{lab} = 45° and the deuterons can no longer be resolved from the background at 90°.

The spectra for the monitor counter are essentially the same as those of the moving counter with the exception that at 8-9 MeV the deuteron was energetic enough to penetrate the depletion region in the counter, resulting in pulses being dropped to lower channels, corresponding to the fraction of the total energy lost in the depletion region.

It was only at energies of $E_d < 4.5$ MeV that a few $H^2(\alpha,\alpha)H^2$ runs were made, because of the reduction in background when alpha particles are used in place of deuterons as the incident projectiles. The benefit from the reduction in background is outweighed, however, by the limitation in center of mass energy and angle (Figs. 9A and 9B) when using $H^2(\alpha,\alpha)H^2$. As a result, the angular distributions from this reaction were taken only at $E_\alpha/2 = 2.935$, 3.441, 3.946 and 4.450 MeV and angles from 50° to 130° at 10° intervals in the center of mass (Figs. 18 through 21).

IV. RESULTS

The main body of data comprises angular distributions at various bombarding energies, E_d from 3 to 11.5 MeV and excitation functions at 18, 55, 90, 130 and 156 degrees (Figs. 18-42). These data have compared with those of Galonsky et al. (1955) (Fig. 39) and Stewart et al. (1962) (Fig. 41). There is a tendency for both the previous works to be somewhat high with respect to the present study, but the agreement on the whole is fair. This work is in definite disagreement with Burge et al. (1952) (Fig. 29).

At this juncture, clarification of the data presentation is made. The points on the Figures 18 through 42 are experimental with relative error bars and the solid lines are the phase shifts analysis fit to the data. In those instances where an analysis was not made, dashed lines are drawn through the experimental points for clarity. It should be noted that Figures 39 and 40, which appear at first to be identical, are in fact different in emphasis. The data on Figure 39 was taken expressly for the excitation curve, whereas Figure 40 is an excitation curve compiled from angular distribution data. The data of Figure 40 extend up to 11.5 MeV and suggest a negative curvature in the vicinity of 9 MeV that is not readily apparent in that of Figure 39.

The levels of interest here are the T = 0 levels in Li^6, which are the only ones that can be reached with d-He^4 elastic scattering. These are in particular the E_x = 4.52, 5.5 and 7.4 MeV levels (Ajzenberg-Selove and Lauritsen 1959). It was found (Fig. 38) that 4.52 MeV is the only prominent level; the 5.5-MeV level manifests itself as a slight dip in the cross-section at 90° (Figs. 39 and 40) in keeping with its 1^+ assignment (Galonsky and McEllistrem 1955a); the 7.4-MeV level manifests itself both in the variation in the character of angular distributions from about 6.5 MeV (Figs. 23 through 36) and in a negative curvature in the 90° excitation curve (Fig. 40), suggesting (but not determining) the presence of a negative parity state (Galonsky and McEllistrem 1955a). This argument will be pursued further in the section "Analysis of Data."

V. REDUCTION OF EXPERIMENTAL DATA

A. Energy Loss in Foil and Gas

In order to determine the actual energy of the incident particle, it was necessary to make a correction for the energy loss in the entrance nickel foil and in the gas between the entrance foil and the scattering volume. This was done through the use of the stopping cross-section for protons, ϵ_p, plotted by Whaling (1958) for H^2, Ni and He^4 as the target materials. The values of the stopping cross-sections for alpha particles and deuterons were computed with $\epsilon_\alpha (E_\alpha) = 4\epsilon_p (E_\alpha/3.97)$ and $\epsilon_d (E_d) = \epsilon_p (E_d/2)$, where E_α and E_d are the respective energies of alpha particles and deuteron particles. The densities used for nickel, helium and deuterium were 8.75 gms./cc., 0.17847 gms./liter and 0.17976 gms./liter respectively at standard temperature and pressure conditions. The thickness of foils stated by the supplier was assumed correct. The distance from the entrance foil to the center of the chamber is 8.719". The results are tabulated in Tables I through III.

B. Energy of Observed Particles

In order to differentiate the alpha particle from the deuterium particle in the spectrum of the angular distribution, it is necessary to know something about the kinematics of the reaction. This is easily

obtained by using Equations 2.3 through 2.7 on pages 412ff. of Evans (1955), which gives

$$E_r/E_o = 4M_1M_2\cos^2(\theta_r)_{lab}/(M_1 + M_2)^2 \qquad (1)$$

and

$$E_s/E_o = \left\{M_1^2/(M_1+M_2)^2\right\}\left\{\cos(\theta_s)_{lab} \pm \left[(M_2/M_1)^2 - \sin^2(\theta_s)_{lab}\right]^{\frac{1}{2}}\right\} \qquad (2)$$

where the "nuclear disintegration energy" is equal to zero for elastic scattering and minor changes in notation are made giving the following:

E_r is the energy of the recoil particle

E_s is the energy of the scattered particle

E_o is the energy of the incident particle

M_1 is the mass of the incident particle

M_2 is the mass of the target particle

$(\theta_s)_{lab}$ is the angle of scattering for the scattered particle in the laboratory

$(\theta_r)_{lab}$ is the angle of recoil for the struck particle in the laboratory

It is seen that Equation 1 is always single-valued, but Equation 2 is single-valued when $M_2 > M_1$ and double-valued when $M_2 < M_1$ in keeping with the argument on page 412 of Evans (1955), that the square root of the ratio of the energies is real and positive. The graphs for d on He^4 and He^4 on d are Figures 9A and 9B respectively.

C. Formulas for Data Reduction

The formulas, together with their approximations for the differential cross-section as a function of yield and experimental parameters, are derived in Appendix A. The errors due to the approximations, statistics and the inaccurate knowledge of the experimental parameters are discussed in the following section. Here we present merely the formulas for the differential cross-section in the center of mass due to the yield of the incident particle

$$(d\sigma/d\Omega)_{cm} = (Y_s/NnG)\ \sin(\theta_s)_{lab}\ (d\Omega_{lab}/d\Omega_{cm}) \tag{3}$$

and that due to the yield of the recoil particle

$$(d\sigma/d\Omega)_{cm} = (Y_r/4NnG)\ \tan(\theta_r)_{lab} \tag{4}$$

where

$$G = 2bA/R_o h$$

and

Y_s is the yield of scattered particles

Y_r is the yield of recoil particles

N is the number of beam particles during the counting period

n is the number of target particles per cubic centimeter

A is the area of the second collimator defining slit (Fig. 2)

$2b$ is the width of the first collimator defining slit (Fig. 10)

R_o is the distance from the center of the chamber to the back of the second defining slit (Fig. 10)

h is the distance from the front of the first to the back of the second defining slit (Fig. 10)

The kinematics for the incident particle in a two-body reaction is discussed in Marion and Ginzbarg (1949), and the conversion from lab angle to c.m. angle and the solid angle ratio, $d\Omega_{lab}/d\Omega_{cm}$, were obtained from their tables for the scattered particle, using $x = M_1/M_2$, where M_1 is the mass of the incident particle and M_2 is the mass of the struck particle. These tables were calculated from

$$d\Omega_{lab}/d\Omega_{cm} = \cos(\theta_{cm} - \theta_{lab})\sin^2\theta_{lab}/\sin^2\theta_{cm} \qquad (5)$$

A discussion of these kinematics can also be obtained in Evans (1955), where the following formulas* are derived for lab angle to c.m. angle conversion,

$$\cot(\theta_s)_{lab} = (M_1/M_2)\csc(\theta_s)_{c.m.} + \cot(\theta_s)_{c.m.} \qquad (6)$$

for the scattered particle from which Equation 5 is obtained, and

$$(\theta_r)_{lab} = (\pi - (\theta_r)_{c.m.})/2 \qquad (7)$$

for the recoil particle, which gives together with

$$d\Omega_{cm}/d\Omega_{lab} = \sin\theta_{cm}\, d\theta_{cm}/\sin\theta_{lab}\, d\theta_{lab} \qquad (8)$$

the obvious result

$$d\Omega_{lab}/d\Omega_{cm} = \tan\theta_{lab}/4\sin\theta_{lab} \qquad (9)$$

---

* Equations 6 and 7 are the same as Equations 23 and 22 on p. 834 of the cited text with changes in notation.

where

$(\theta_s)_{cm}$ is the angle of scattering in the center of mass

$(\theta_r)_{cm}$ is the angle of scattering in the center of mass determined from the recoil particle in the laboratory system

D. Error Analysis

The analysis of the probable error in this experiment was divided into two parts. One, which is angle-independent and which we choose to call the systematic error, is motivated by Equations 3 and 4 and is tabulated in Table IV. The important factors are the accuracy of the geometric factor, G, the accuracy of charge collection manifested in the beam rate, N, the error in the pressure and temperature manifested in the particle density, n. In addition, the error due to the approximation in the differential cross-section reduction formulas is calculated. The total systematic error due to these factors combines to give an rms value for the probable systematic error of 1%.

The relative error arises from several sources. The error in estimating the background (taken to be 1/4 of the background, N/4 (Fig. 11)) contributes. Also, the statistics of the total number of counts in the peak, including the background, M + N, and separately the statistics of the background, N, contribute. These contributions give a relative error of $(M + 2N + N^2/16)^{\frac{1}{2}}$. In addition, there are other factors contributing to the relative error; among these are the errors

arising from the uncertainty in the alignment of the chamber ($\pm$ 6') and the inaccuracy in setting a given protractor angle (also $\pm$ 6'). These inaccuracies are reflected in the $\sin(\theta_s)_{lab}$ $(d\Omega_{lab}/d\Omega_{cm})$ and $\tan(\theta_r)_{lab}$ terms of Equations 3 and 4. Tabulations of this effect are in Tables V and VI. A further effect of the two sources of the $\pm$ 6' uncertainty is an uncertainty as to the true value of the measured yield. This effect of approximately 1.5% predominates at 17.97° and 156° in the center of mass, at which angles this effect is included. At the same angles (17.97° and 156°), an additional effect is of significance, that of the error resulting from a high dead-time correction. This error was found to be on the order of 2% for the large dead-time correction of 30%. The procedure used for determining the dead-time correction was that of comparing the live-time meter of the 400 channel analyzer with a pulser connected to the analyzer and a scaler.

There are sources of error that were estimated to be negligible. The check on the dead-time correction shows that it is in error by less than 1% at angles other than 17.97° and 156°. Furthermore, the error in yield due to uncertainty in angle is also less than 1% at angles other than 17.97° and 156°. Also, extrapolation of the contaminant yield to forward angles, where it could not be resolved from the desired particle yield, indicates errors of less than 1% and might be considered to be accounted for in the background subtraction. Finally, the mean charge of 2 used for $H^2(\alpha,\alpha)H^2$ is not in error by more than 0.6%.

VI. ANALYSIS OF DATA

A. Introduction

1. Outline of the Analysis

Here the choice of approach in analyzing the elastic scattering data will be recapitulated. With the rather sparse evidence for any level other than the 2^+ (Section IV), it was decided not to use a single level approximation to begin with, but to use a parametrization in terms of phase shifts with real and imaginary parts and tensor coupling parameters. The derivation of the scattering cross-section formula

$$3k^2 \frac{d\sigma}{d\Omega} = 2|A|^2 + |B|^2 + \sin^2\theta\left\{|C|^2 + |D|^2\right\} + \sin^4\theta\left\{|E|^2\right\}$$

is outlined in Appendix C and is equation C.10, where

$\frac{d\sigma}{d\Omega}$ is the differential scattering cross-section in the center of mass system

k is the wave number for the reduced mass

A through E are the transition amplitudes from channel spin state m_s to channel spin state $m_{s'}$, where

$$k^2\left(\frac{d\sigma}{d\Omega}\right)_{+1,+1} = k^2\left(\frac{d\sigma}{d\Omega}\right)_{-1,-1} = |A|^2$$

$$k^2\left(\frac{d\sigma}{d\Omega}\right)_{0,0} = |B|^2$$

$$\frac{k^2}{\sin^2\theta}\left(d\sigma/d\Omega\right)_{0,+1} = \left(k^2/\sin^2\theta\right)\left(d\sigma/d\Omega\right)_{-1,0} = |C|^2/2$$

$$(k^2/\sin^2\theta)(d\sigma/d\Omega)_{0,+1} = (k^2/\sin^2\theta)(d\sigma/d\Omega)_{0,-1} = |D|^2/2$$

$$(k^2/\sin^4\theta)(d\sigma/d\Omega)_{+1,-1} = (k^2/\sin^4\theta)(d\sigma/d\Omega)_{-1,+1} = |E|^2/2$$

These parameters are given in terms of the scattering matrix U, in equations C.11 through C.15. Each of the above amplitudes conserves $J\pi$, and consists of a part that conserves ℓ and a part that allows ℓ to change by ± 2. In addition, amplitudes A and B have a Rutherford scattering term because m_s is conserved for these elements.

Even though one does not obtain the quantitative values for the widths or excitation energies of the levels in using a phase shift analysis, one does get an indication of the resonating terms, in that they tend to go positive instead of continuing the negative trend due to potential or hard sphere scattering. Furthermore, once the phase shift parameters are obtained, single level parameters can be calculated on the assumption of an interaction distance. This procedure is outlined in Appendix D and the level parameters tabulated in Tables VII through IX.

Once the phase shift analysis was decided upon, it was necessary to determine the parameters to use. Galonsky and McEllistrem (1955a) used s-wave and d-wave in their single-level analysis of the data up to $E_d = 4.62$ MeV. It is therefore obvious that s through d waves should be included in the analysis. This resulted in three parameters for the d-wave (δ_2^3, δ_2^2, δ_2^1) and one parameter for the s-wave (δ_0^1). In

view of the departure of p-wave from the hard sphere values in the analysis of Galonsky and McEllistrem, it was decided to use three parameters for the p-wave (δ_1^2, δ_1^1, δ_1^0). In addition, there is a possibility of coupling between levels of the same $J\pi$, so a coupling constant ϵ was introduced for coupling between δ_0^1 and δ_2^1 (Gammel et al., 1960). The above real parameters do not allow for the three particle reaction (see Introduction). In order to allow for the three particle reaction, it was decided to make all the aforementioned parameters complex.

At this juncture, one might consider the possible configurations for the E_x = 7.4 MeV level, which appears to have a negative parity (p. 22) and must be T = 0 if it is to be observed in the $He^4(d,d)He^4$ reaction. The possibility of additional p^2 states was discounted at this energy, in that Inglis (1952, 1953) predicted, through the use of intermediate coupling, that the next p^2 level was at E_x = 14.0 MeV. Also, p^2 configurations result in positive parity states.

From the former configuration, there are two possible T = 0 states: one, the space anti-symmetric singlet state that can be made with δ_1^1; two, the space symmetric triplet state that can be made with δ_1^2, δ_1^1 and δ_1^0. The lpld configuration allows several additional possibilities. Among the space anti-symmetric states, there are those formed by δ_2^2 and δ_3^3, in addition to the one formed by δ_1^1. And

among the space symmetric states, there are the ones formed by δ_3^4, δ_3^3, δ_3^2, δ_2^3, δ_2^2 and δ_2^1, in addition to the one formed by δ_1^2, δ_1^1, and δ_1^0.

Due to an error on the part of the author in determining the space symmetries, the greater fraction of these possibilities was not considered. And what is even more unfortunate, the more likely possibility ($^3P_{210}$) received only a cursory examination. All of the phase shifts, however, are included in the program with the exception of δ_3^4. In addition, a coupling parameter between δ_0^1 and δ_2^1 and a coupling parameter between δ_1^2 and δ_3^2 were included. The possibilities of varying the real and/or imaginary parts of the parameters were included, which resulted in a total of nine cases, and are self-explanatory in the copy of the program (Appendix G).

Before continuing, it would be advisable to look at the form of the scattering matrix. Lane and Thomas (1958) show that when the scattering matrix represents the totality of events in the universe, it must be unitary and symmetric. The unitarity insures conservation of particles with a total probability of one, and the symmetry insures the time reversibility of Schrödinger's equation. In the case of d-He^4 elastic scattering, where the reaction channels are not treated explicity in our formulation, it is necessary to account for a loss in particles by making the phase shifts imaginary.

In the case where there is not a coupling between channels of different ℓ values, the scattering is diagonal in the phase shift, δ_ℓ, but when there is a coupling between two ℓ values, the diagonal matrix must be rotated by a 2 x 2 unitary matrix (Blatt and Biedenharn 1952). This results in a coupling parameter or rotation angle, ε, in two space. A 2 x 2 scattering matrix without a loss of particles and without tensor coupling can be expressed by

$$U = \begin{pmatrix} e^{2i\delta_1} & , & 0 \\ 0 & , & e^{2i\delta_2} \end{pmatrix} \tag{10}$$

where δ_1 and δ_2 are real. When coupling between channels 1 and 2 is considered, U must then be operated on with the rotation matrix

$$T = \begin{pmatrix} \cos\varepsilon & , & \sin\varepsilon \\ -\sin\varepsilon & , & \cos\varepsilon \end{pmatrix} \tag{11}$$

where ε is real. Then,

$$U' = T^{-1}UT = \begin{pmatrix} \cos^2\varepsilon\, e^{2i\delta_1} + \sin^2\varepsilon\, e^{2i\delta_2} & , & \tfrac{1}{2}\sin(2\varepsilon)(e^{2i\delta_1} - e^{2i\delta_2}) \\ \tfrac{1}{2}\sin(2\varepsilon)(e^{2i\delta_1} - e^{2i\delta_2}) & , & \sin^2\varepsilon\, e^{2i\delta_1} + \cos^2\varepsilon\, e^{2i\delta_2} \end{pmatrix} \tag{12}$$

It is readily seen that within the constraints on the scattering matrix, three additional parameters can be used by considering those

already used as being complex instead of real. Furthermore, if there were no coupling, it is obvious that complex phase shifts give an amplitude reduction or a loss in particles.

The object of the program (Figure 12) is to calculate, using a starting set of phase shifts and coupling parameters, a scattering cross-section for each angle and comparing it with the experimental cross-section. On this comparison, a necessary change in the initial parameters is derived, and if this change is significant, the initial parameters are changed, and a new set of cross-sections is calculated. This continues, until the changes become insignificant.

Our motivation in calculating the change in the starting parameters is a modification of Newton's method:

$$(\sigma_{ex})_n = (\sigma_{calc})_n + \sum_{i=1}^{I} (\partial\sigma_{calc}/\partial\delta_i)_n \Delta\delta_i + \cdots \qquad (13)$$

where

I is the number of parameters

N is the number of angles in an angular distribution

$(\sigma_{ex})_n$ is the n^{th} experimental differential cross-section

$(\sigma_{calc})_n$ is the n^{th} calculated differential cross-section

δ_i is the i^{th} parameter

$\Delta\delta_i$ is the change in the i^{th} parameter

One has, in general, N pieces of data for N angles at a given energy, and therefore can form matrices with N rows. Letting $z_n = (\sigma_{ex})_n - (\sigma_{calc})_n$, one obtains column matrices with N rows for z and I rows for $\Delta\delta_i$. The matrix A for $(\partial\sigma_{calc}/\partial\delta_i)$ has I columns and N rows. In order to calculate $\Delta\delta_i$, one would normally proceed by multiplying A and z by the transpose of A, then multiplying both sides by the inverse of A^TA. This results in

$$\Delta\delta = (A^TA)^{-1}(A^Tz) \tag{14}$$

This was tried, but did not converge. The argument is that necessary precision is lost on taking the inverse, even though a double precision matrix inversion routine was used. It was decided that the mathematical grounds for the method used to obtain convergence were incidental, provided a method of convergence could be found. In this spirit, a gross simplification was made by considering all of z_n to be due to the δ_i under consideration, which resulted in

$$\Delta\delta_i = N^{-1}\sum_{n=1}^{N} z_n/A_{ni} \tag{15}$$

after averaging the $\Delta\delta i$ due to each n over the number of pieces of data, N. The procedure resulting from equation 15 did not work any better than that of equation 14. It was decided that the problem might have been over-simplified. In order to better approximate the method of equation 14 and yet avoid a matrix inversion, it was decided to

ignore the off-diagonal elements of $A^T A$ and use the equation

$$\Delta \delta_i = \sum_{n=1}^{N} z_n A_{ni} \Big/ \sum_{n=1}^{N} A_{ni} \qquad (16)$$

which proved successful.

In the program, once a satisfactory set of values is obtained for the parameters, the iteration stops and the tensor polarization parameters, which are the invariant parameters of double scattering (Appendix E), and the total reaction cross-section are calculated. The formula used for the total reaction cross-section was

$$\sigma_r = (\pi/k^2) \sum_{\ell} \Big\{ (2\ell+1) - [(2\ell+3)/3] \left| U^{\ell+1}_{\ell,\ell} \right|^2 - [(2\ell+1)/3] \left| U^{\ell}_{\ell,\ell} \right|^2 - [(2\ell-1)/3] \left| U^{\ell-1}_{\ell\,\ell} \right|^2 - [(2\ell+3)/3] \left| U^{\ell+1}_{\ell,\ell+2} \right|^2 - [(2\ell-1)/3] \left| U^{\ell-1}_{\ell,\ell-2} \right|^2 \Big\} \qquad (17)$$

in keeping with Blatt and Weisskopf (1952a), p. 431.

2. Procedure in the Analysis

The phase shift analysis, in its original form, was coded for the Burroughs 220 in machine language. The differences between the 220 program and that finally coded in Fortran for the IBM 7090 (Appendix G) was that the former did not include tensor coupling and imaginary phase shifts for particle loss in the reaction channels. In addition, the

decision-making logic used for the 220 program was much simpler in that the author was present to make logical decisions throughout the iterative procedure.

The Burroughs 220 program was initially checked by using the phase shifts Galonsky and McEllistrem (1955a) report at the 1.07 MeV level in the program and confirming the cross-sections they report. Unfortunately, these data were all at back-scattering angles and did not point up a program error in the Rutherford part of the scattering cross-section. This error was revealed on comparing the 220 program with the 7090 program, using the same input data. In addition, the accuracy of the corrected 220 program was checked by hand calculations for simple input data and further compared with the 7090 program. This did not give a check on ε or on the imaginary parts of the phase shifts. However, all errors that would show up in internal inconsistencies (e.g., the existence of a total reaction cross-section with all real variable parameters) were found. Also, visual checking and rechecking of the program was done.

In the region from 3 to 4.5 MeV, the object of the program was to verify the results of Galonsky and McEllistrem (1955a). This was done, mainly, by trying to eliminate the need for the 1^+ resonance, in that it was not salient in the $He^4(d,d)He^4$ excitation curves. This procedure did not work. As a result of the phase shift analysis in the 3 to 5 MeV region, anomalous behavior of δ_2^2 and δ_2^1 was necessary.

As further corroboration of the work of Galonsky and McEllistrem (1955a), it was not possible to continue the p-wave according to hard sphere scattering, but instead there was a trend for all the p-waves to stay above -20° (Figure 15). The real part of ε was included in the analysis and the value for it ranged from 14° at 2.935 MeV to 0.8° at 4.955 MeV (Figure 13) for the best fits. This behavior seems unrealistic, especially in view of the prediction that ε is insignificant in this energy region (Gammel et al. 1960). An explanation of this behavior might be obtained from considering the small number of data points used in this region with somewhat large error bars.

The analysis from 5 to 7 MeV proved to be particularly challenging. The reasons for this are many. First, there is a three particle reaction that manifests itself through one or more of eight possible channels, if we limit ourselves to $\ell = 2$ waves as a maximum. Furthermore, the real part of ε was predicted to be of significance in this energy range (Gammel et al. 1960). Moreover, there is the change of characteristic in the angular distributions that suggests a resonance, which can come about through one or more of seven possibilities, if the arbitrary restriction $\ell = 2$ maximum is imposed. If f-waves are also considered, six additional parameters occur. In view of the large number of possibilities, it was necessary to exercise judgment and concentrate on the possibilities that were more likely.

In spite of the complications in this energy region, it was possible to continue the real parts of the s-wave and the d-waves with reasonable confidence (Figures 13 and 14). The δ_0^1 parameter is in good agreement with that predicted by Gammel et al. (1960) and the δ_2^3 parameter is not unreasonable. The resonating behavior of δ_2^2 and δ_2^1 will be discussed further below.

An attempt was made in this energy region to eliminate the 7.4 MeV level with no real success. Consequently, a decision had to be made about the p-waves. The departure from hard sphere behavior continued in this region with δ_1^0 and δ_1^1 being especially conspicuous. There is reason (see "Outline of the Analysis") to expect a resonance through δ_1^0, but the attempt was made to give δ_1^1 resonant behavior. This will be discussed further below.

On investigating the consequences of an imaginary part for ε, it was shown that this should be small or zero, depending on the imaginary parts of δ_0^1 and δ_2^1, in order to prevent a creation of particles (Tombrello 1963). The real parts of ε proved to be slightly negative (-2°) after averaging over the best fits in this energy region. In view of the fact that the scatter about the average was in excess of 2°, it would not be unreasonable to use zero as the value of ε in this energy region.

The three particle reaction tended to perturb the imaginary parts of δ_2^3 and δ_2^2, and upon calculating the excitation curve for

the total reaction cross-section, using the average values of the parameters obtained in the phase shift analysis, a rather convincing curve resulted (Figure 17). This curve, on extrapolation of the lower end, is in rather good agreement with the threshold of the reaction (Henkel et al. 1955), and on extrapolation at the high-energy end, is in good agreement with the reported total cross-section of 0.3 ± 0.1 barn (Allred et al. 1951). In that the total reaction cross-section was not used as a constraint in the analysis, this convincing result would indicate that the reaction cross-section is fairly well determined by the scattering data.

The tensor polarization parameters resulting from the analysis are in reasonable agreement with those of Haeberli (1963) and Seiler et al. (1962) and are tabulated in Tables X through XXIII.

a. The 2^+ Level

The values for δ_2^2 are in good agreement with those of Galonsky and McEllistrem (1955a) up to 4.5 MeV (Figure 14). The continuation of this parameter through the transition region (5 to 7 MeV) presented some difficulty, in that there was a tendency for it to level off at any one of several values starting at 120°. The continuation chosen was the one consistent with a small value of ϵ in both the real and imaginary parts. Once the values of the δ_2^2 phase shift were obtained, a reliability check was made on them by introducing reasonable variations

in the p-waves. The values for δ_2^2 remained fairly insensitive.

From the values of δ_2^2, a single level approximation was made, using a value of 4.8 fermis for the interaction radius, which gave the best agreement in the resonant region ($\beta \approx 90°$) of several radii tried, including that of 3.5 fermis used by Galonsky and McEllistrem (1955a).

The reason the interaction radius of 3.5 fermis is acceptable for Galonsky and McEllistrem's (1955a) analysis,but unacceptable for the analysis of the present experiment, stems from the variation between the δ_2^2 of the former experiment and that of the latter (Figure 14) in the region of resonance. Once the resonant phase shifts, θ, are calculated from the level assignments of each of the aforementioned experiments, the resonant phase shifts of both of the experiments are exceptionally compatible. On the other hand, the values for the resonant phase shifts of the present experiment , obtained from the single level approximation, differ quite markedly (15°-20°) from the values obtained from the phase shift analysis in the neighborhood of $E_d = 9$ MeV. This deviation would imply that it is impossible to make a single level approximation to the scattering data throughout the resonating region, holding the interaction radius constant. The assignments resulting from the single approximation are tabulated in Table VII.

b. The 1^+ Level

The continuation of the δ_2^1 phase shift through the transition region was easier and the values for this parameter less sensitive than those of the remaining parameters. A single level parameterization of this level was also made with an interaction radius of 4.8 fermis, the results of which are tabulated in Table VIII.

c. The 7.4 MeV Level

The behavior of δ_1^1 chosen as the parameter of the resonance is extremely poor. The "mean" curve was drawn through points with a great deal of scatter (Figure 15). The fit of the angular distributions calculated from these "mean" values for the parameters to the experimental points leaves something to be desired at all energies, with the possible exception of 7.968 MeV. These deviations from good fits might be attributed to the p-wave inconsistencies. In spite of the lack of confidence in the 1^- assignment for the 7.4 MeV level, a single level parameterization was made, using an interaction radius of 3.5 fermis, which gives the correct excitation energy. The results of the parameterization are tabulated in Table IX.

B. Discussion

The phase shift analysis corroborated Galonsky and McEllistrem (1955a) in the 3 to 4.5 MeV range. Furthermore, there was a measure

of success in the fitting through the transition region (5 to 7 MeV). The successful aspects were the determining of assignments for the 2^+ and 1^+ levels, a convincing prediction for the shape of the total cross-section for the three particle reaction and reasonable values for tensor polarization parameters. The one great disappointment is the uncertainty of the level assignments for the 7.4 MeV level evidence in the erratic behavior of the p-waves. Suggestions will be made for further study in this area after dispensing with the question of uniqueness of the phase shift analysis obtained from an elastic scattering experiment.

The problem of the uniqueness of a phase shift analysis fit is embodied in the number of parameters needed to describe the elastic scattering process of spin 1 particles on spin zero particles (Phillips 1960; Puzikov 1957). Equation C.10, although written with five parameters, each of which depends on all ℓ values, can be reduced to four (Gammel et al. 1960). These four parameters, in contrast to the case of one parameter for spin zero on spin zero particles, cannot be uniquely determined from angular distributions. The results of angular distributions present one constraint. In order to provide for the three additional constraints, it is necessary to perform double scattering experiments. The equation of import is (Stapp 1957)

$$I'(\theta',\varphi') = I_o(\theta')\,[1 + A(\theta',\varphi') + B(\theta',\varphi')\cos\varphi' + C(\theta',\varphi')\cos 2\varphi'] \qquad (18)$$

where

$I'(\theta'\varphi)$ is the differential cross-section after the second scattering

$I_o'(\theta')$ is the differential cross-section for an unpolarized beam and is measured in the elastic scattering experiment

A, B and C are parameters depending on the center of mass energy and the scattering angles

θ' and φ' are the angles of the second scattering using the plane formed by the first scattering as the $x'z'$ plane and the direction of the beam after the scattering as the z' axis

On examining equation 18, it is seen that by judicious choices in a double scattering experiment of the angles φ' for a given angle θ', the values for A, B and C can be determined.

The non-uniqueness of the phase shift analysis is probably not as bleak as it appears to be at first sight, in that there is a great deal of physical intuition in picking a starting set of values and insuring the continuity of the fit throughout the energy range considered. The problem arises if there are two solutions existing in the same area.

This was not investigated at length, but would seem improbable for those parameters that were insensitive and quite possible for those that were not.

In view of the large number of possible parameters in the fitting of the data and the lack of uniqueness in any given fit, it would seem advisable at this point to press for further theoretical study in order to determine more probable choices from the overwhelming possibilities. This study could center about the likelihood of low-lying odd parity states and their expected space symmetries and J values. In the case of triplet states, it would be informative to have a treatment of the splitting and whether the split has $L + S$ or $|L - S|$ as the lowest energy state. In the realm of a theoretical treatment, one might transcend the immediate problem and investigate the possible breakdown at high energies of the phase shift analysis and/or the single level approximation.

In addition to the above, and in keeping with the non-uniqueness of the elastic scattering fit, it would be advisable to incorporate the data of a double scattering experiment into the constraints on a phase shift analysis.

In lieu of striking out for new horizons, the more pedestrian approach may be taken in a concerted effort to understand the p-wave behavior in the elastic scattering. The ^3P state (see "Outline of the Analysis") is most probable, and an attempt should be made to force a δ_1^0 resonance in conjunction with δ_1^1 and δ_2^1. The δ_1^2 phase

shift,in conjunction with the δ_1^1 phase shift, is also suggested in the space symmetric triplet resulting from a 1pld configuration, and it might prove fruitful to force a resonance using both these phase shifts at the same time.

The possibility remains, in spite of the convincing evidence to the contrary, that the three particle reaction is not going through the correct channels as yet. It might be expected, in that the 2^+ and the 1^+ levels are resonating in the transition region, that the particle loss should go through the imaginary parts of δ_2^2 and δ_2^1 instead of δ_2^3 and δ_2^2.

As a final alternative, f-waves under more intensive study might present the solutions for dilemmas that still remain.

C. Summary

In summation, the phase shifts obtained are presented in Figures 13 through 16 after having drawn a "mean" curve through the calculated points. The fits to the angular distributions are presented in Figures 18 through 31 for the "mean" data. In addition, the assignments for the three levels investigated are tabulated in Tables VII through IX. The tensor polarization parameters are tabulated in Tables X through XXIII, and the total reaction cross-section is plotted in Figure 17.

APPENDIX A

Calculation of Reduction Formulas

In Figure 10, the origin of coordinates is located at the center of the rear aperture of the collimator. The z-axis is the centerline of the collimating slits, intersecting the beam line at $z = R_o$. The beam lies in the xz-plane, making an angle θ_o with the z-axis. The edge of the front slit is the line $x = b$, $z = h$.

We direct our attention to a bundle of particles leaving an element of the beam line dB, at distance B along the beam line from its intersection with the z-axis. The number of particles arriving at an area element dS in the xy-plane is

$$dY = Nn\, dB\, \sigma(\theta)\, dS \cos\chi\, R^{-2} \qquad (A.1a)$$

where χ is the angle between the normal to dS and the ray to dB. In terms of the angle θ between the beam line B and the ray between dB and dS,

$$dB = R\, d\theta / \sin\theta \qquad (A.1b)$$

and $$dY = Nn\, \sigma(\theta) \cos\chi\, dS\, d\theta / R \sin\theta \qquad (A.1c)$$

where $$\sigma(\theta) = (d\sigma/d\Omega)_{lab} \qquad (A.2)$$

Furthermore,

$$\cos\chi = (R_o - B\cos\theta_o)/R \qquad (A.3)$$

$$R^2 = (R_o - B\cos\theta_o)^2 + y^2 + (x - B\sin\theta_o)^2 \qquad (A.4)$$

$$R^2 \sin^2\theta = (R_o \sin\theta_o - x\cos\theta_o)^2 + y^2 \qquad (A.5)$$

On squaring the terms in (A.4) and solving for B, one obtains

$$B = (R_o \cos\theta_o + x \sin\theta_o) \pm \{ (R_o \cos\theta_o + x \sin\theta_o)^2 - (R_o^2 + y^2 + x^2 - R^2) \}^{\frac{1}{2}} \qquad (A.6)$$

Collecting terms

$$B = R_o \cos\theta_o + x \sin\theta_o \pm R\cos\theta \qquad (A.7)$$

evolves, which gives on making the appropriate substitution of Equation A.5

$$B = R_o \cos\theta_o + x\sin\theta_o \pm (\cos\theta/\sin\theta)\left\{(R_o\sin\theta_o - x\cos\theta_o)^2 + y^2\right\}^{\frac{1}{2}} \qquad (A.8)$$

It is obvious from Figure 11 that $B < R_o \cos\theta + x \sin\theta_o$, so the minus sign in Equation A.8 is retained. It can also be seen from Figure 10 that the limits on B are given by

$$(x - B \sin\theta_o)/(R_o - B\cos\theta_o) = (x \mp b)/h \qquad (A.9)$$

Now, let $\xi = \theta - \theta_o$, $c_o = \cos\theta_o$, $S_o = \sin\theta_o$. Then by a Taylor series expansion, one obtains

$$\cot\theta = c_o/S_o - \xi/S_o^2 - c_o\xi^2/S_o^3 \qquad (A.10)$$

On making this substitution into (A.8) and expanding

$$\left\{ (R_o S_o - x c_o)^2 + y^2 \right\}^{\frac{1}{2}} \approx R_o S_o \left\{ 1 - x c_o / R_o S_o + \tfrac{1}{2} (x c_o / R_o S_o)^2 \right.$$

$$\left. + \tfrac{1}{2}(y/R_o S_o)^2 - \tfrac{1}{2}(x c_o / R_o S_o)^2 \right\}$$

$$\approx R_o S_o - x c_o + \tfrac{1}{2} y^2 / R_o S_o \qquad \text{(A.11)}$$

one obtains upon neglecting x^3 and y^3 terms

$$B \approx x/S_o - y^2 c_o / 2R_o S_o^2 + \xi(R_o/S_o - x c_o/S_o^2) - \xi^2 R_o c_o / S_o^2 \qquad \text{(A.12)}$$

up to second order in ξ. Using

$$(R^2 \sin\theta)^{-1} = \sin\theta \left[R_o S_o - x c_o)^2 + y^2 \right]^{-1} = (S_o + \xi c_o - \xi^2/2S_o) /$$

$$\left[R_o S_o - x c_o)^2 + y^2 \right] \qquad \text{(A.13)}$$

$$\left[(R_o S_o - x c_o)^2 + y^2 \right]^{-1} = (R_o S_o)^{-2} \left[1 + 2x c_o / R_o S_o \right.$$

$$\left. + 3(x c_o / R_o S_o)^2 - (y/R_o S_o)^2 \right] \qquad \text{(A.14)}$$

and (A.12), one obtains, continuing the approximation

$$(R_o - B \cos\theta_o)/R^2 \sin\theta = (R_o S_o)^{-1} \left(1 + x c_o / R_o S_o \right.$$

$$\left. + (x c_o / R_o S_o)^2 + \tfrac{1}{2}(c_o^2 - 2)(R_o S_o)^{-2} y^2 - \xi^2/2 \right) \qquad \text{(A.15)}$$

Given (A.9), one has the limits on B and can determine the limits on ξ. This is accomplished by using (A.12) and temporarily neglecting ξ^2 terms and solving for ξ with the appropriate limits on B. One obtains

$$\xi \approx - (x \mp b)/h + y^2 c_o / 2R_o^2 S_o + (x \mp b)^2 h^{-2} c_o / S_o \qquad \text{(A.16)}$$

However, it can be seen from (A.12) that if

$$\xi = -(x \mp b)/h + y^2 c_o/2R_o^2 S_o \qquad (A.17)$$

then the extra term in (A.16) is of the order ξ^2.

Expanding

$$\sigma(\theta) = \sigma(\theta_o) + \xi\sigma'(\theta_o) + \tfrac{1}{2}\xi^2 \sigma''(\theta_o) \qquad (A.18)$$

and substituting (A.3), (A.4), and (A.5) into (A.1), one gets

$$NndS \int \sigma(\theta) \cos \chi (R \sin \theta)^{-1} d_\theta =$$

$$NndS(R_o S_o)^{-1} \int \left\{ \sigma(\theta_o) + \xi\sigma'(\theta_o) + \tfrac{1}{2}\xi^2\sigma''(\theta_o)\right\} \qquad (A.19)$$

$$x \left\{1 + x c_o/R_o S_o + (x c_o/R_o S_o)^2 + \tfrac{1}{2}(c_o^2 - 2)(R_o S_o)^{-2} y^2 - \xi^2/2\right\} d\xi$$

Using (A.17) for the limits on ξ, integrating over area A and continuing the approximation, one obtains

$$Nn(R_o S_o)^{-1} A\sigma(\theta_o)^2 bh^{-1}\Big\{ 1 + c_o x_{av}/S_o R_o + c_o^2 (x^2)_{av}/S_o^2 R_o^2 + \tfrac{1}{2}(c_o^2 - 2)$$

$$x (R_o S_o)^{-2} (y^2)_{av}$$

$$-b^2/6h^2 - (x^2)_{av}/2h^2 + [\sigma(\theta_o)/\sigma(\theta_o)][-x_{av}/h + c_o (y^2)_{av}/2S_o R_o^2 \qquad (A.20)^*$$

$$- c_o (x^2)_{av}/S_o R_o h] + (\sigma''(\theta_o)/\sigma(\theta_o))(b^2/6h^2 + (x^2)_{av}/2h^2)\Big\}$$

for the yield, where $x_{av} = A^{-1} \int x\, dS$, $x^2_{av} = A^{-1} \int x^2\, dS$, and $y^2_{av} = A^{-1} \int y^2 dS$.

Noting from Equation A.20 that if $b^2/6h^2 << 1$, one can use

$$Nn(R_o S_o)^{-1} A\, \sigma(\theta_o)\, 2bh^{-1} \qquad (A.21)$$

except for small values of S_o, an attempt is made to design the slit

*Equation A.20 differs from Breit (1939) in that the $x^2/2h^2$ term should have a minus sign instead of the plus Breit et al. (1939) give .

system so that (A.21) is valid at all angles. In considering the additional terms in (A.20), it is seen that terms without s_o in the denominator can be neglected at small angles and, in addition, x_{av} terms are zero if the slit is symmetric. Furthermore, it can be assumed that Rutherford scattering is the primary contributor to the scattering at small angles and has the cross section

$$\sigma(\theta_o) = C/\theta_o^4 \qquad (A.22)$$

where C is a constant. Then for a rectangular slit with half width b, one obtains

$$x_{av} = \frac{1}{b}\int_o^b x\,dx = \frac{b}{2} \qquad (A.23)$$

$$x_{av}^2 = \frac{1}{b}\int_o^b x^2 dx = \frac{b^2}{3} \qquad (A.24)$$

$$y_{av}^2 = \frac{\ell^2}{12} \qquad (A.25)$$

where ℓ is the length of the rear slit. Substituting Equations A.22 through A.25 in A.20, equating (A.20) to (A.21), and neglecting $b^2/6h^2$, one obtains

$$(\ell/2b)^2 = 2(5h^2)^{-1}(h^2 + 4R_o h + 20\,R_o^2) \qquad (A.26)$$

Also, this equation has been derived with a high degree of accuracy by Silverstein (1959). The high order corrections resulting from Silverstein's derivation are insignificant in comparison to the accuracy of this experiment.

APPENDIX B

Sample Calculation for Data Reduction

Run #23 on February 13, 1962 will be used in the sample calculation. The nominal energy of this run is 5 Mev. and the spectrum is plotted in Figure 11. We use Equations 3 through 9 and first calculate

$$G = 2b_1A/R_oh = .08145 \times 1040875 \times 2.54/4.79 \times 2.3325 = 7.57 \times 10^{-4} \text{ cm.}$$

$$N = V \times t \times 60/R \times 1.602 \times 10^{-19} = .04901 \times 5.023 \times 60/.9985 \times 10^{6} \times 1.602 \times 10^{-19} = 9.234 \times 10^{13} \text{ particles}$$

$$n = 6.5839 \times 10^{18} \times P/T$$

$$P/T = .07911$$

The value of Y_s is obtained by subtracting N' from M' + N' and correcting with the ratio of clock time over live time

$$Y_s = M' \times 337/333 = (13756 - 360) \times 337/333$$

and the value of Y_r is obtained by subtracting N from M + N and correcting with the ratio of clock time over live time

$$Y_r = M \times 337/333 = (16028 - 1200) \times 337/333$$

The value for θ_{cm} is found for $\theta_{lab} = 35°$ and $M_1/M_2 = 0.5$ in Marion and Ginzbarg (1949) and is equal to 51.67°. The value of $d\Omega_{lab}/d\Omega_{cm}$ for this angle is .5122 and $\sin \theta_{lab} = 0.57358$. Combining these quantities according to Equation 3, we get $(d\sigma/d\Omega)_{cm} = .1093$ barns/ster.

at 51.67° c.m. For the recoil particle, we are able to find θ_{cm} by subtracting 2 x θ_{lab} from 180°, which gives θ_{cm} = 110°. Using $\tan\theta_{lab}$ = .70021, we get $(d\sigma/d\Omega)_{cm}$ = 0.0719 barns/ster. for 110° c.m.

The value for the corrected energy of 4.955 MeV is found in Table III for 5 Mev deuterons on 5000 Å nickel foil and 23.6 cm oil.

The relative error on the differential cross-section in the case of the scattered particle is obtained by noting that the vector sum of $\sqrt{(M' + 2N' + (N')^2/16)}$ = 1.11% and

$$[\sin(\theta_{lab} + \sqrt{2} \times .1)(d\Omega_{lab}/d\Omega_{cm})_{\theta_{lab}+\sqrt{2}\times.1} - \sin\theta_{lab}(d\Omega_{lab}/d\Omega_{cm})_{\theta_{lab}}]/$$

$$\sin\theta_{lab}(d\Omega_{lab}/d\Omega_{cm})$$

$$= .306 \times \sqrt{2}\ \%$$

give an rms error of ± 1.0% for σ_r when rounded off. In the case of the recoil particle, we get $M + 2N + N^2/16$ = 2.21% and

$$[\tan(\theta_{lab} + \sqrt{2} \times .1 - \tan\theta_{lab}]/\tan\theta_{lab} = \sqrt{2} \times .408\%$$

when added vectorially and rounded off, give an rms error of ± 2.0% for σ_s. The error in dead time correction and the error in the yield due to an uncertainty in the laboratory angle is not significant at this data point.

On this date, the energy was known to be better than 3/1000, which gives an rms error of ± .015 MeV.

APPENDIX C

Differential Cross-Section as a Function of the Elements of the Collision Matrix

The derivation of the general equation can be found in many dissertations (Sachs 1953). The analysis is made possible by the short-range nature of the nuclear force. This enables one to solve the Schrödinger equation without a detailed knowledge of the form of the nuclear potential, in that the solutions are outside the range of the potential. Because of this, it is only necessary to include the long-range Coulomb potential explicitly. The asymptotic solution of the wave function is indeterminate within phase factors in its exponential representation. These phase factors are called phase shifts and their values are caused by the nuclear force that shifts their values from what they would be in the absence of a nuclear potential (Evans 1955).

In the collision matrix representation of the differential cross-section, it is possible to set up the wave function for the scattering process by considering the asymptotic solutions to the Schrödinger wave equation, both the incoming part due to the incident beam and an outgoing part, proportional to the elements of the collision matrix, due to scattering. Since the ultimate goal is to represent the elements of the collision matrix with a finite number of phase shifts in an open form, it is necessary to extract the Rutherford part, which is dependent on all ℓ

values. It is then possible, after proper normalization, to identify the differential cross-section with the square of the absolute value of the outgoing amplitude. The result is

$$(d\sigma/d\Omega)_{\sigma\sigma'} = (\pi/k_\sigma^2)\Big|\sum_{\ell,\ell'} i^{\ell-\ell'}(2\ell+1)^{\frac{1}{2}}\exp(\tfrac{1}{2}i(\alpha_\ell+\alpha_{\ell'}))(U-I)_{ss'}Y_{\ell'}^{m'}(\sigma') + i\frac{R_\sigma}{\sqrt{\pi}}\delta_{\sigma\sigma'}\Big|^2 \qquad (C.1)$$

which is the same as Equation 10.11 of Sachs (1953) with $\alpha_\ell = 2(\eta_\ell - \eta_o)$ and $R_\sigma = \pi^{\frac{1}{2}} e^{-2i\eta_o}\rho_\sigma$.

$\alpha_\ell = 2\sum_{s=1}^{\ell} \tan^{-1}(\frac{\eta}{s})$ the Coulomb phase shift with $\alpha_o \equiv 0$

$\eta = zz' e^2/\hbar v$

z is the atomic number of the incident particle

z' is the atomic number of the target particle

e is the charge of the electron

$\hbar$ is Planck's constant divided by 2π

k is the wave number in the center of mass

ℓ is the orbital quantum number

U is the collision matrix

I is the unit matrix

$Y_\ell^{m'}(\sigma)$ is the spherical harmonic of the outgoing wave given by Galonsky and McEllistrem(1955a)

$$Y_{\ell'}^{m'}(\sigma) = (-1)^{\frac{1}{2}(m' + |m'|)} \left[\frac{2\ell' + 1}{4\pi} \frac{(\ell' - |m'|)!}{(\ell' + |m'|)!} \right]^{\frac{1}{2}}$$

$$\times \sin^{|m'|} e^{i m' \varphi} \frac{d^{(m')} P_{\ell}(\cos \theta)}{d(\cos \theta)^{|m'|}} \qquad (C.2)$$

where

$$P_{\ell}(x) = \frac{1}{2^{\ell} \ell!} \frac{d^{\ell}(x^2 - 1)^{\ell}}{d x^{\ell}} \qquad (C.3)$$

σ is the identity of the particle, including spin orientation

s denotes ℓ and m as well as σ

primes refer to outgoing particles

unprimes refer to incoming particles

The Rutherford amplitude of the incident wave

$R_{\sigma} = -\frac{1}{2}\eta \csc^2(\theta/2) \exp(i\eta \ln \csc^2(\theta/2))$

In Equation C.1, the U's are in an (S, ℓ, m_S, m_{ℓ}) representation. In order to finally evaluate the elements of U, it is necessary to make the transformation to an (S, ℓ, J, m_J) representation (Blatt and Biedenharn 1952). This is accomplished by considering

$$\Psi_J^{m_J} = i^{\ell + S - J} \sum_{m_{\ell} + m_S = m_J} (J, m_J, \ell, S / m_{\ell}, m_S, \ell, S) Y_{\ell}^{m_{\ell}} \chi^{m_S} \qquad (C.4)$$

which is the coupling of the eigenfunctions of the spin operator and the orbital angular momentum operators to form a wave function that is an eigenfunction of the total angular momentum which is a conserved

quantity in the elastic scattering interaction. Equation C.4 is suggested by Sachs (1953) in his Appendix 3 and differs from that of Blatt and Biedenharn in the phase factor $i^{\ell + S - J}$ where $(J, m_J, \ell, S/m_\ell, m_S, \ell, S)$ is the representation for Clebsch-Gordan coefficients defined by Condon and Shortley (1935). This modification is necessary for the preservation of invariance under time reversal.* Upon the conversion of $\langle S', \ell', m_S', m_\ell' | U | S, \ell, m_S, m_\ell \rangle$ to $\langle \Psi_{J'}^{m_{J'}\dagger} | U | \Psi_J^{m_J} \rangle$ a factor of $i^{\ell - \ell'}$ arises where $\ell - \ell' = 0, \pm 2$ in the case of d-He^4 elastic scattering. This, when multiplied by $i^{\ell - \ell'}$ originally in Equation C.1, gives $i^{0, \pm 4}$, which in all cases equals 1.

---

*Invariance under time reversal was neglected by Galonsky and McEllistrem (1952a), which means the off-diagonal elements of their collision matrix have the wrong signs. This oversight was of no consequence in their case, in that they assumed they could neglect the off-diagonal elements and would also be inconsequential in this dissertation, since the sign could be absorbed in the phase of the coupling parameter (Appendix A).

The invariance under time reversal concept is then academic, but yet interesting. This is discussed in Baldin et al. (1961). §, 21, the upshot of which is in using the time reversal operation in quantum mechanics, we should get effects similar to that in classical mechanics. For instance, if we have a dynamic equation that has proceeded according to Newton's postulates, we should be able to retrace our steps by replacing quantities such as position x by x and velocity v by -v. In the case of magnetic field, it can be resolved, with a little thought, that the field would have to be inverted in the time reversed equation for a charged particle to retrace its steps.

It can be shown (Wigner 1932) that time reversal in quantum mechanics is equivalent to an operation on the operator $\hat{O}$ of $\hat{K}\hat{V}^\dagger\hat{O}\hat{V}\hat{K}$, where $\hat{V}$ is a unitary matrix, $\hat{V}^\dagger$ its hermetian adjoint, and $\hat{K}$ is the complex conjugate operation. It is also shown in Baldin et al. (1961) that an operation on the eigenfunction of $VK\Psi_o$ is equivalent to operating on $\hat{O}$. Furthermore, it can be shown that for rotational operators such as the angular momentum operator $\hat{L}_z$, analogous to the situation in classical mechanics, the operation $\hat{K}\hat{V}^\dagger\hat{L}_z VK = -\hat{L}_z$.

Upon specializing the equation to d-He^4 elastic scattering and defining the parameters A through E in terms of $(d\sigma/d\Omega)_{m_S', m_S}$, one obtains

$$k^2(d\sigma/d\Omega)_{+1,+1} = k^2(d\sigma/d\Omega)_{-1,-1} = |A|^2 \tag{C.5}$$

$$k^2(d\sigma/d\Omega)_{0,0} = |B|^2 \tag{C.6}$$

$$(k^2/\sin^2\theta)(d\sigma/d\Omega)_{+1,0} = (k^2/\sin^2\theta)(d\sigma/d\Omega)_{-1,0} = |C|^2/2 \tag{C.7}$$

$$(k^2/\sin^2\theta)(d\sigma/d\Omega)_{0,+1} = (k^2/\sin^2\theta)(d\sigma/d\Omega)_{0,-1} = |D|^2/2 \tag{C.8}$$

$$(k^2/\sin^4\theta)(d\sigma/d\Omega)_{+1,-1} = (k^2/\sin^4\theta)(d\sigma/d\Omega)_{-1,+1} = |E|^2/2 \tag{C.9}$$

In order to obtain the differential cross-section for an unpolarized beam, we must sum the above equations over the outgoing channels and average over the incoming ones, which gives

$$3k^2(d\sigma/d\Omega) = 2|A|^2 + |B|^2 + \sin^2\theta \left\{ |C|^2 + |D|^2 \right\} + \sin^4\theta \left\{ |E|^2 \right\} \tag{C.10}$$

where

$$\begin{aligned} A = R + \sum_{\ell} (e^{\frac{1}{2}i\alpha_\ell}/4i) \Big\{ & e^{\frac{1}{2}i\alpha_\ell} P_\ell \left[(\ell+2) U_{\ell,\ell}^{\ell+1} + (2\ell+1) U_{\ell,\ell}^{\ell} \right. \\ & + (\ell-1) U_{\ell,\ell}^{\ell-1} - 2(2\ell+1) \Big] + e^{\frac{1}{2}i\alpha_{\ell+2}} P_{\ell+2} \left[(\ell+1)(\ell+2) \right]^{\frac{1}{2}} U_{\ell,\ell+2}^{\ell+1} \\ & + e^{\frac{1}{2}i\alpha_{\ell-2}} P_{\ell-2} \left[\ell(\ell-1) \right]^{\frac{1}{2}} U_{\ell,\ell-2}^{\ell-1} \Big\} \end{aligned} \tag{C.11}$$

$$B = R+\sum_{\ell} (e^{\frac{1}{2}i\alpha_\ell}/2i) \Big\{ e^{\frac{1}{2}i\alpha_\ell} P_\ell[(\ell+1)U_{\ell,\ell}^{\ell+1} + \ell\, U_{\ell,\ell}^{\ell-1} - (2\ell+1)]$$

$$- e^{\frac{1}{2}i\alpha_{\ell+2}} P_{\ell+2}[(\ell+1)(\ell+2)]^{\frac{1}{2}} U_{\ell,\ell+2}^{\ell+1} - e^{\frac{1}{2}i\alpha_{\ell-2}} P_{\ell-2}$$

$$+ [\ell(\ell-1)]^{\frac{1}{2}} U_{\ell,\ell-2}^{\ell-1} \Big\} \qquad (C.12)$$

$$C = \sum_{\ell} (e^{\frac{1}{2}i\alpha_\ell}/2i) \Big\{ [e^{\frac{1}{2}i\alpha_\ell} P_\ell'/\ell(\ell+1)] [\ell(\ell+2)\, U_{\ell,\ell}^{\ell+1} - (2\ell+1)\, U_{\ell,\ell}^{\ell}$$

$$- (\ell^2-1)\, U_{\ell,\ell}^{\ell-1}] + e^{\frac{1}{2}i\alpha_{\ell+2}} P_{\ell+2}' [(\ell+1)/(\ell+2)]^{\frac{1}{2}} U_{\ell,\ell+2}^{\ell+1}$$

$$+ e^{\frac{1}{2}i\alpha_{\ell-2}} P_{\ell-2}' [\ell/(\ell-1)]^{\frac{1}{2}} U_{\ell,\ell-2}^{\ell-2} \Big\} \qquad (C.13)$$

$$D = \sum_{\ell} (e^{\frac{1}{2}i\alpha_\ell}/2i) \Big\{ e^{\frac{1}{2}i\alpha_\ell} P_\ell' [U_{\ell,\ell}^{\ell+1} - U_{\ell,\ell}^{\ell-1}] + e^{\frac{1}{2}i\alpha_{\ell+2}} P_{\ell+2}'$$

$$\times [(\ell+1)/(\ell+2)]^{\frac{1}{2}} U_{\ell+2}^{\ell+1} - e^{\frac{1}{2}i\alpha_{\ell-2}} P_{\ell-2}' [\ell/(\ell-1)]^{\frac{1}{2}} U_{\ell,\ell-2}^{\ell-1} \Big\} \qquad (C.14)$$

$$E = \sum_{\ell} (e^{\frac{1}{2}i\alpha_\ell}/2\sqrt{2}\,i) \Big\{ [e^{\frac{1}{2}i\alpha_\ell} P_\ell''/\ell(\ell+1)] [\ell(U_{\ell,\ell}^{\ell+1} - (2\ell+1)\, U_{\ell,\ell}^{\ell}$$

$$+ (\ell+1)\, U_{\ell,\ell}^{\ell-1}] + (e^{\frac{1}{2}i\alpha_{\ell+2}}/[(\ell+1)(\ell+2)]^{\frac{1}{2}}) P_{\ell+2}'' U_{\ell,\ell+2}^{\ell+1}$$

$$+ (e^{\frac{1}{2}i\alpha_{\ell-2}}/[\ell(\ell-1)]^{\frac{1}{2}}) P_{\ell-2}'' U_{\ell,\ell-2}^{\ell-1} \Big\} \qquad (C.15)$$

where $U_{\ell,\ell'}^{J}$ is the element of the scattering matrix, conserving J and going from an incident channel ℓ to a final channel ℓ'.

APPENDIX D

Single Level Formulas

In this appendix, the formulas used in the single level approximation to each of the resonances will be presented. The formulas, when used for those ℓ-values through which there are reactions in addition to elastic scattering, are rather poor approximations to the data of this dissertation, in that the reaction channels are neglected in the formulas. The single level analysis, which is valid for resonances removed from others of the same $J\pi$, results from the following (Galonsky and McEllistrem 1955a).

$$U^{\ell}_{\ell,\ell} = \exp[2i(\varphi_\ell + \beta^\ell)], (J = \ell) \tag{D.1}$$

$$U_{\ell,\ell\pm1}^{\ell\pm1} = e^{2i\varphi_\ell}\left(\frac{\Gamma_{\lambda,\ell\pm2}}{\Gamma_\lambda} + \frac{\Gamma_{\lambda,\ell}}{\Gamma_\lambda}\exp^{(2i\beta^{\ell\pm1})}\right), (J=\ell\pm1) \tag{D.2}$$

$$U_{\ell\pm2}^{\ell\pm1} = U_{\ell,\ell\pm2}^{\ell\pm1} = e^{i(\varphi_\ell+\varphi_{\ell\pm2})}\frac{(\Gamma_{\lambda,\ell}\Gamma_{\lambda,\ell\pm2})^{\frac{1}{2}}}{\Gamma_\lambda}$$

$$\times\ 2i\sin\beta^{\ell\pm1}\exp(i\beta^{\ell\pm1}),\ (J=\ell\pm1) \tag{D.3}$$

$$\tan\beta^J = (\Gamma_\lambda/2)/(E_R-E), (\Gamma_\lambda = \Gamma_{\lambda,\ell} \text{ for } J=\ell$$

$$\Gamma_\lambda = \Gamma_{\lambda,\ell} + \Gamma_{\lambda,\ell\pm2} \text{ for } J=\ell\pm1) \tag{D.4}$$

$$\Gamma_{\lambda,\ell}/2 = (k\gamma_{\lambda,\ell}^{\ 2})/A_\ell^{\ 2} \tag{D.5}$$

$$E_R = E_\lambda + \Delta_\lambda \tag{D.6}$$

$$\Delta_\lambda = -\frac{\gamma_{\lambda,\ell}}{a}[g_\ell + \ell] \text{ for } J=\ell \tag{D.7}$$

$$\Delta_\lambda = -\frac{\gamma_{\lambda,\ell}^2}{a}\left[g_\ell + \ell\right] - \frac{\gamma_{\lambda,\ell\pm 2}^2}{a}\left[g_{\ell\pm 2} + \ell\pm 2\right] \text{ for } J = \ell\pm 1 \tag{D.8}$$

$$g_\ell = \frac{d(\ln A_\ell)}{d(\ln (ka))} \tag{D.9}$$

$$\tan \varphi_\ell = -\left(F_\ell / G_\ell\right)_a \tag{D.10}$$

where

$\gamma_{\lambda,\ell}^2$ is the reduced width of the λ level leading to the decay of the Li^6 state into a deuteron and alpha particle

ℓ is the relative orbital angular momentum

$\Gamma_{\lambda,\ell}$ is proportional to the probability for decay

$\frac{1}{A_\ell^2}$ is an inhibiting Coulomb and centrifugal barrier factor $= \frac{1}{F_\ell^2 + G_\ell^2}$

F_ℓ is the regular Coulomb function

G_ℓ is the irregular Coulomb function

k is the wave number

φ_ℓ is the hard-sphere scattering phase shift

β^J is the resonance scattering phase shift

$U_{\ell,\ell'}^J$ is an element of the scattering matrix

a is the interaction radius in the scattering

From Equations D.4, D.5, D.6, and D.7, one obtains

$$E_\lambda - \frac{\gamma_{\lambda,\ell}^2}{a}\left[g_\ell + \ell + \frac{ka}{A_\ell^2 \tan\beta^J}\right] = E \qquad \text{(D.11)}$$

The above equation was used to fit the phase shifts obtained from the phase shift analysis with the assumption that $\delta_\ell^J = \varphi_\ell + \beta_\ell^J$. The parameters g_ℓ and φ_ℓ were computed, using Equations D.9 and D.10, from a knowledge of the regular and irregular Coulomb functions.

The limitations of Equation D.11 are worth repeating. In using (D.11), we are in effect ignoring the possibility of tensor force coupling or reactions through channels other than elastic scattering, both of which are only approximately true in this dissertation.

APPENDIX E

Tensor Polarization Parameters

The tensor invariants of the double scattering process, which are tabulated in Tables X through XXIII, will be discussed and presented in this appendix. The outgoing wave in elastic scattering of a polarized beam is in a mixed state and can be represented as a linear combination of the pure states $\chi^s_{m_s}$ (Pondrom 1959),

$$\Psi(m_s) = \sum_{m_s'} \langle m_s | M | m_s' \rangle \ \chi^s_{m_s'} \qquad \text{(E.1)}$$

where

$\Psi(m_s)$ is the outgoing wave

$\chi^s_{m_s'}$ is the eigenfunction of the Schrödinger wave equation with the operator S_z

m_s is the eigenvalue of the spin projection of the polarized beam in the initial state

m_s' is the projection on the z axis of the spin s

$\langle m_s | M | m_s' \rangle$ is the transition amplitude from state m_s to state m_s'

In that the dimension of the spin space is three for d-He^4 elastic scattering, it is possible to characterize the density matrix in terms of a linear combination of nine (3^2) irreducible Hermetian operators T_{JM} (Lakin 1955), which must be chosen to satisfy the commutators (Racah 1942)

$$[(J_x \pm i J_y),\ T_{JM}] = [(J \mp M)(J \pm M + 1)]^{\frac{1}{2}}\ T_{J,M\pm1} \qquad (E.2)$$

and

$$[J_z, T_{JM}] = M\ T_{JM} \qquad (E.3)$$

where

$$T_{JM}^{\dagger} = (-1)^M\ T_{J,-M} \qquad (E.4)$$

These operators transform like spherical harmonics with their normalization and orthogonality being chosen as

$$\mathrm{Tr}\ T_{JM}\ T_{J'M'}^{\dagger} = 3\delta_{JM,J'M'} \qquad (E.5)$$

As a result, one obtains a tensor of rank zero (the identity matrix), three tensors of rank one, and five tensors of rank two:

$$T_{11} = -\tfrac{1}{2}\sqrt{3}\,(S_x + i S_y) \qquad (E.6)$$

$$T_{10} = -\left(\frac{3}{2}\right)^{\frac{1}{2}} S_z \qquad (E.7)$$

$$T_{22} = \tfrac{1}{2}\sqrt{3}\,(S_x + i S_y)^2 \qquad (E.8)$$

$$T_{21} = -\tfrac{1}{2}\sqrt{3}\,[(S_x + i S_y) S_z + S_z (S_x + i S_y)] \qquad (E.9)$$

and

$$T_{20} = \left(\tfrac{1}{2}\right)^{\frac{1}{2}} (3 S_z^2 - 2) \qquad (E.10)$$

These are expressions for five of the matrices in terms of spin operator S, with the ones for negative M being determined from (E.4). The Equations E.6 through E.10 can be verified with (E.2), (E.3), and (E.5), realizing that the T's commute with the orbital part of the J's.

The representations of the spin operators can be obtained by defining

$$S_z = \begin{pmatrix} 1 & 0 & 0 \\ 0 & 0 & 0 \\ 0 & 0 & -1 \end{pmatrix}$$

and rotating this through $\pi/2$, for

$$S_x = \frac{1}{\sqrt{2}} \begin{pmatrix} 0 & 1 & 0 \\ 1 & 0 & 1 \\ 0 & 1 & 0 \end{pmatrix}$$

and finally, with the use of the commutator, $[S_z, S_x] = i S_y$

$$S_y = \frac{1}{\sqrt{2}} \begin{pmatrix} 0 & -i & 0 \\ i & 0 & -i \\ 0 & +i & 0 \end{pmatrix}$$

By considering Equation E. 1, the expectation value for the T's of a beam that is initially in the μ^{th} substate can be written as

$$\langle \mu | T | \mu \rangle = \sum_{\beta} \langle \beta | M^{\dagger} | \mu \rangle \langle \beta | T \sum_{\gamma} \langle \mu | M | \gamma \rangle | \gamma \rangle$$

$$= \sum_{\beta\gamma} \langle \beta | M^{\dagger} | \mu \rangle \langle \mu | M | \gamma \rangle \langle \beta | T' | \gamma \rangle$$

in the Dirac bra and ket notation. For a beam that is initially unpolarized, it is now necessary to average over the values of μ

$$\left\{ \frac{1}{2 s_i + 1} \sum \langle \mu | \mu \rangle \right\} \langle T \rangle = \frac{1}{2 s_i + 1} \sum_{\mu} \langle \mu | T | \mu \rangle$$

$$= \sum_{\beta\gamma} \left\{ \frac{1}{2 s_i + 1} \sum_{\mu} \langle \beta | M^{\dagger} | \mu \rangle \langle \mu | M | \gamma \rangle \right\} \langle \beta | T | \gamma \rangle$$

which gives

$$\langle T \rangle = \frac{1}{Tr\rho} \sum_{\beta,\gamma} \rho_{\beta\gamma} T_{\beta\gamma} \qquad \text{(E.11)}$$

where

$$\rho_{\beta\gamma} = \frac{1}{2 s_i + 1} \sum_{\mu} M_{\beta\mu}^{\dagger} M_{\mu\gamma} \qquad \text{(E.12)}$$

the $\beta\gamma$ element of the density matrix and $s_i = 1$, the initial spin state.

The value for M is

$$M = \begin{pmatrix} a & -g & e \\ f & b & -f \\ e & g & a \end{pmatrix}$$

where

$$a = A$$

$$b = B$$

$$g = \sin\theta\, C/\sqrt{2}$$

$$f = \sin\theta\, D/\sqrt{2}$$

$$e = \sin^2\theta\, E/\sqrt{2}$$

with A through E being defined in Appendix C, which results in

$$Tr\rho = \tfrac{2}{3}\left[|a|^2 + \tfrac{1}{2}|b|^2 + |g|^2 + |f|^2 + |e|^2 \right] \qquad \text{(E.13)}$$

$$i\langle T_{11}\rangle = (\sqrt{\tfrac{2}{3}}\,/\mathrm{Tr}\rho)\,[\mathrm{Im}(bf^*) + \mathrm{Im}(ge^*) + \mathrm{Im}(ag^*)] \qquad \text{(E.14)}$$

$$\langle T_{22}\rangle = -(\sqrt{\tfrac{1}{3}}\,/\,\mathrm{Tr}\rho)\,[2\,\mathrm{Re}\,(ae^*) - |f|^2] \qquad \text{(E.15)}$$

$$\langle T_{21}\rangle = -(\sqrt{\tfrac{2}{3}}\,/\mathrm{Tr}\rho)\,[\mathrm{Re}\,(bf^*) + \mathrm{Re}(e^*g) - \mathrm{Re}(ag^*)] \qquad \text{(E.16)}$$

$$\langle T_{20}\rangle = (\sqrt{\tfrac{2}{3}}\,/\mathrm{Tr}\rho)\,[|a|^2 + |f|^2 + |e|^2 - 2\,|g|^2 - |b|^2] \qquad \text{(E.17)}$$

$$\langle T_{10}\rangle = 0 \qquad \text{(E.18)}$$

APPENDIX F

Sample Calculation for the Data Analysis

In this appendix, a set of starting values for the phase shift analysis will be presented, using a program identical with that of Appendix G with one exception. The program in Appendix G forces the imaginary parts of the coupling parameter negative, whereas the program that is used for this sample forced this parameter positive.

The angular distribution of interest is that of 7.968 MeV. Some degree of analysis has already taken place, and it is now of interest to find the effect of starting the program with the real parts of the phase shifts equal to that of the best fit previously obtained, but with the departure from the previous fit by using $\text{Im } \delta_2^{\,3} < \text{Im } \delta_2^{\,2}$. In accord with the above, the values for the real parts are:

$$\delta_0^{\,1} = 60.41°$$

$$\delta_1^{\,2} = -15.5°$$

$$\delta_1^{\,1} = 25.8°$$

$$\delta_1^{\,0} = -15.5°$$

$$\delta_2^{\,3} = 171.25°$$

$$\delta_2^{\,2} = 136.19°$$

$$\delta_2^{\,1} = 111.09°$$

$$\epsilon = -1.28°$$

and the values for the imaginary parts are:

$$\delta_0^{\,1} = 0.0°$$

$$\delta_1^{\,2} = 0.0°$$

$$\delta_1^{\,1} = 3.0°$$

$$\delta_1^{\,0} = 0.0°$$

$$\delta_2^{\,3} = 16.0°$$

$$\delta_2^{\,2} = 22.0°$$

$$\delta_2^{\,1} = 5.0°$$

$$\epsilon = 0.0°$$

Case 2 of the program is chosen which does not affect the real parts, but does perturb the imaginary parts, resulting in:

$$\delta_0^{\,1} = 0.0°$$

$$\delta_1^{\,2} = 0.81°$$

$$\delta_1^{\,1} = 5.95°$$

$$\delta_1^{\,0} = 1.06°$$

$$\delta_2^{\,3} = 29.95°$$

$$\delta_2^{\,2} = 10.90°$$

$$\delta_2^{\,1} = 0.0°$$

$$\epsilon = 6.26°$$

Results for tensor polarization parameters and the total reaction cross-sections are also obtained, but will not be presented here.

Upon plotting the phase shift parameters at this and other energies, then fairing the data, one obtains the results tabulated in captions of the Figures 13 through 17. One also obtains the tensor polarization parameters tabulated in Table XXI.

It is now possible to calculate the level parameters of an energy level, e.g. the 2^+ level. It is decided to use 4.8 fermis for the interaction radius and it is now necessary to calculate φ_2, A_2^2, g_2, and k (Appendix D) using a Burroughs 220 program coded for this computation. It is then possible, using the values for the δ_2^2 phase shifts, to calculate $\beta_2^2 = \delta_2^2 - \varphi_2$. The value for the excitation energy is that at which $\beta_2^2 = 90°$. This energy is 4.57 MeV. Next, Equation D.11 is used for E_d = 3.0 to 6.0 MeV, and a series of seven simultaneous equations are formed by pairing each of these obtained with the one obtained at the resonating energy. This results in a total of seven values for $\frac{\gamma_{\lambda,\ell}^2}{a}$, ranging from 0.738 MeV to 1.083 MeV. The average of 0.981 MeV is used. On calculating the Wigner limit from

$$\frac{3}{2}\ \frac{\hbar^2}{\mu a}$$

one obtains

$$\theta_2^2 = \frac{\gamma_{\lambda,\ell}^2}{3/2\,\frac{\hbar^2}{\mu a}} = 0.481$$

APPENDIX G

Fortran Program for Data Analysis

This program is described in the section entitled "Outline of the Analysis" and is presented in an abridged version in Figure 12. In this treatment, a copy of the coding is presented along with a description of the input and the output format.

A definition of the input quantities is as follows:

NMAX is the total number of differential cross-sections in the angular distribution

IMAX is the number of starting parameters used, where the real and the imaginary parts of a phase shift are two parameters

KW is the control word, indicating the case desired; this can be 1 through 9 with the function of each case being described in the program comments

WGT is a weighting factor, that is set equal to one

T is the laboratory energy of the incident deuteron in MeV

SIGEX(N) is the experimental cross-section of the N^{th} piece of data

ANGLE(N) is the center of mass angle of the N^{th} piece of data

LMAX or MAXL is the maximum value of ℓ included in the iteration; this is coupled with the case chosen to some extent

DELTA(I) is the I^{th} parameter in the program and is equal to:

$\mathrm{Re}\,\delta_0^1$ I = 1

$\mathrm{Re}\,\delta_1^2$ I = 2

$\mathrm{Re}\,\delta_1^1$ I = 3

$\mathrm{Re}\,\delta_1^0$ I = 4

$\mathrm{Re}\,\delta_2^3$ I = 5

$\mathrm{Re}\,\delta_2^2$ I = 6

$\mathrm{Re}\,\delta_2^1$ I = 7

$\mathrm{Re}\,\varepsilon_1$ I = 8

$\mathrm{Re}\,\delta_3^3$ I = 9

$\mathrm{Re}\,\delta_3^2$ I = 10

$\mathrm{Re}\,\varepsilon_2$ I = 11

and to the imaginary parts of the above parameters for I + 25.

An abbreviated form of the final output results with each complete iteration. The final output has the total reaction cross-section resulting from s-wave alone, from s + p-waves, from s + p + d-waves, and from s + p + d + f-waves, if LMAX = 3. The tensor polarization parameters are printed out for each angle, as are the experimental and calculated

cross-sections. In addition, a χ^2 for the fit is given and the final DELTA(I) is presented in a column array.

The coding for the program follows:

```
CHE(D)HE CONTROL PROGRAM
I     DIMENSION D(25),SX(50),SA(50),SL(50,25),DELTA(25),SIGEX(25),
      1DDELTA(25),SIGCA(50),ANGLE(50),SLOPE(50,25),Z(50),R(50),
      2P(10,50),P1(10,50),P2(10,50),TEMP(50),DELTA2(25),
      3ELTA(25),Y(10),SIGCAS(50,25),DELTA3(25),DDELT3(25),
      4A(50),B(50),C(50),F(50),E(50),A1(50),B1(50),C1(50),D1(50),E1(50),
      5A2(50),B2(50),C2(50),D2(50),E2(50),A3(50),B3(50),C3(50),D3(50),
      6E3(50),U1(5),U2(5),U3(5),U4(5),U5(5),SANG(50),SANG2(50),SANG4(50)
      7CANG(50),CANG2(50),TRHO(50),T11(50),T22(50),T21(50),T20(50)
            DIMENSION ALPHA(10),WAVENO(2)
      COMMON D,IMAX,NMAX,SA,R,P,P1,P2,LMAX,Y,KW,WAVENO,ANGLE,
      1A,B,C,F,E,U1,U2,U3,U4,U5,SANG2,SANG4
      EQUIVALENCE (DELTA,D),(IMAX,MAXI),(NMAX,MAXN),(SIGCA,SA),
      1(SIGEX,SX),(SLOPE,SL),(WGT,W),(CHISQ,CIQ)
    90READ INPUT TAPE 5,200,NMAX,IMAX,KW,WGT,T,(SIGEX(N),ANGLE(N),
      1N =1,NMAX)
       I5 =IMAX/2
       I6 =26
       I7 =25+IMAX/2
       READ INPUT TAPE 5,201,LMAX,(DELTA(I),I=1,I5)
       READ INPUT TAPE 5,201,MAXL,(DELTA(I),I=I6,I7)
  200 FORMAT(3I4,2F10.5/(2F10.5))
  201 FORMAT(I4/(F10.5))
       DO 130 I=1,I5
       DELTA(I+25)=DELTA(I+25)/57.295780
  130 DELTA(I) =DELTA(I)/57.295780
       DO 131 N =1,NMAX
  131 ANGLE(N) =ANGLE(N)/57.295780
       GO TO (91,92,93,94,95,96,97,98,99),KW
C WIGGLE REAL PARTS OF DELTAS L=0-2 AND EPSILON 1 (8 PARAMETERS)
   91 IP1 = 1
       IP2 = IMAX/2
       IP3 = 1
       GO TO 1
   81 GO TO (21,31,52),KKW
  101 GO TO 2
  111 GO TO 4
C WIGGLE IMAGINARY PARTS OF DELTAS L=0-2 AND EPSILON 1 (8 PARAMETERS)
   92 IP1 =26
       IP2 =25+IMAX/2
       IP3 = 1
       GO TO 1
   82 GO TO (21,31,52),KKW
  102 GO TO 2
  112 GO TO 4
C WIGGLE REAL AND IMAG. PARTS OF DELTAS L=0-2 AND EPSILON 1 (16
C PARAMETERS)
   93 IP1=26-IMAX/2
       IP2 =25+IMAX/2
       IP3 =1
       GO TO 1
   83 I1 =IMAX/2
       DO 883 I =1,I1
       IP4 =25-IMAX/2+I
  883 D(IP4) =D(I)
       GO TO (21,31,52),KKW
  103 DO 903 I=1,I1
       IP4 =25-IMAX/2+I
  903 D(I)=D(IP4)
```

```
      GO TO 2
  113 I1=IMAX/2
      DO 913 I=1,I1
      IP4 =25-IMAX/2+I
      DO 913 N =1,NMAX
  913 SL(N,IP4)=SL(N,I)
      GO TO 4
C WIGGLE REAL AND IMAG. PARTS OF J=1,L=1,DELTA (2PARAMETERS)
   94 IP1 = 3
      IP2 =28
      IP3 =25
      GO TO 1
   84 GO TO (21,31,52),KKW
  104 GO TO 2
  114 GO TO 4
C WIGGLE REAL AND IMAG. PARTS OF J=3,L=3,DELTA (2 PARAMETERS)
   95 IP1 = IMAX/2
      IP2 =25+IMAX/2
      IP3 =25
      GO TO 1
   85 GO TO (21,31,52),KKW
  105 GO TO 2
  115 GO TO 4
C WIGGLE REAL AND IMAG. PARTS OF J=3,L=3,J=2,L=3,J=2,L=1,
C DELTAS (6 PARAMETERS)
   96 IP1 =36
      IP2 =41
      IP3 = 1
      GO TO 1
   86 D(36) =D(9)
      D(37) =D(10)
      D(38) =D(2)
      D(39) =D(34)
      D(40) =D(35)
      D(41) =D(27)
      GO TO (21,31,52),KKW
  106 D(9) =D(36)
      D(10) =D(37)
      D(2) =D(38)
      D(34) =D(39)
      D(35) =D(40)
      D(27) =D(41)
      GO TO 2
  116 DO 126 N = 1,NMAX
      SL(N,36) =SL(N,9)
      SL(N,37) =SL(N,10)
      SL(N,38) =SL(N,2)
      SL(N,39) =SL(N,34)
      SL(N,40) =SL(N,35)
  126 SL(N,41) =SL(N,27)
      GO TO 4
C WIGGLE REAL AND IMAG. PARTS OF J=3,L=3,J=2,L=3,J=2,L=1,
C DELTAS AND EPSILON 2 (8 PARAMETERS)
   97 IP1 =37
      IP2 =44
      IP3 = 1
      GO TO 1
   87 D(37) =D(9)
      D(38) =D(10)
```

```
      D(39) =D(11)
      D(40) =D(2)
      D(41) =D(34)
      D(42) =D(35)
      D(43) =D(36)
      D(44) =D(27)
      GO TO (21,31,52),KKW
  107 D(9) =D(37)
      D(10) =D(38)
      D(11) =D(39)
      D(2) =D(40)
      D(34) =D(41)
      D(35) =D(42)
      D(36) =D(43)
      D(27) =D(44)
      GO TO 2
  117 DO 127 N = 1,NMAX
      SL(N,37) =SL(N,9)
      SL(N,38) =SL(N,10)
      SL(N,39) =SL(N,11)
      SL(N,40) =SL(N,2)
      SL(N,41) =SL(N,34)
      SL(N,42) =SL(N,35)
      SL(N,43) =SL(N,36)
  127 SL(N,44) =SL(N,27)
      GO TO 4
C WIGGLE REAL AND IMAG. PARTS J=3,L=3,J=2,L=3,J=2,L=1,J=1,L=1
C DELTAS AND EPSILON 2 (10 PARAMETERS)
   98 IP1 =37
      IP2 =46
      IP3 = 1
      GO TO 1
   88 D(37) =D(9)
      D(38) =D(10)
      D(39) =D(11)
      D(40) =D(2)
      D(41) =D(3)
      D(42) =D(34)
      D(43) =D(35)
      D(44) =D(36)
      D(45) =D(27)
      D(46) =D(28)
      GO TO (21,31,52),KKW
  108 D(9) =D(37)
      D(10) =D(38)
      D(11) =D(39)
      D(2) =D(40)
      D(3) =D(41)
      D(34) =D(42)
      D(35) =D(43)
      D(36) =D(44)
      D(27) =D(45)
      D(28) =D(46)
      GO TO 2
  118 DO 128 N = 1,NMAX
      SL(N,37) =SL(N,9)
      SL(N,38) =SL(N,10)
      SL(N,39) =SL(N,11)
      SL(N,40) =SL(N,2)
```

```
      SL(N,41) =SL(N,3)
      SL(N,42) =SL(N,34)
      SL(N,43) =SL(N,35)
      SL(N,44) =SL(N,36)
      SL(N,45) =SL(N,27)
  128 SL(N,46) =SL(N,28)
      GO TO 4
C WIGGLE REAL AND IMAG. PARTS OF ALL DELTAS THRU L=2 AND ALSO J=3,L=3,
C J=2,L=2,DELTAS PLUS EPSILON 1 AND EPSILON 2
   99 IP1 =26-IMAX/2
      IP2 =25 +IMAX/2
      IP3 =1
      GO TO 1
   89 I1 =IMAX/2
      DO 889 I =1,I1
      IP4 =25-IMAX/2+I
  889 D(IP4)=D(I)
      GO TO (21,31,52),KKW
  109 DO 909 I=1,I1
      IP4 =25-IMAX/2+I
  909 D(I)=D(IP4)
      GO TO 2
  119 I1=IMAX/2
      DO 919 I=1,I1
      IP4 =25-IMAX/2+I
      DO 919 N =1,NMAX
  919 SL(N,IP4)=SL(N,I)
      GO TO 4
    1 CHISQI = 20.
      BETA =SQRTF((2.*T)/(2.*931.141))*(1.-(3.*T)/(4.*2.*931.141))
      WAVENO(1)=(2.*4.*BETA*1E-12*931.141)/(1.973E-11*(2.+4.))
      WAVENO(2) =0.0
      ETA =(2.*1.44E-13)/(1.973E-11*BETA)
      DO 252 N=1,NMAX
      ANG =SINF(ANGLE(N)/2.)
      ANG2=ANG*ANG
      TEM =ETA*LOGF(1./ANG2)
      N1 =N+50
      ANGLE(N1) =0.0
      Z(N)=COSF(TEM)
      Z(N+50)=SINF(TEM)
      TEM=-0.5*ETA/ANG2
      R(N)=TEM*Z(N)
  252 R(N+50)=TEM*Z(N+50)
      JMAX =LMAX +1
      JP2=JMAX+2
      DO 253 J =2,JP2
      JP =J -1
      ALPHA(1) =0.0
  253 ALPHA(J)=ALPHA(JP)+2.*ATANF(ETA/FLOATF(JP))
      DO 254 N =1,NMAX
      SANG(N)=SINF(ANGLE(N))
      SANG2(N)=SANG(N)*SANG(N)
      SANG4(N)=SANG2(N)*SANG2(N)
      CANG(N)=COSF(ANGLE(N))
      CANG2(N)=CANG(N)*CANG(N)
      JP2=JMAX+4
      P(1,N) =1.0
      P(2,N)=CANG(N)
```

```
      DO 254 J=3,JP2
      J1 =J-1
      J2 =J+1
      J3 =J-2
      AJ =J
      AJ1 =J1
2540P(J,N)=(2.*AJ1-1.)/AJ1*CANG(N)*P(J1,N)-(AJ1-1.)/AJ1*P(J3,N)
      DO 255 N =1,NMAX
      P1(1,N) =0.0
      P1(2,N) =1.0
      JP2=JMAX+3
      DO 255 J =3,JP2
      J1 =J-1
      J2 =J+1
      AJ =J
      AJ1 =J1
2550P1(J,N)=(AJ1*(AJ1+1.)/(2.*AJ1+1.))*(P(J1,N)-P(J2,N))/(1.-CANG2(N))
      DO 256 N=1,NMAX
      P2 (1,N) =0.0
      P2(2,N) =0.0
      P2(3,N) =3.0
      JP2=JMAX+2
      DO 256 J =4,JP2
      J1 =J-1
      J2 =J+1
      AJ =J
2560P2(J,N)=AJ1*(AJ1+1.)/(2.*AJ1+1.)*(P1(J1,N)-P1(J2,N))/(1.-CANG2(N))
     1+(2.*CANG(N)*P1(J,N))/(1.-CANG2(N))
      MAXJ =LMAX+3
      DO 257 J=1,MAXJ
      TEM=ALPHA(J)/2.
      Y(J)=COSF(TEM)
  257 Y(J+10)=SINF(TEM)
      KKW=1
      KKK=1
      RMS1=100.0
    2 CALL XSECT
      GO TO(8,8,8,8,8,8,8,8,8,8,8,8,8,100),KKK
    8 KKK=KKK+1
      CIQ=0.0
      DO 20 N=1,NMAX
   20 CIQ=CIQ+((SX(N)-SA(N))/(W*SX(N)))*((SX(N)-SA(N))/(W*SX(N)))
      GO TO (22,30),KKW
   30 GO TO(81,82,83,84,85,86,87,88,89),KW
   31 KKW=1
      IF(CIQ-CHISQI)22,22,23
   23 IF(ABSF(CIQ-CHISQI)-.05)22,22,25
   25 D(33)=-D(33)
      DELTA3(33)=-DELTA3(33)
      DDELT3(33)= -DDELT3(33)
      DO 24 I=IP1,IP2,IP3
      DDELTA(I)=.333*DDELT3(I)
      DELTA(I)=DELTA3(I)+DDELTA(I)
      DDELT3(I)=DDELTA(I)
      IF(I-26)24,43,43
   43 IF(D(I))39,24,24
   39 D(I)=0.0
   24 CONTINUE
      DELTA3(33)=-DELTA3(33)
```

```
      DDELT3(33)= -DDELT3(33)
      D(33)=-D(33)
      KKW=2
      GO TO (101,102,103,104,105,106,107,108,109),KW
C SLOPE
   22 DO 259 N=1,NMAX
  259 TEMP(N) =SIGCA(N)
      I5 =IMAX/2
      DO 260 I=1,I5
      IF(ABSF(DELTA(I))-.01/57.295780)32,33,33
   32 ELTA(I)=.01/57.295780
      GO TO 34
   33 ELTA(I)=1.01*DELTA(I)
   34 IF(ABSF(DELTA(I+25))-.01/57.295780)35,36,36
   35 ELTA(I+25)=.01/57.295780
      GO TO 37
   36 ELTA(I+25)=1.01*DELTA(I+25)
   37 DELTA2(I+25)=DELTA(I+25)
  260 DELTA2(I) =DELTA(I)
      DO 262 ILM=1,I5
      DELTA(ILM+25)=ELTA(ILM+25)
      CALL XSECT
      DO 264 NIL=1,NMAX
      SIGCAS(NIL,ILM+25)=SIGCA(NIL)
 2640SLOPE(NIL,ILM+25)=(SIGCAS(NIL,ILM+25)-TEMP(NIL))/(DELTA(ILM+25)-DE
     1LTA2(ILM+25))
      DELTA(ILM+25)=DELTA2(ILM+25)
      DELTA(ILM) =ELTA(ILM)
      CALL XSECT
      DO 261 NIL =1,NMAX
      SIGCAS(NIL,ILM) =SIGCA(NIL)
 2610SLOPE(NIL,ILM) =(SIGCAS(NIL,ILM) -TEMP(NIL))/(DELTA(ILM) -DELTA2(I
     1LM))
  262 DELTA(ILM) =DELTA2(ILM)
      I6 =26
      I7 =25+IMAX/2
      DO 263 N=1,NMAX
  263 SIGCA(N) =TEMP(N)
      GO TO (111,112,113,114,115,116,117,118,119),KW
    4 DO 11 I=IP1,IP2,IP3
      TEM=0.0
      DO 10 N=1,NMAX
   10 TEM=TEM+SL(N,I)*SL(N,I)
      DDELTA(I)=0.0
      DO 11 N=1,NMAX
   11 DDELTA(I)=DDELTA(I)+(SX(N)-SA(N))*SL(N,I)/TEM
      SUM = 0.0
      DO 15 I = IP1,IP2,IP3
   15 SUM = SUM + DDELTA(I) ** 2/FLOATF(((IP2 - IP1)/IP3) + 1)
      RMS = SQRTF (SUM)
      IF(RMS-RMS1)50,50,51
   50 RMS1=RMS
      GO TO 54
   51 KKW1=KKW
      KKW=3
      GO TO (81,82,83,84,85,86,87,88,89),KW
   52 D(33)=-D(33)
      DELTA3(33)=-DELTA3(33)
      DDELT3(33)= -DDELT3(33)
```

```
      DO 53 I=IP1,IP2,IP3
      DDELTA(I)=.333*DDELT3(I)
      DELTA(I)=DELTA3(I)+DDELTA(I)
      DDELT3(I)=DDELTA(I)
      IF(I-26)53,49,49
   49 IF(D(I))44,53,53
   44 D(I)=0.0
   53 CONTINUE
      DELTA3(33)=-DELTA3(33)
      DDELT3(33)= -DDELT3(33)
      D(33)=-D(33)
      KKW=KKW1
      GO TO(101,102,103,104,105,106,107,108,109),KW
   54 GO TO (81,82,83,84,85,86,87,88,89),KW
   21 WRITE OUTPUT TAPE 6,203,CHISQ,(DELTA(I),I=1,50)
      WRITE OUTPUT TAPE 6,204,RMS,(DDELTA(I),I=1,50)
  204 FORMAT(F10.5/(F10.5))
      IF(RMS-.1/57.295780)100,100,40
   40 IF(RMS-3./57.295780)42,42,41
   41 IF(RMS-20./57.295780)65,65,60
   42 KKW=2
      GO TO 65
   60 D(33)=-D(33)
       DELTA3(33)=-DELTA3(33)
      DDELTA(33)=-DDELTA(33)
      DDELT3(33)= -DDELT3(33)
      DO 77 I=IP1,IP2,IP3
      IF (ABSF(DDELTA(I))-10./57.295780)77,77,75
   75 IF(DDELTA(I))70,76,76
   70 DELTA3(I)=D(I)
      DDELT3(I)=-3./57.295780
      D(I)=D(I)-3./57.295780
      IF(I-26)77,45,45
   76 DELTA3(I)=D(I)
      DDELT3(I)=3./57.295780
      D(I)=D(I)+3./57.295780
      IF(I-26)77,45,45
   45 IF(D(I))46,77,77
   46 D(I)=0.0
   77 CONTINUE
      DDELTA(33)=-DDELTA(33)
      DELTA3(33)=-DELTA3(33)
      DDELT3(33)= -DDELT3(33)
      D(33)=-D(33)
      GO TO 3
   65 D(33)=-D(33)
      DDELTA(33)=-DDELTA(33)
      DO 66 I=IP1,IP2,IP3
      DELTA3(I)=D(I)
      DDELT3(I)=DDELTA(I)
      D(I)=D(I)+DDELTA(I)
      IF(I-26)66,47,47
   47 IF(D(I))48,66,66
   48 D(I)=0.0
   66 CONTINUE
      DELTA3(33)=-DELTA3(33)
      DDELT3(33)=-DDELT3(33)
      D(33)=-D(33)
    3 CHISQI=CIQ
```

```
      GO TO (101,102,103,104,105,106,107,108,109),KW
  101 DO 132 I=1,15
      DELTA(I+25)=57.295780*DELTA(I+25)
  132 DELTA(I) =57.295780*DELTA(I)
      DO 133 N =1,NMAX
  133 ANGLE(N) =ANGLE(N)*57.295780
C POLARIZATION TENSORS
      DO 301 N=1,NMAX
I     A1(N)=A(N)
I      B1(N)=B(N)
I     C1(N)=(.707,0.0)*SANG(N)*C(N)
I     D1(N)=(.707,0.0)*SANG(N)*F(N)
I     E1(N)=(.707,0.0)*SANG2(N)*E(N)
I     A2(N)=ABSF(A1(N))
I     B2(N)=ABSF(B1(N))
I     C2(N)=ABSF(C1(N))
I     D2(N)=ABSF(D1(N))
I     E2(N)=ABSF(E1(N))
I     TRHO(N)=(.667,0.0)*(A2(N)*A2(N)+(.5,0.0)*B2(N)*B2(N)+C2(N)*C2(N)+
     1D2(N)*D2(N)+E2(N)*E2(N))
      D1(N+50)=-D1(N+50)
      E1(N+50)=-E1(N+50)
I     B3(N)=B1(N)*D1(N)
I     C3(N)=C1(N)*E1(N)
I     E3(N)=A1(N)*E1(N)
      C1(N+50)=-C1(N+50)
I     A3(N)=A1(N)*C1(N)
      T11(N)=(1.414/(1.732*TRHO(N)))*(B3(N+50)+C3(N+50)+A3(N+50))
      T22(N)=(1./(1.732*TRHO(N)))*(2.*E3(N)-D1(N)*D1(N)-D1(N+50)*D1(N+50
     1))
      T21(N)=-(1.414/(1.732*TRHO(N)))*(B3(N)+C3(N)-A3(N))
I 301 T20(N)=((1.414,0.0)/((3.,0.0)*TRHO(N)))*(A2(N)*A2(N)+D2(N)*D2(N)+
     1E2(N)*E2(N)-(2.,0.0)*C2(N)*C2(N)-B2(N)*B2(N))
C REACTION XSECT
      IP10=LMAX+1
I     SIGRE=(0.0,0.0)
      DO 302 I=1,IP10
I     UA=ABSF(U1(I))
I     UB=ABSF(U2(I))
I     UC=ABSF(U3(I))
I     UD=ABSF(U4(I))
I     UE=ABSF(U5(I))
      X=I-1
I     OSIGRE=SIGRE+((3.141,0.0)/(WAVENO*WAVENO))*(((2.,0.0)*X+(1.,0.))-((
     12.,0.0)*X+(3.,0.0))/(3.,0.0)*UC*UC-((2.,0.0)*X+(1.,0.0))/(3.,0.0)*
     2UB*UB-(((2.,0.0)*X-(1.,0.0))/(3.,0.0))*UA*UA-(((2.,0.0)*X+(3.,0.0)
     3)/(3.,0.0))*UD*UD-(((2.,0.0)*X-(1.,0.0))/(3.,0.0))*UE*UE)
  302 WRITE OUTPUT TAPE 6,303,SIGRE,(ANGLE(N),T11(N),T22(N),T21(N),T20(N
     1),N=1,NMAX)
      WRITE OUTPUT TAPE 6,202,T,(ANGLE(N),SIGEX(N),SIGCA(N), N=1,NMAX)
      WRITE OUTPUT TAPE 6,203,CHISQ, (DELTA(I),I=1,50)
  202 FORMAT (1H125X20HPHASE SHIFT ANALYSIS///15X29HENERGY OF INCIDENT P
     1ARTICLE =F10.5///2X20HCENTER OF MASS ANGLE2X26HEXPERIMENTAL CROSS
     2SECTION2X24HCALCULATED CROSS SECTION///(5XF10.5,16XF10.5,18XF10.5)
     3///)
 2030FORMAT(5X7HCHISQ =F10.5///25X18HTOTAL PHASE SHIFTS///(30XF10.5))
 3030FORMAT(1H125X19HTENSOR POLARIZATION///15X29HTOTAL REACTION CROSS S
     1ECTION=F10.5///2X20HCENTER OF MASS ANGLE7X3HT119X3HT229X3HT219X3HT
     220///(5XF10.5,9XF10.5,2XF10.5,2XF10.5,2XF10.5))

      GO TO 9
      END
```

```
      SUBROUTINE XSECT
I     DIMENSION AA(5),AB(5),AC(5),BA(5),BB(5),BC(5),CA(5),CB(5),CC(5),
     1DA(5),DB(5),DC(5),EA(5),EB(5),EC(5),U1(5),U2(5),U3(5),U4(5),U5(5)
     2Z(25),A(50),B(50),C(50),F(50),E(50),DELTA(25),SIGCA(50),ANGLE(50)
     3R(50),P(10,50),P1(10,50),P2(10,50),Y(10),SANG2(50),SANG4(50)
      COMMON DELTA,IMAX,NMAX,SIGCA,R,P,P1,P2,LMAX,Y,KW,WAVEND,ANGLE,
     1A,B,C,F,E,U1,U2,U3,U4,U5,SANG2,SANG4
      DO 207 N =1,NMAX
      N1 =N+50
      JP2 =LMAX +1
      DO 207 J =1,JP2
      P(J,N1) =0.0
      P1(J,N1) =0.0
  207 P2(J,N1) =0.0
      GO TO(1,1,1,1,4,5,6,6,6),KW
    1 DO 10 I =1,7
      IP =I +25
   10 Z(I) =-2.*DELTA(IP)
      DO 11 I =26,32
      IP =I -25
   11 Z(I) =2.*DELTA(IP)
      Z(8) =DELTA(8)
      Z(33) =DELTA(33)
      IP9 =3
I   2 U3(2) =EXPF(Z(2))
I     U2(2) =EXPF(Z(3))
I     U1(2) =EXPF(Z(4))
I     U4(2) =(0.0,0.0)
I     U5(2) =(0.0,0.0)
I   3 U3(3) =EXPF(Z(5))
I     U2(3) =EXPF(Z(6))
I     CUS=COSF(Z(8))
I     SYN=SINF(Z(8))
I     XP1=EXPF(Z(1))
I      XP7=EXPF(Z(7))
I     U1(3)=(SYN*SYN)* XP1+ CUS*CUS* XP7
I     U4(3) =(0.0,0.0)
I     U5(3)=(.5,0.0)*(SINF((2.,0.0)*Z(8)))*( XP1- XP7)
I     U3(1)=CUS*CUS* XP1+SYN*SYN* XP7
I     U2(1) =(0.0,0.0)
I     U1(1) =(0.0,0.0)
I     U4(1)=U5(3)
I     U5(1) =(0.0,0.0)
      DO 100 N=1,IP9
I     X =N-1
I     AA(N) =((X+(2.,0.))*U3(N)+((2.,0.)*X+(1.,0.))*U2(N)+(X-(1.,0.))*U1
     1(N)-(2.,0.)*((2.,0.)*X  +(1.,0.)))
I     AB(N) =SQRTF((X+(1.,0.))*(X+(2.,0.)))*U4(N)
I     AC(N) =SQRTF(X*(X-(1.,0.)))*U5(N)
I     BA(N)=(X+(1.,0.))*U3(N)+X*U1(N)-((2.,0.)*X+(1.,0.))
I     BB(N) =SQRTF((X+(1.,0.))*(X+(2.,0.)))*U4(N)
I     BC(N) =SQRTF(X*(X-(1.,0.)))*U5(N)
I     CA(N) =(X*(X+(2.,0.))*U3(N)-((2.,0.)*X+(1.,0.))*U2(N)-(X**2-(1.,0.
     1))*U1(N))/(X*(X+(1.,0.)))
I     CB(N) =SQRTF((X+(1.,0.))/(X+(2.,0.)))*U4(N)
I     CC(N) =SQRTF(X/(X-(1.,0.)))*U5(N)
I     DA(N) =U3(N) -U1(N)
I     DB(N) =SQRTF((X+(1.,0.))/(X+(2.,0.)))*U4(N)
I     DC(N) =SQRTF(X/(X-(1.,0.)))*U5(N)
```

```
I      EA(N)=(X*U3(N)-((2.,0.)*X+(1.,0.))*U2(N)+(X+(1.,0.))*U1(N))/(X*
      1(X+(1.,0.)))
I      EB(N) =U4(N)/SQRTF((X+(1.,0.))*(X+(2.,0.)))
I  100 EC(N) =U5(N)/SQRTF(X*(X-(1.,0.)))
       GO TO 50
C CASE 5
     4 DO 20 I =1,7
       IP =I +25
    20 Z(I) =-2.*DELTA(IP)
       DO 21 I =26,32
       IP =I -25
    21 Z(I)  =2.*DELTA(IP)
       Z(8) =DELTA(8)
       Z(9) =-2.*DELTA(34)
       Z(33) =DELTA(33)
       Z(34) =2.*DELTA(9)
I      U3(4) =(0.0,0.0)
I      U2(4) =EXPF(Z(9))
I      U1(4) =(0.0,0.0)
I      U4(4) =(0.0,0.0)
I      U5(4) =(0.0,0.0)
       IP9 =4
       GO TO 2
C CASE 6
     5 DO 30 I =1,7
       IP =I +25
    30 Z(I) =-2.*DELTA(IP)
       DO 31 I=26,32
       IP =I -25
    31 Z(I) =2.*DELTA(IP)
       Z(8) =DELTA(8)
       Z(9) =-2.*DELTA(34)
       Z(10) =-2.*DELTA(35)
       Z(33) =DELTA(33)
       Z(34) =2.*DELTA(9)
       Z(35) =2.*DELTA(10)
I      U3(4) =(0.0,0.0)
I      U2(4) =EXPF(Z(9))
I      U1(4) =EXPF(Z(10))
I      U4(4) =(0.0,0.0)
I      U5(4) =(0.0,0.0)
       IP9 =4
       GO TO 2
C CASES 7-9
     6 DO 40 I =1,7
       IP =I +25
    40 Z(I) =-2.*DELTA(IP)
       DO 41 I=26,32
       IP =I-25
    41 Z(I) =2.*DELTA(IP)
       Z(8) =DELTA(8)
       Z(9) =-2.*DELTA(34)
       Z(10) =-2.*DELTA(35)
       Z(11) =DELTA(11)
       Z(33) =DELTA(33)
       Z(34) =2.*DELTA(9)
       Z(35) =2.*DELTA(10)
       Z(36) =DELTA(36)
I      SYN=SINF(Z(11))
```

```
I      CUS=COSF(Z(11))
I       XP2=EXPF(Z(2))
I       XP10=EXPF(Z(10))
I      U3(2)=CUS*CUS* XP2+SYN*SYN* XP10
I      U2(2) =EXPF(Z(3))
I      U1(2) =EXPF(Z(4))
I      U4(2)=(.50,0.0)*SINF((2.,0.0)*Z(11))*( XP10- XP2)
I      U5(2) =(0.0,0.0)
I      U3(4) =(0.0,0.0)
I      U2(4) =EXPF(Z(9))
I      U1(4)=CUS*CUS* XP10+SYN*SYN* XP2
I      U4(4) =(0.0,0.0)
I      U5(4)=U4(2)
       IP9 =4
       GO TO 3
   50  JMAX =LMAX +1
       DO 60 N =1,NMAX
I      A(N) =R(N)
I      B(N) =R(N)
I      C(N) =(0.0,0.0)
I      F(N) =(0.0,0.0)
I      E(N) =(0.0,0.0)
       DO 60 J =1,JMAX
       K =J +2
       IF(J-2)52,52,51
   51  M =J-2
       GO TO 53
   52  M =1
I  530A(N)=A(N)+Y(J)/(0.0,4.)*(Y(J)*P(J,N)*AA(J)+Y(K)*P(K,N)*AB(J)+Y(M)
     1*P(M,N)*AC(J))
I      B(N)=B(N)+Y(J)/(0.0,2.)*(Y(J)*P(J,N)*BA(J)-Y(K)*P(K,N)*BB(J)
     1-Y(M)*P(M,N)*BC(J))
I      C(N)=C(N)+Y(J)/(0.0,2.)*(Y(J)*P1(J,N)*CA(J)-Y(K)*P1(K,N)*CB(J)
     1+Y(M)*P1(M,N)*CC(J))
I      F(N)=F(N)+Y(J)/(0.0,2.)*(Y(J)*P1(J,N)*DA(J)+Y(K)*P1(K,N)*DB(J)
     1-Y(M)*P1(M,N)*DC(J))
I  600E(N)=E(N)+Y(J)/(0.0,2.828)*(Y(J)*P2(J,N)*EA(J)+Y(K)*P2(K,N)*EB(J)
     1+Y(M)*P2(M,N)*EC(J))
       DO 61 N =1,NMAX
I      AX=ABSF(A(N))
I      BX=ABSF(B(N))
I      CX=ABSF(C(N))
I      DX=ABSF(F(N))
I      EX=ABSF(E(N))
I   61 SIGCA(N)=((2.,0.)*AX*AX+BX*BX+SANG2(N)*(CX*CX+DX*DX)+SANG4(N)*EX*
     1EX)/((3.,0.)*WAVENO*WAVENO)
       RETURN
       END
```

REFERENCES

F. Ajzenberg-Selove and T. Lauritsen, 1959, Nuc. Phys. 11, 1.

K. W. Allen, E. Almqvist and C. B. Bigham, 1960, Proc. Phys. Soc. (London) 75, 913.

J. C. Allred, D. K. Froman, A. M. Hudson, and L. Rosen, 1951 Phys. Rev. 82, 786.

V. V. Balashov, 1959, Soviet Physics-JETP 9, 798.

A. M. Baldin, V. I. Goldanskiĭ, and I. L. Rozental , 1961, Kinematics of Nuclear Reactions (Oxford University Press, London).

J. M. Blatt and L. C. Biedenharn, 1952, Revs. Modern Phys. 24, 258.

J. M. Blatt and V. F. Weisskopf, 1952a, Theoretical Nuclear Physics (John Wiley and Sons, New York).

G. Breit, H. M. Thaxton, and L. Eisenbud, 1939, Phys. Rev. 55, 1018.

E. J. Burge, H. B. Burrows, and W. M. Gibson, 1952, Proc. Roy. Soc. (London) A210, 534.

E. U. Condon and G. H. Shortley, 1935, The Theory of Atomic Spectra (Cambridge University Press, Cambridge, England).

W. C. Dickinson and D. C. Dodder, 1953, Rev. Sci. Inst. 24, 428.

R. D. Evans, 1955, The Atomic Nucleus (McGraw-Hill Book Company, Inc., New York).

A. Galonsky, R. A. Douglas, W. Haeberli, M. T. McEllistrem, and H. T. Richards, 1955, Phys. Rev. 98, 586.

A. Galonsky and M. T. McEllistrem, 1955a, Phys. Rev. 98, 590.

J. L. Gammel, B. J. Hill, and R. M. Thaler, 1960, Phys. Rev., 119, 267.

W. Haeberli, 1963, (private communication).

R. L. Henkel, J. E. Perry, Jr., and R. K. Smith, 1955, Phys. Rev. 99, 1050.

R. D. Huntoon, A. Ellett, D. S. Bayley, and J. A. Van Allen, 1940, Phys. Rev. 58, 97.

D. R. Inglis, 1952, Phys. Rev. 87, 915.

D. R. Inglis, 1953, Revs. Modern Phys. 25, 390.

W. Lakin, 1955, Phys. Rev. 98, 139.

A. M. Lane and R. G. Thomas, 1958, Revs. Modern Phys. 30, 257.

T. Lauritsen, T. Huus, and S. G. Nilsson, 1953, Phys. Rev. 92, 1501.

T. Lauritsen and F. Ajzenberg-Selove, 1962, Energy Levels of Light Nuclei (National Academy of Sciences--National Research Council, Washington, D. C.).

H. W. Lefevre, R. R. Borchers, and C. H. Poppe, 1962, Phys. Rev. 128, 1328.

J. B. Marion and A. S. Ginzbarg, 1949, Tables for the Transformation of Angular Distribution Data from the Laboratory System to the Center of Mass System (Shell Development Company, Houston, Texas).

E. M. Pell, 1960, Jour. App. Phys. 31, 291.

R. J. N. Phillips, 1960, Proc. Phys. Soc. (London) 75, 317.

L. G. Pondrom, 1959, Phys. Rev. Letters 2, 346.

L. Puzikov, R. Ryndin, and J. Smorodinsky, 1957, Nuc. Phys. 3, 436.

G. Racah, 1942, Phys. Rev. 62, 438.

J. L. Russell, Jr., G. C. Phillips, and C. W. Reich, 1956, Phys. Rev. 104, 135.

B. V. Rybakov, V. A. Sidorov, and N. A. Viasov, 1961, Nuc. Phys. 23, 491.

R. G. Sachs, 1953, Nuclear Theory (Addison-Wesley Publishing Company, Inc.) Chap. 10, Appendix 3.

F. Seiler, S. E. Darden, L. C. McIntyre, and W. G. Weitkamp, 1962, Bull. Amer. Phys. Soc. 7, 531.

E. A. Silverstein, 1959, Nuclear Inst. and Meth. 4, 53.

H. P. Stapp, 1957, Phys. Rev. 107, 607.

L. Stewart, J. E. Brolley, Jr., and L. Rosen, 1962, Phys. Rev. 128, 707.

T. A. Tombrello, 1963, (private communication).

P. H. Wackman and N. Austern, 1962, Nuc. Phys. 30, 529.

W. Whaling, 1958, Handbuch der Physik 34, 193.

E. P. Wigner, 1932, Göttingen Nachr. 32, 546.

K. Wildermuth, Y. C. Tang, F. C. Khanna, and L. D. Pearlstein, 1961, Proc. Rutherford Jubilee Int. Conf. (Manchester) p. 259.

H. R. Worthington, J. M. McGruer, and D. E. Findley, 1953, Phys. Rev. 90, 899.

Table I. Energy corrections for deuterium gas and 2500 Å nickel foil, with alpha particles incident. See text, p. 23.

Nominal Energy (MeV)	Corrected Energy	
	20 cm.-oil (MeV)	25 cm.-oil (MeV)
6.000	5.875	5.865
7.000	6.887	6.878
8.000	7.895	7.887
9.000	8.904	8.897
10.000	9.909	9.903
11.000	10.916	10.910
12.000	11.920	11.915

Table II. Energy corrections for helium gas and 2500 Å nickel foil, with deuterons as the incident particles. See text, p. 23.

Nominal Energy	Corrected Energy	
(MeV)	20 cm.-oil (MeV)	25 cm.-oil (MeV)
3.000		2.958
5.000	4.973	4.971
6.000	5.976	5.973
7.000	6.979	6.977
8.000	7.981	7.979
9.000	8.982	8.981
10.000	9.984	9.982
11.000	10.984	10.983
12.000	11.986	11.984

Table III. Energy corrections for helium gas and 5000 Å nickel foil, with deuterons as the incident particles. See text, p. 23.

Nominal Energy	Corrected Energy	
(MeV)	20 cm. oil (MeV)	25 cm. -oil (MeV)
5.000	4.956	4.954
6.000	5.962	5.960
7.000	6.966	6.964
8.000	7.969	7.967
9.000	8.971	8.970
10.000	9.974	9.972
11.000	10.975	10.974
12.000	11.977	11.975

Table IV. Systematic Errors

a. Error in Geometric Factor

$$G = 2bA/R_o h$$

Parameter	Error (percent)
2b	.4
A	.5
h	.005
R_o	.1
G	.648

b. Error in Charge Collection

$$N = Vt/R$$

Parameter	RMS Error (percent)
V	.02
t	.02
R	.1
N	.1039

c. Error in Particle Density

$$n \alpha (S.G.)p/T$$

Parameter	RMS Error (percent)
S.G.	.5
p	.2
T	.2
n	.574

d. Error in Approximating Cross-Section Equation

Parameter	RMS Error (percent)
$h^2/3h^2$	.0948

Probable angular independent systematic error = 1.0

See *text, pp.* 25ff.

Table V. Error due to $\sin\theta_{lab}\,(d\Omega_{lab}/d\Omega_{cm})$

θ_{lab} (degrees)	RMS Error (percent)
12.0	1.5
15.0	1.0
20.0	.5
25.0	.5
30.0	.5
40.0	.5
50.0	.5
55.0	.5
60.0	.5
65.0	.5
70.0	.5
80.0	.5
90.0	.5

See text, pp. 27ff.

Table VI. Error due to $\tan\theta_{lab}$

θ_{lab} (degrees)	RMS Error (percent)
12.0	1.0
15.0	1.0
20.0	1.0
25.0	.5
30.0	.5
35.0	.5
40.0	.5
45.0	.5
50.0	.5
55.0	.5
60.0	.5
65.0	.5
70.0	1.0

See text, pp. 27ff.

Table VII. Single level parameters for the 2^+ level in Li^6. The units of γ^2 tabulated here differ from those described in the text, p. 61 , in that the units of γ^2 in the text are MeV-cm.

Level	2^+
Interaction Radius	4.8 fermis
Reduced Width	0.981 MeV
Excitation Energy	$E_x = 4.57$ MeV
Ratio to Wigner Limit	$\theta_2^2 = \gamma_2^2 / (\frac{3h^2}{2\mu a^2}) = 0.481$

Table VIII. Single level parameters for the 1^+ level in Li^6. The units of γ^2 tabulated here differ from those described in the text, p. 61 , in that the units of γ^2 in the text are MeV-cm.

Level	1^+
Interaction Radius	4.8 fermis
Reduced Width	1.005 MeV
Excitation Energy	$E_x = 5.62$ MeV
Ratio to Wigner Limit	$\theta_2^2 = \gamma_2^2 / \left(\frac{3h^2}{2\mu a^2} \right) = 0.492$

Table IX. Single level parameters for the (1^-) level in Li^6. The units of γ^2 tabulated here differ from those described in the text, p. 61 , in that the units of γ^2 in the text are MeV-cm.

Level	(1^-)
Interaction Radius	3.5 fermis
Reduced Width	1.46 MeV
Excitation Energy	7.19 MeV
Ratio to Wigner Limit	$\theta_1^2 = \gamma_1^2 / (\frac{3\hbar^2}{2\mu a^2}) = 0.380$

Table X

Tensor Polarization Parameters at E_d = 2.935 MeV

Center of Mass Angle (degrees)	i⟨T11⟩	⟨T22⟩	⟨T21⟩	⟨T20⟩
50.00000	-0.21539	0.17050	-0.12616	0.17335
60.00000	-0.21781	0.22571	-0.17298	0.23764
70.00000	-0.16706	0.25059	-0.16429	0.24186
80.00000	-0.08516	0.23897	-0.09963	0.20701
90.00000	-0.00000	0.20078	-0.00000	0.16391
100.00000	0.07094	0.15332	0.10728	0.13979
110.00000	0.12328	0.10957	0.20168	0.14972
120.00000	0.15830	0.07475	0.27117	0.19698
130.00000	0.17668	0.04893	0.30878	0.27625

See Appendix E.

Table XI

Tensor Polarization Parameters at E_d = 3.441 MeV

Center of Mass Angle (degrees)	i ⟨T11⟩	⟨T22⟩	⟨T21⟩	⟨T20⟩
50.00000	-0.30038	0.05590	-0.19473	0.04515
60.00000	-0.29115	0.04639	-0.25485	0.06909
70.00000	-0.21385	0.02105	-0.24731	0.04863
80.00000	-0.08587	-0.03115	-0.15457	-0.01056
90.00000	0.04877	-0.10771	0.00820	-0.09101
100.00000	0.14725	-0.18261	0.18910	-0.14797
110.00000	0.19710	-0.22575	0.33440	-0.13686
120.00000	0.20910	-0.22595	0.41733	-0.04682
130.00000	0.19736	-0.19162	0.43648	0.09989

See Appendix E.

Table XII

Tensor Polarization Parameters at E_d = 3.946 MeV

Center of Mass Angle (degrees)	i ⟨T11⟩	⟨T22⟩	⟨T21⟩	⟨T20⟩
50.00000	-0.46372	-0.14906	-0.35867	-0.09362
60.00000	-0.46150	-0.19379	-0.40459	-0.17396
70.00000	-0.36301	-0.19658	-0.37163	-0.19340
80.00000	-0.16429	-0.18328	-0.23215	-0.16124
90.00000	0.05518	-0.23093	0.00390	-0.19194
100.00000	0.18752	-0.34575	0.25690	-0.30982
110.00000	0.21918	-0.42471	0.43492	-0.36225
120.00000	0.20129	-0.40889	0.50740	-0.26128
130.00000	0.16986	-0.32561	0.49509	-0.05796

See Appendix E.

Table XIII

Tensor Polarization Parameters at E_d = 4.450 MeV

Center of Mass Angle (degrees)	i ⟨T11⟩	⟨T22⟩	⟨T21⟩	⟨T20⟩
50.00000	-0.55956	-0.34878	-0.47930	-0.18838
60.00000	-0.57039	-0.38696	-0.51028	-0.36952
70.00000	-0.43249	-0.20628	-0.40434	-0.29023
80.00000	-0.19900	0.11591	-0.19712	0.03626
90.00000	-0.03876	0.25528	-0.00281	0.20536
100.00000	0.01260	0.10187	0.16581	0.04005
110.00000	0.02265	-0.17146	0.32647	-0.22840
120.00000	0.03653	-0.33745	0.43335	-0.30605
130.00000	0.05270	-0.33500	0.44916	-0.15860

See Appendix E.

Table XIV

Tensor Polarization Parameters at E_d = 4.731 MeV

Center of Mass Angle (degrees)	i ⟨T11⟩	⟨T22⟩	⟨T21⟩	⟨T20⟩
17.97000	-0.14381	-0.01744	-0.04886	0.07407
22.44000	-0.24087	-0.04998	-0.11815	0.17655
29.85000	-0.36355	-0.12856	-0.23415	0.21110
37.20000	-0.45742	-0.22611	-0.33416	0.11794
44.48000	-0.53952	-0.33307	-0.41986	-0.04554
51.67000	-0.59905	-0.42039	-0.48034	-0.23385
58.75000	-0.60164	-0.42357	-0.48781	-0.36690
65.70000	-0.51106	-0.26829	-0.41522	-0.33179
72.52000	-0.34561	0.02788	-0.28029	-0.09869
79.18000	-0.18610	0.32058	-0.14656	0.19117
85.66000	-0.08905	0.48752	-0.05260	0.37486
91.95000	-0.05243	0.50787	0.01017	0.40006
98.02000	-0.05071	0.41304	0.06491	0.29412
103.88000	-0.05991	0.24665	0.12719	0.11386
110.00000	-0.06419	0.04085	0.20455	-0.08926
120.00000	-0.04148	-0.22434	0.32222	-0.27404
130.00000	0.00016	-0.29733	0.36880	-0.19572
140.00000	0.02960	-0.23688	0.33876	0.01390
150.00000	0.03862	-0.14263	0.26719	0.21817
156.00000	0.03635	-0.09233	0.21606	0.31465

See Appendix E.

Table XV

Tensor Polarization Parameters at E_d = 4.955 MeV

Center of Mass Angle (degrees)	i ⟨T11⟩	⟨T22⟩	⟨T21⟩	⟨T20⟩
17.97000	-0.15703	-0.02388	-0.05794	0.14590
22.44000	-0.25265	-0.05881	-0.11962	0.22921
29.85000	-0.37442	-0.13899	-0.21776	0.23193
37.20000	-0.47219	-0.23839	-0.30271	0.12559
44.48000	-0.56014	-0.34730	-0.37571	-0.04124
51.67000	-0.62291	-0.43080	-0.42391	-0.22666
58.75000	-0.61728	-0.40954	-0.41754	-0.34301
65.70000	-0.50229	-0.19894	-0.33286	-0.26704
72.52000	-0.31469	0.15420	-0.20188	0.00957
79.18000	-0.15661	0.46793	-0.09411	0.31046
85.66000	-0.07796	0.63088	-0.03527	0.48255
110.00000	-0.12272	0.11603	0.10841	-0.00559
120.00000	-0.10398	-0.13298	0.21667	-0.24694
130.00000	-0.04741	-0.25566	0.28041	-0.22436
140.00000	0.00054	-0.22201	0.27329	-0.04236
150.00000	0.02272	-0.13780	0.22154	0.15093
156.00000	0.02567	-0.08993	0.18071	0.24399

See Appendix E.

Table XVI

Tensor Polarization Parameters at E_d = 5.473 MeV

Center of Mass Angle (degrees)	i ⟨T11⟩	⟨T22⟩	⟨T21⟩	⟨T20⟩
17.97000	-0.17616	-0.03055	-0.05391	0.19661
22.44000	-0.26990	-0.06473	-0.09147	0.23291
29.85000	-0.39091	-0.13888	-0.14543	0.19265
37.20000	-0.49130	-0.22973	-0.19005	0.08717
44.48000	-0.57917	-0.32589	-0.22521	-0.05248
51.67000	-0.62867	-0.38378	-0.23963	-0.18946
58.75000	-0.58113	-0.30789	-0.21278	-0.23489
65.70000	-0.40329	-0.02283	-0.14083	-0.08560
72.52000	-0.18526	0.35995	-0.06637	0.20430
79.18000	-0.05075	0.64040	-0.03146	0.44861
85.66000	-0.01762	0.76101	-0.03251	0.55836
91.95000	-0.04717	0.75913	-0.04859	0.54616
98.02000	-0.10397	0.67380	-0.06328	0.44459
103.88000	-0.16422	0.52941	-0.06630	0.28281
110.00000	-0.21306	0.33187	-0.05022	0.07716
120.00000	-0.22122	0.00216	0.01672	-0.20796
130.00000	-0.14736	-0.17820	0.08845	-0.27129
140.00000	-0.06399	-0.18630	0.11825	-0.15382
150.00000	-0.01349	-0.12233	0.10872	0.00138
156.00000	0.00111	-0.08098	0.09224	0.07951

See Appendix E.

Table XVII

Tensor Polarization Parameters at E_d = 5.961 MeV

Center of Mass Angle (degrees)	i ⟨T11⟩	⟨T22⟩	⟨T20⟩	⟨T20⟩
17.97000	-0.18780	-0.02905	-0.03447	0.15011
22.44000	-0.27465	-0.05693	-0.04938	0.14895
29.85000	-0.38263	-0.11510	-0.06576	0.09252
37.20000	-0.46943	-0.18548	-0.07581	0.00893
44.48000	-0.53725	-0.25742	-0.07975	-0.08524
51.67000	-0.54957	-0.28823	-0.07315	-0.15935
58.75000	-0.43812	-0.18637	-0.05252	-0.13836
65.70000	-0.19755	0.09853	-0.02913	0.03832
72.52000	0.02250	0.42313	-0.02546	0.27472
79.18000	0.10795	0.62354	-0.04409	0.42704
85.66000	0.08544	0.69249	-0.07248	0.46963
91.95000	0.00891	0.67649	-0.10151	0.43178
100.00000	-0.12241	0.57180	-0.13272	0.29603
110.00000	-0.27810	0.33298	-0.14543	0.02698
120.00000	-0.33636	0.04495	-0.10938	-0.23728
130.00000	-0.26132	-0.13261	-0.04358	-0.32232
140.00000	-0.14524	-0.15205	0.00477	-0.23818
150.00000	-0.06367	-0.10108	0.02303	-0.11422
156.00000	-0.03499	-0.06687	0.02410	-0.05170

See Appendix E.

Table XVIII

Tensor Polarization Parameters at E_d = 6.476 MeV

Center of Mass Angle (degrees)	i ⟨T11⟩	⟨T22⟩	⟨T21⟩	⟨T20⟩
17.97000	-0.18068	-0.02227	-0.01002	0.05515
22.44000	-0.24960	-0.04087	-0.00818	0.03230
29.85000	-0.33008	-0.07852	-0.00010	-0.01799
37.20000	-0.39292	-0.12441	0.01097	-0.06961
44.48000	-0.43466	-0.17138	0.02369	-0.11712
51.67000	-0.40892	-0.18537	0.03305	-0.13631
58.75000	-0.23670	-0.08908	0.02333	-0.07114
65.70000	0.04822	0.14187	-0.01901	0.09101
72.52000	0.23586	0.35870	-0.07227	0.23353
79.18000	0.25838	0.46220	-0.11182	0.28329
85.66000	0.19061	0.48338	-0.13833	0.26492
91.95000	0.08701	0.46174	-0.15847	0.20716
98.02000	-0.03165	0.41362	-0.17540	0.12146
100.00000	-0.07317	0.39235	-0.18038	0.08720
103.88000	-0.15706	0.34205	-0.18880	0.01112
110.00000	-0.28800	0.23853	-0.19546	-0.12899
120.00000	-0.42983	0.03146	-0.17254	-0.34820
130.00000	-0.38933	-0.10782	-0.10857	-0.40725
140.00000	-0.24944	-0.11931	-0.04994	-0.31040
150.00000	-0.13427	-0.07629	-0.01846	-0.19170
156.00000	-0.08833	-0.04953	-0.00917	-0.13675

See Appendix E.

Table XIX

Tensor Polarization Parameters at E_d = 6.965 MeV

Center of Mass Angle (degrees)	i ⟨T11⟩	⟨T22⟩	⟨T21⟩	⟨T20⟩
17.97000	-0.15513	-0.01439	0.01118	-0.03822
22.44000	-0.20204	-0.02473	0.02244	-0.06605
29.85000	-0.25120	-0.04483	0.04245	-0.09829
37.20000	-0.28652	-0.06912	0.06289	-0.11877
44.48000	-0.30017	-0.09326	0.08028	-0.12556
51.67000	-0.24038	-0.09421	0.07797	-0.09769
58.75000	-0.02711	-0.01895	0.01970	-0.00439
65.70000	0.25400	0.13003	-0.08869	0.10957
72.52000	0.37399	0.23680	-0.16566	0.14540
79.18000	0.34511	0.26974	-0.19350	0.11390
85.66000	0.26249	0.26541	-0.20028	0.05634
91.95000	0.16387	0.24568	-0.20248	-0.01348
98.02000	0.05519	0.21651	-0.20534	-0.09561
100.00000	0.01612	0.20460	-0.20857	-0.12638
103.88000	-0.06663	0.17704	-0.20909	-0.19324
109.50000	-0.20087	0.12524	-0.21099	-0.30473
110.00000	-0.21344	0.11990	-0.21091	-0.31527
120.00000	-0.44519	-0.00358	-0.19020	-0.50707
130.00000	-0.49536	-0.09156	-0.12662	-0.52947
140.00000	-0.36114	-0.08965	-0.06380	-0.38943
150.00000	-0.21692	-0.05350	-0.02923	-0.25241
156.00000	-0.15246	-0.03375	-0.01819	-0.19582

See Appendix E.

Table XX

Tensor Polarization Parameters at E_d = 7.479 MeV

Center of Mass Angle (degrees)	i ⟨T11⟩	⟨T22⟩	⟨T21⟩	⟨T20⟩
17.97000	-0.11630	-0.00731	0.02693	-0.11229
22.44000	-0.13951	-0.01139	0.04161	-0.13234
29.85000	-0.15565	-0.01840	0.06367	-0.13933
37.20000	-0.16123	-0.02607	0.08322	-0.13007
44.48000	-0.14616	-0.03199	0.09322	-0.10087
51.67000	-0.06214	-0.02484	0.06425	-0.03309
58.75000	0.15453	0.01802	-0.05489	0.06989
65.70000	0.37921	0.08044	-0.20972	0.10855
72.52000	0.42806	0.10823	-0.27139	0.04776
79.18000	0.37750	0.10668	-0.26701	-0.03605
85.66000	0.30778	0.09542	-0.24809	-0.11440
91.95000	0.23605	0.08115	-0.23140	-0.19126
98.02000	0.15806	0.06446	-0.21963	-0.27486
103.88000	0.06375	0.04403	-0.21145	-0.37214
109.50000	-0.05610	0.01847	-0.20380	-0.48423
120.00000	-0.35986	-0.04363	-0.17184	-0.69555
130.00000	-0.55267	-0.07999	-0.10414	-0.69606
140.00000	-0.47348	-0.06308	-0.04418	-0.48944
150.00000	-0.31118	-0.03363	-0.01689	-0.31094
156.00000	-0.22763	-0.02030	-0.00968	-0.24384

See Appendix E.

Table XXI

Tensor Polarization Parameters at E_d = 7.968 MeV

Center of Mass Angle (degrees)	i ⟨T11⟩	⟨T22⟩	⟨T21⟩	⟨T20⟩
17.97000	-0.07894	-0.00271	0.03597	-0.15485
22.44000	-0.08390	-0.00335	0.04993	-0.16039
29.85000	-0.07559	-0.00355	0.06749	-0.14135
37.20000	-0.05963	-0.00281	0.07892	-0.10702
44.48000	-0.02636	-0.00027	0.07310	-0.05039
51.67000	0.06154	0.00609	0.01134	0.04255
58.75000	0.24484	0.01610	-0.15838	0.13345
65.70000	0.40630	0.01913	-0.32879	0.09401
72.52000	0.42417	0.01206	-0.35738	-0.03512
79.18000	0.38276	0.00308	-0.31945	-0.14671
85.66000	0.33822	-0.00534	-0.27790	-0.23363
90.00000	0.30967	-0.01108	-0.25468	-0.28802
91.95000	0.29658	-0.01379	-0.24557	-0.31298
98.02000	0.25039	-0.02321	-0.22159	-0.39773
100.00000	0.23200	-0.02671	-0.21488	-0.42891
103.88000	0.18787	-0.03437	-0.20261	-0.49681
109.50000	0.09535	-0.04750	-0.18488	-0.61303
110.00000	0.08496	-0.04878	-0.18318	-0.62433
120.00000	-0.21182	-0.07391	-0.13664	-0.84675
130.00000	-0.53348	-0.07531	-0.06381	-0.85893
140.00000	-0.55364	-0.04646	-0.01233	-0.60217
150.00000	-0.39586	-0.02119	0.00255	-0.37697
156.00000	-0.29803	-0.01199	0.00388	-0.29487

See Appendix E.

Table XXII

Tensor Polarization Parameters at E_d = 8.481 MeV

Center of Mass Angle (degrees)	i ⟨T11⟩	⟨T22⟩	⟨T21⟩	⟨T20⟩
17.97000	-0.04245	0.00026	0.04073	-0.17524
22.44000	-0.03305	0.00110	0.05121	-0.16083
29.85000	-0.00723	0.00302	0.05986	-0.11391
37.20000	0.02245	0.00513	0.05824	-0.05694
44.48000	0.06339	0.00591	0.03112	0.02060
51.67000	0.13909	-0.00046	-0.06600	0.12534
58.75000	0.27151	-0.02560	-0.27635	0.18700
65.70000	0.38049	-0.05925	-0.44504	0.06856
72.52000	0.39574	-0.07334	-0.43272	-0.11549
79.18000	0.37915	-0.07475	-0.35990	-0.24359
85.66000	0.36474	-0.07433	-0.29625	-0.33206
91.95000	0.35337	-0.07534	-0.24916	-0.40930
98.02000	0.33764	-0.07834	-0.21380	-0.49162
100.00000	0.32964	-0.07978	-0.20361	-0.52210
103.88000	0.30664	-0.08321	-0.18460	-0.58892
110.00000	0.23813	-0.08986	-0.15433	-0.71646
120.00000	-0.02545	-0.09746	-0.09092	-0.95513
130.00000	-0.43797	-0.07981	-0.01096	-1.00832
140.00000	-0.59752	-0.04114	0.03086	-0.73406
150.00000	-0.47498	-0.01567	0.02957	-0.45962
156.00000	-0.36882	-0.00806	0.02293	-0.35717

See Appendix E.

Table XXIII

Tensor Polarization Parameters at E_d = 8.971 MeV

Center of Mass Angle (degrees)	i ⟨T11⟩	⟨T22⟩	⟨T21⟩	⟨T20⟩
17.97000	-0.01638	0.00153	0.03924	-0.16557
22.44000	0.00135	0.00250	0.04361	-0.12894
29.85000	0.03547	0.00375	0.03986	-0.05726
37.20000	0.06969	0.00365	0.02224	0.01566
44.48000	0.10911	-0.00113	-0.02708	0.10249
51.67000	0.16741	-0.02029	-0.15102	0.19913
58.75000	0.25915	-0.06688	-0.37333	0.21363
65.70000	0.34445	-0.11444	-0.51730	0.02645
72.52000	0.37719	-0.12395	-0.46515	-0.19345
79.18000	0.38829	-0.11555	-0.36322	-0.32516
85.66000	0.39915	-0.10721	-0.28218	-0.40625
90.00000	0.40727	-0.10362	-0.24032	-0.45293
91.95000	0.41070	-0.10257	-0.22407	-0.47418
98.02000	0.41739	-0.10141	-0.18062	-0.54744
103.88000	0.41012	-0.10293	-0.14467	-0.63615
103.88000	0.41012	-0.10293	-0.14467	-0.63615
109.50000	0.37533	-0.10607	-0.11115	-0.74475
110.00000	0.37019	-0.10639	-0.10807	-0.75563
114.87000	0.29536	-0.10914	-0.07635	-0.87036
120.00000	0.15417	-0.10950	-0.03852	-0.99667
130.00000	-0.28853	-0.08938	0.03660	-1.10740
140.00000	-0.58113	-0.04661	0.06451	-0.87155
150.00000	-0.52340	-0.01722	0.04845	-0.57016
156.00000	-0.42034	-0.00859	0.03539	-0.44990

See Appendix E.

Figure 1. Energy level diagram for Li^6 with the level assignments of Ajzenberg-Selove and Lauritsen (1959). For the revised level assignments, see Tables VII through IX. Also see text, pp. 1ff.

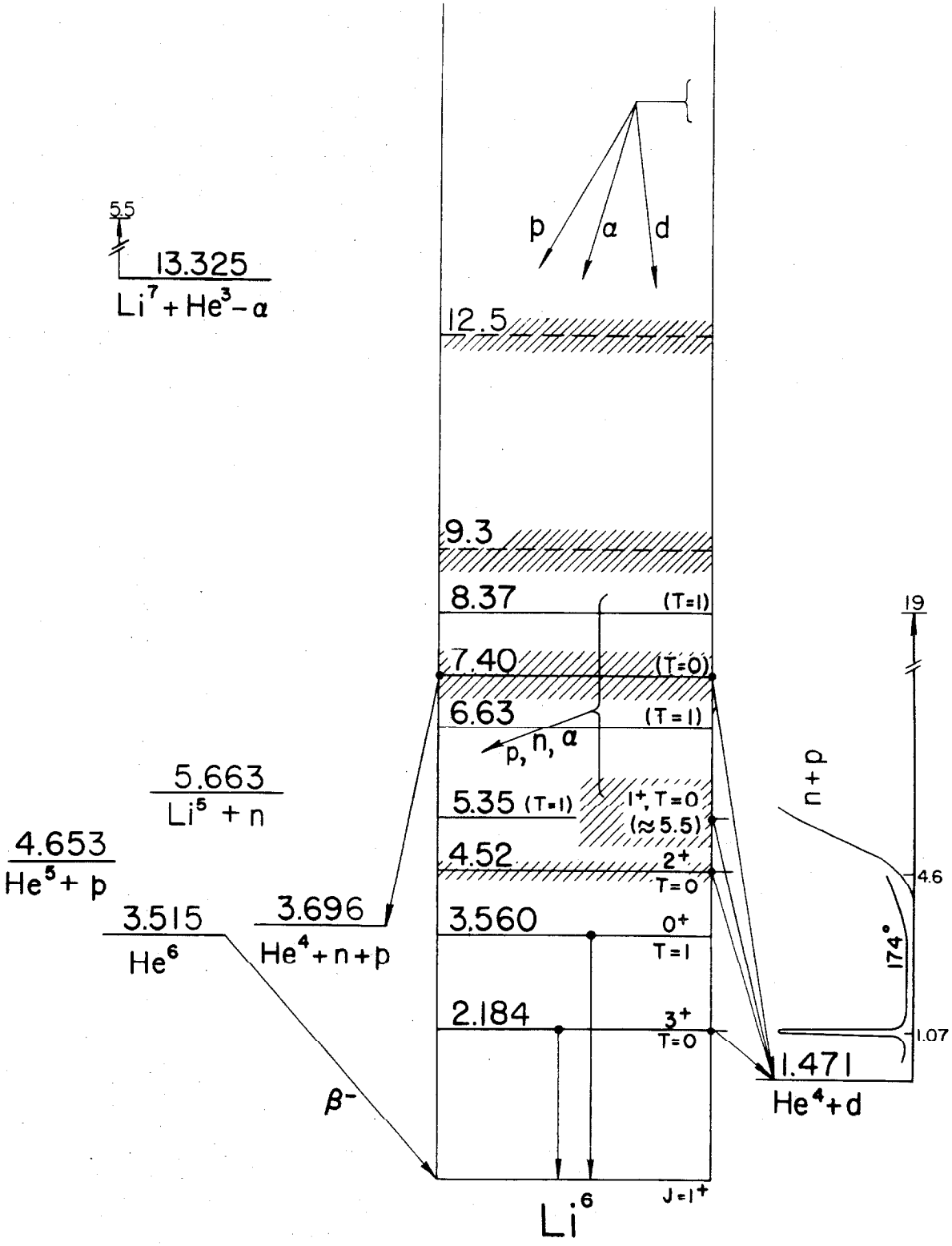
5.5
13.325
Li⁷ + He³ − α
p
α
d
12.5
9.3
8.37
(T=1)
7.40
(T=0)
6.63
(T=1)
p, n, α
5.663
Li⁵ + n
5.35 (T=1)
1⁺, T=0
(≈5.5)
4.653
He⁵ + p
4.52
2⁺
T=0
3.515
He⁶
3.696
He⁴ + n + p
3.560
0⁺
T=1
2.184
3⁺
T=0
β⁻
Li⁶
J=1⁺
19
n + p
4.6
174°
1.07
1.471
He⁴ + d

Figure 2. Cross-section of the gas scattering chamber. See text, pp. 5ff.

1. Modified ½" "Circle Seal" plug shutoff valve.
2. Entrance Foil
3. Beam Collimator
4. Beam defining apertures
5. Standard 1" pipe coupling
6. "Pic Design Corporation" disc dial vernier
7. "Pic Design Corporation" disc dial (protractor)
8. Adjustable platform
9. Defining slits for the stationary counter
10. Defining slits for the moving counter
11. Thermometer
12. Exit foil
13. Magnetic suppressor
14. Electrostatic suppressor
15. Insulator
16. Insulating mount for Faraday cup
17. Faraday cup
18. Rotating hub
19. Lucite top

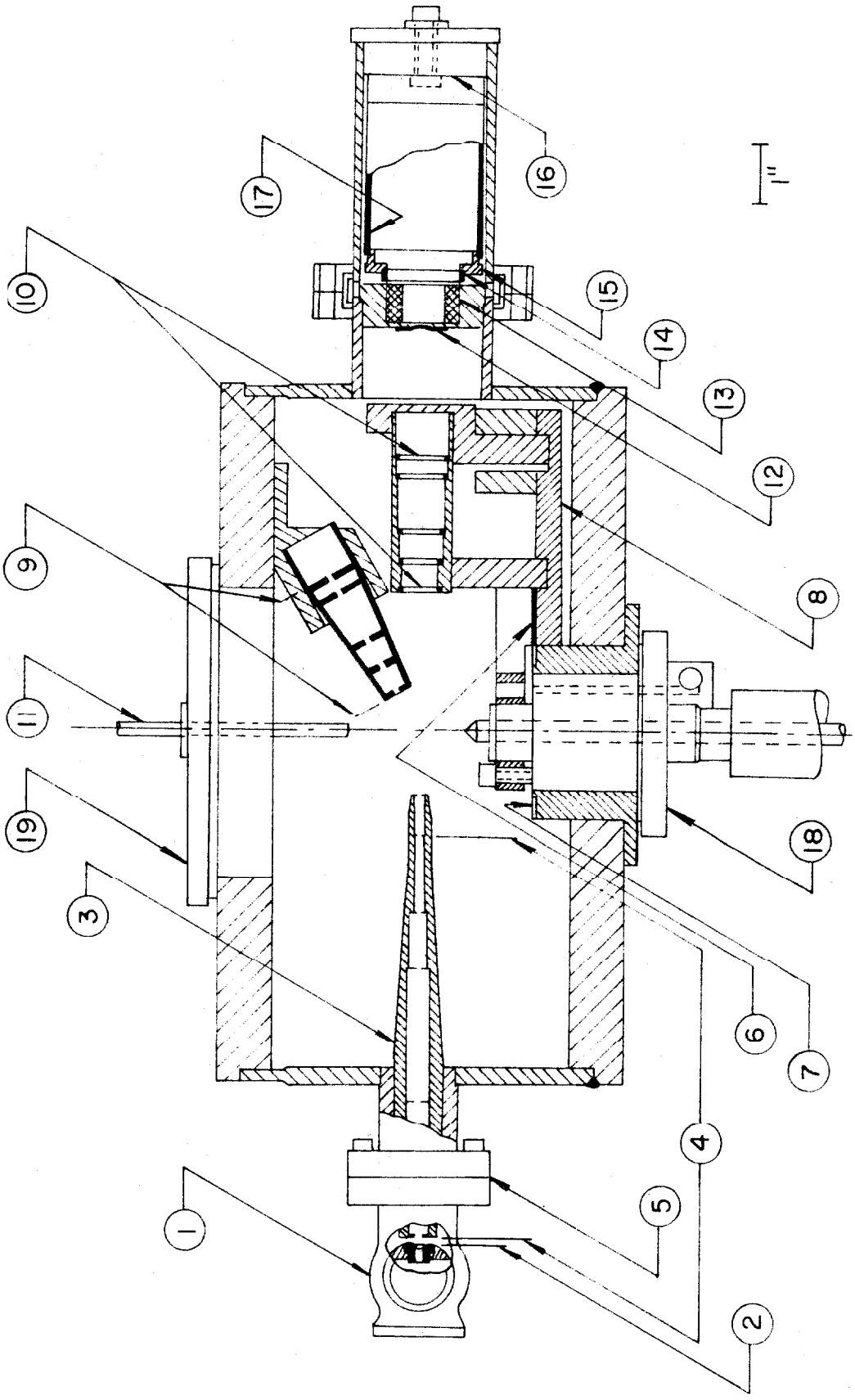
1"
1
2
3
4
5
6
7
8
9
10
11
12
13
14
15
16
17
18
19

Figure 3. Scattered particle counts vs. suppressor voltage for $He^4(d,d)He^4$ at 5.6 MeV. The collection is relatively independent of suppressor voltage with a negative bias in excess of 80 volts. See text, p. 14.

Voltage		Monitor
Cup (positive)	Suppressor (negative)	Counts (x 1000)
70	30	26.455
	40	23.753
	50	21.843
	60	21.253
	78	20.583
	150	20.464
	150	20.205
	150	20.555
0	150	20.355
	150	20.167
	230	20.080
70	230	20.346

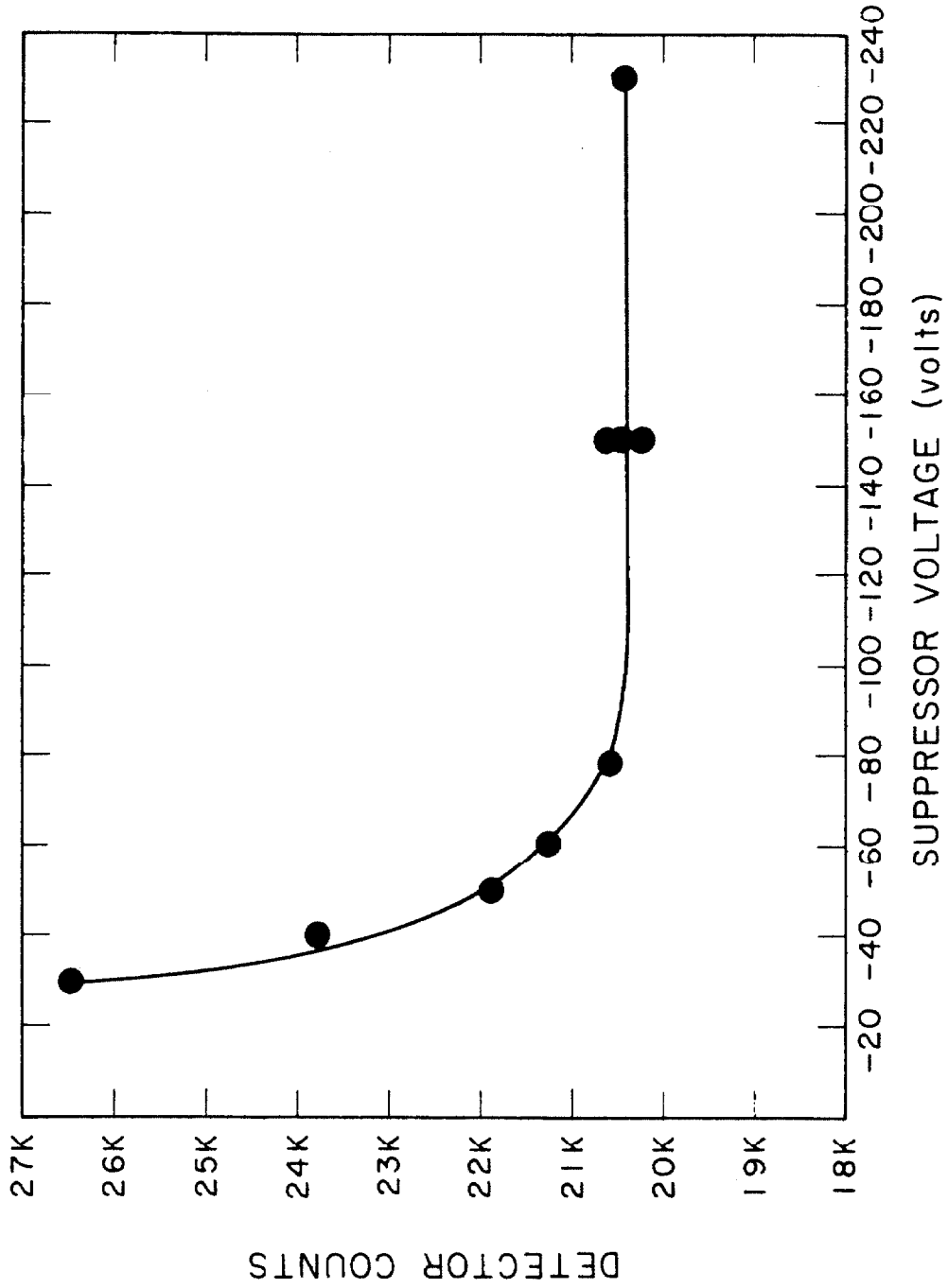
DETECTOR COUNTS
27K
26K
25K
24K
23K
22K
21K
20K
19K
18K
SUPPRESSOR VOLTAGE (volts)
-20 -40 -60 -80 -100 -120 -140 -160 -180 -200 -220 -240

Figure 4. Scattered particle counts vs. pressure from $He^4(\alpha,\alpha)He^4$ at 4.00 MeV and $\theta_{lab} = 12°$.

See text, p. 15.

Pressure (cm.-oil)	Corrected Counts (x 1000)
5.881	102.9
10.135	178.3
15.495	257.4
23.740	434.0

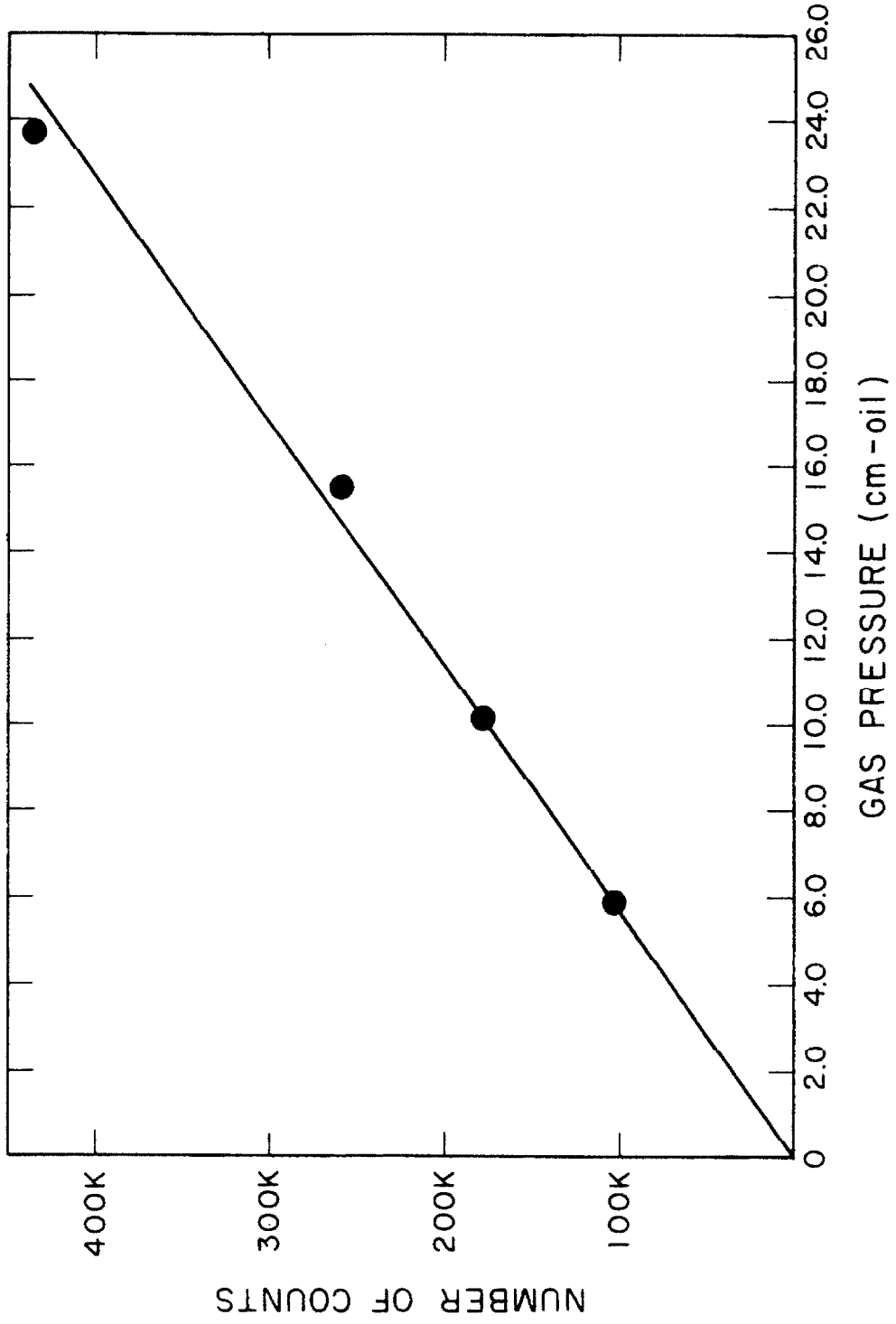
NUMBER OF COUNTS
400K
300K
200K
100K
0
2.0
4.0
6.0
8.0
10.0
12.0
14.0
16.0
18.0
20.0
22.0
24.0
26.0
GAS PRESSURE (cm-oil)

Figure 5. Scattered particle counts vs. pressure from $He^4(d,d)He^4$ at 3.00 MeV and $\theta_{lab} = 12°$.

See text, p. 15.

Pressure (cm.-oil)	Corrected Counts (x 1000)
5.285	145.4
14.095	419.0
19.365	563.0
25.350	740.0

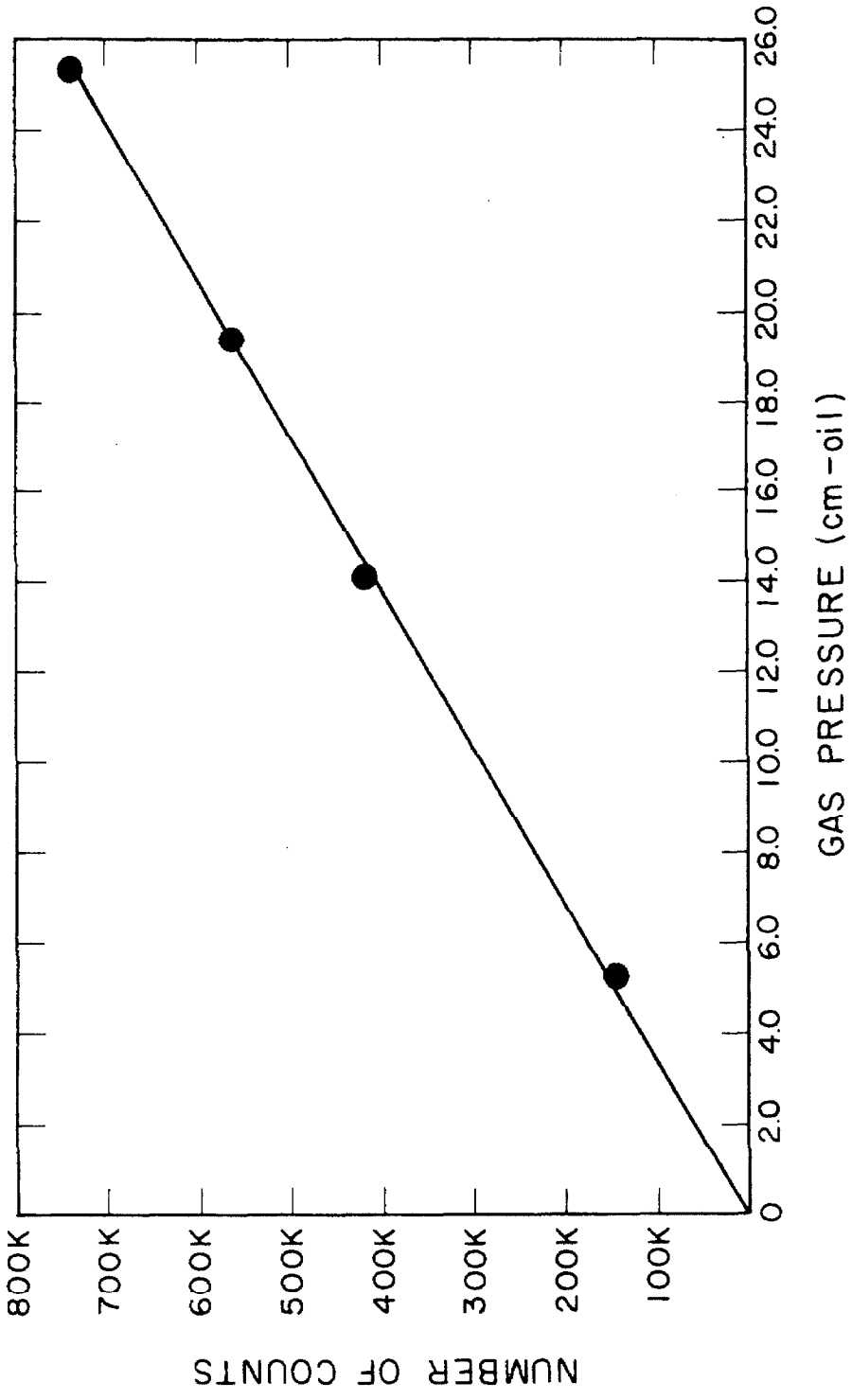
NUMBER OF COUNTS
800K
700K
600K
500K
400K
300K
200K
100K
0
2.0
4.0
6.0
8.0
10.0
12.0
14.0
16.0
18.0
20.0
22.0
24.0
26.0
GAS PRESSURE (cm-oil)

Figure 6. Schematic of the experimental layout. The stationary counter is not shown.

See text, p. 17.

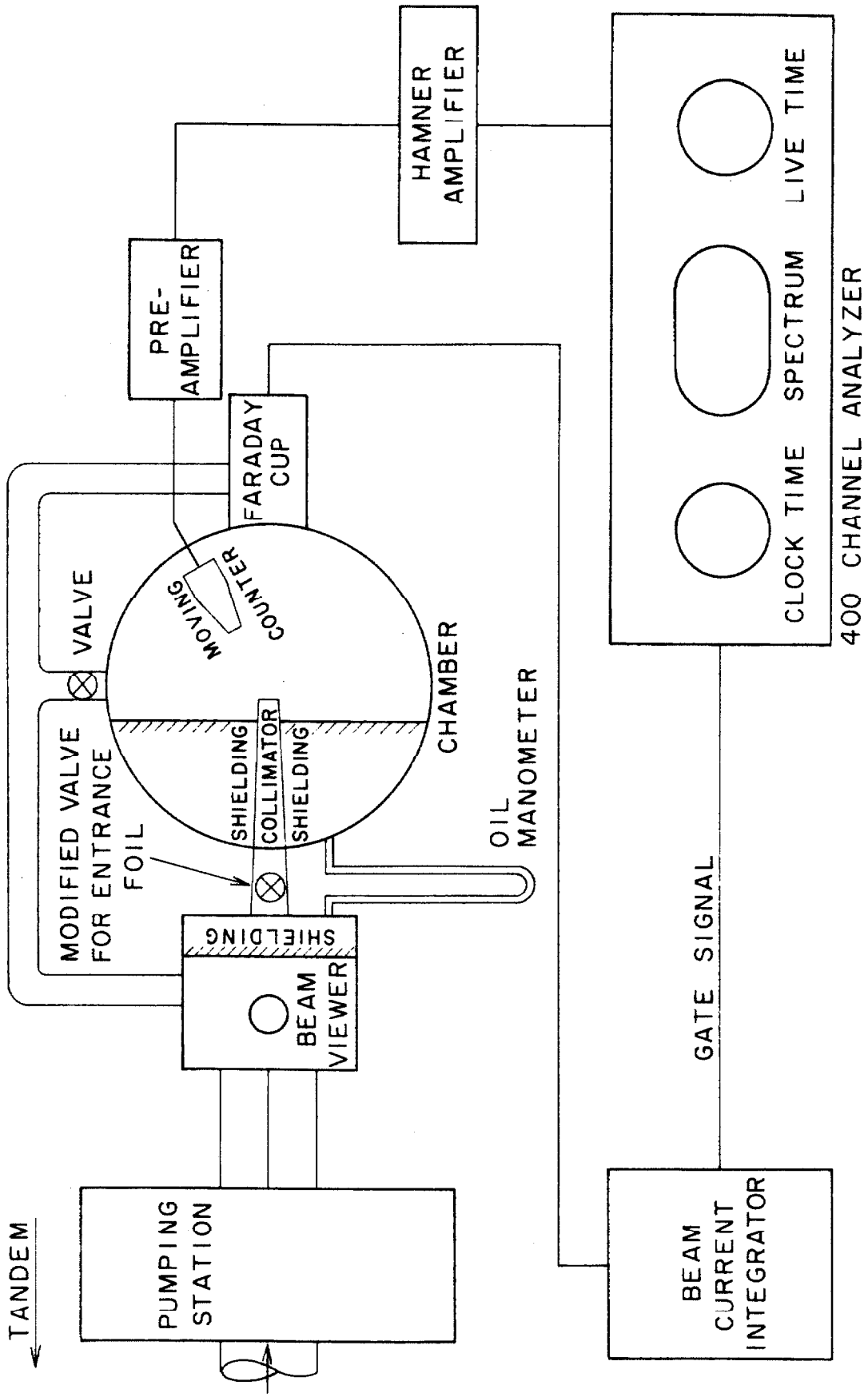
TANDEM
PUMPING STATION
BEAM VIEWER
SHIELDING
MODIFIED VALVE FOR ENTRANCE FOIL
VALVE
SHIELDING
COLLIMATOR
SHIELDING
MOVING COUNTER
CHAMBER
FARADAY CUP
PRE-AMPLIFIER
HAMNER AMPLIFIER
OIL MANOMETER
GATE SIGNAL
BEAM CURRENT INTEGRATOR
CLOCK TIME
SPECTRUM
LIVE TIME
400 CHANNEL ANALYZER

Figure 7. Bias supply to moving counter from the Tennelec model #100 preamplifier. A negative bias was supplied at point C and proved insufficient for the low resistivity lithium diffused counter with the standard 22 MΩ resistor in the preamplifier, so the resistor was replaced with a 2.2 MΩ resistor. The moving counter with a much higher resistivity was biased through an unmodified preamplifier. See text, p. 17.

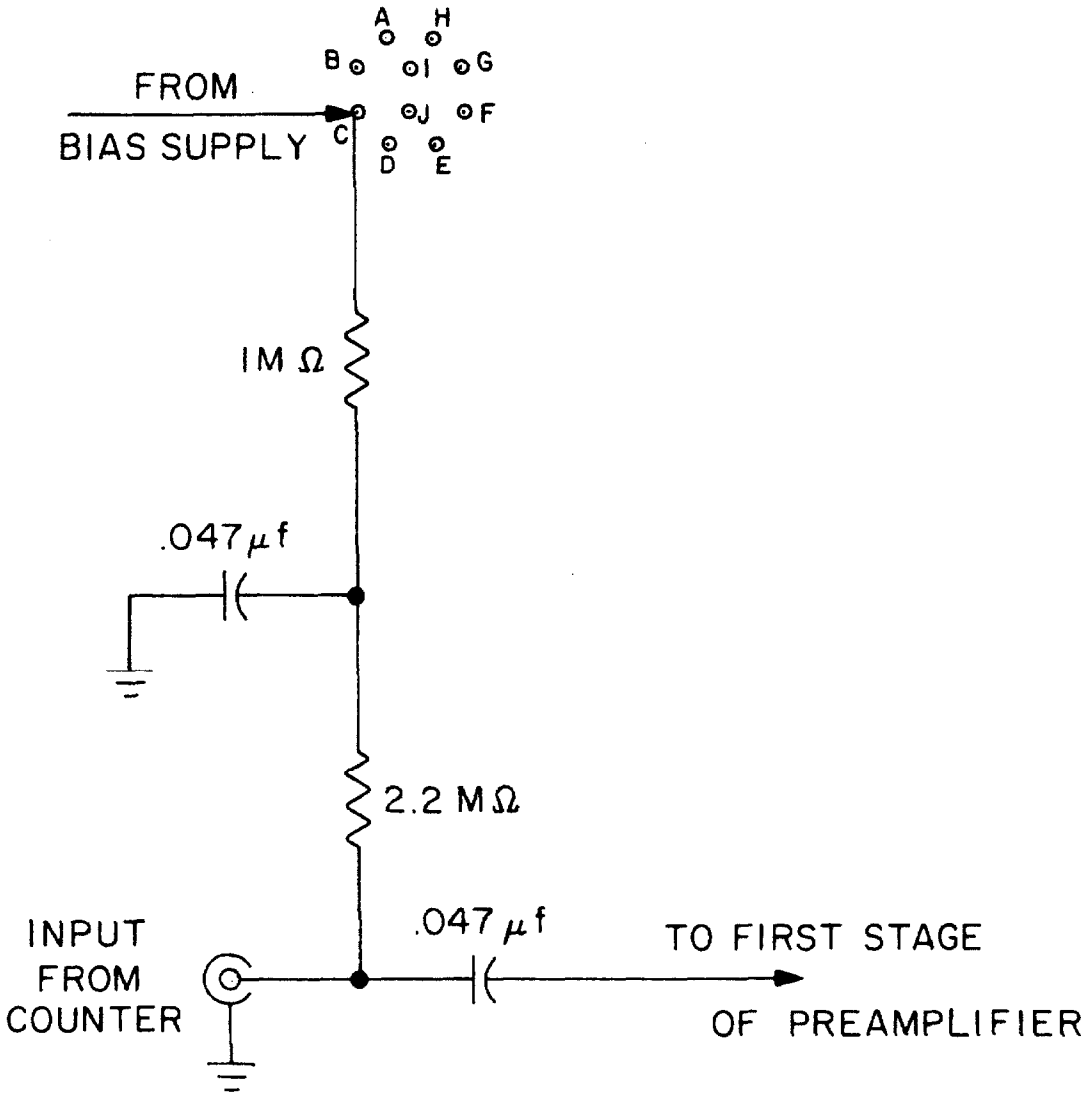
A
H
B
I
G
FROM
BIAS SUPPLY
C
J
F
D
E
IM Ω
.047 μf
2.2 MΩ
INPUT
FROM
COUNTER
.047 μf
TO FIRST STAGE
OF PREAMPLIFIER

Figure 8. Integrator test current circuit. The current was supplied by a standard test cell and was varied with a 10 turn 100 K heliopot. The current was measured by the voltage drop across the .99850 MΩ resistor, with a Rubicon galvanometer. The 100.85 MΩ resistor was used in other test current ranges. See text, p. 17.

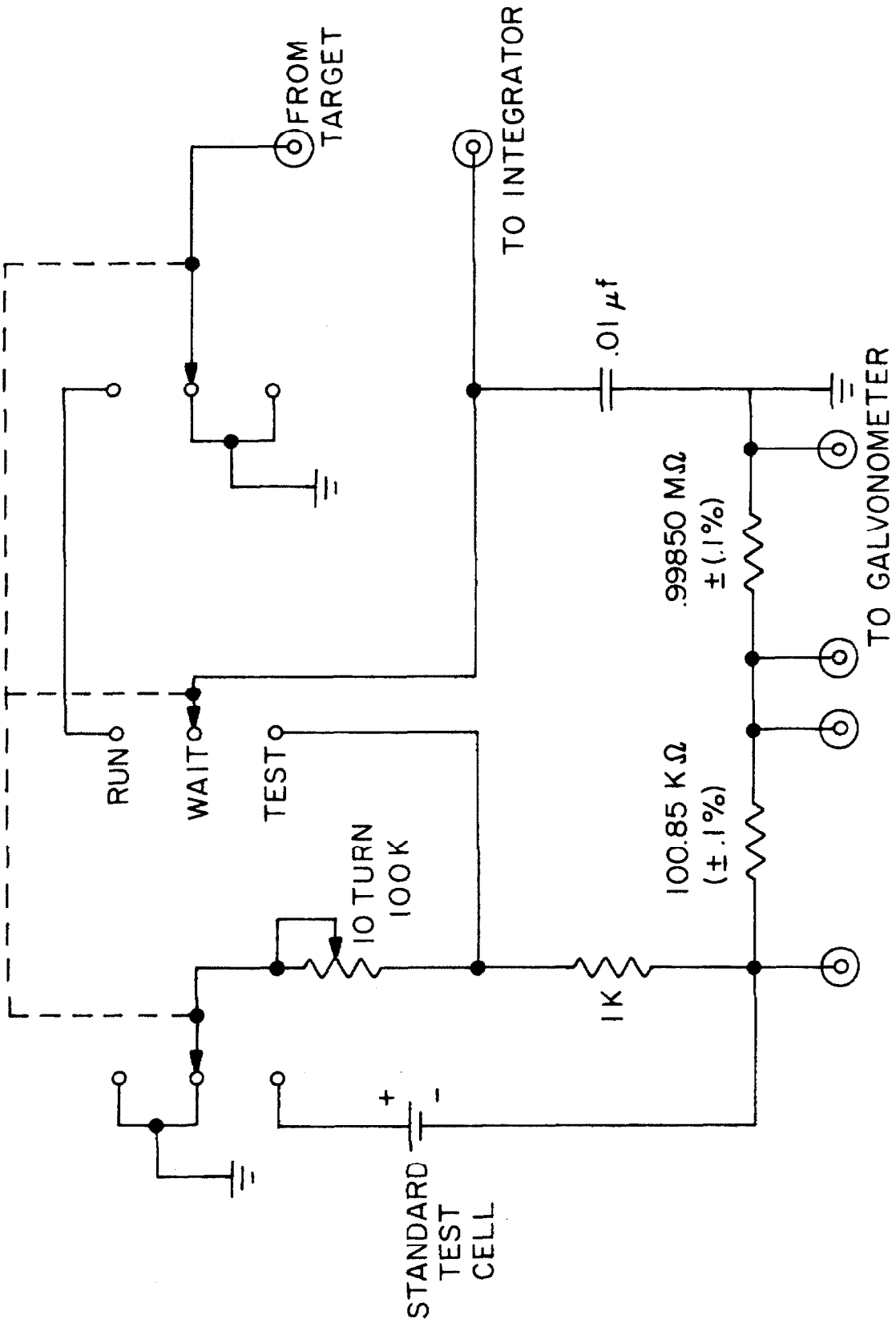
FROM TARGET
TO INTEGRATOR
.01 μf
TO GALVONOMETER
.99850 MΩ ±(.1%)
100.85 KΩ (±.1%)
1K
10 TURN 100K
RUN
WAIT
TEST
+
-
STANDARD TEST CELL

Figure 9A. Kinematics for $He^4(d,d)He^4$, where E_s/E_o is the curve that gives the relative energy of the scattered particle in the laboratory system and E_r/E_o is that for the recoil particle in the laboratory system. See text, pp. 23ff.

Figure 9B. Kinematics for $H^2(\alpha,\alpha)H^2$, where E_s/E_o is the curve that gives the relative energy of the scattered particle in the laboratory system and E_r/E_o is that for the recoil particle in the laboratory system. Only the recoil particles were used for cross-section calculations, in that the scattered particles are either too close to the recoil particles at angles such as 19° or the spread in energy seen by the counter is too great at angles such as 30°.
See text, pp. 23ff.

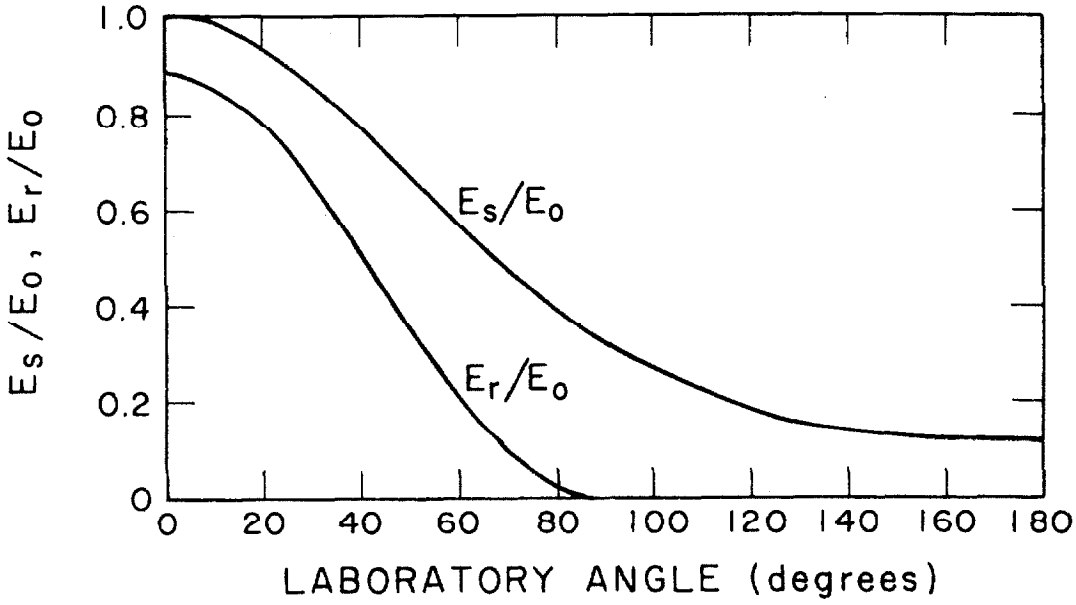
1.0
0.8
0.6
0.4
0.2
0
E_s/E_o, E_r/E_o
E_s/E_o
E_r/E_o
0 20 40 60 80 100 120 140 160 180
LABORATORY ANGLE (degrees)

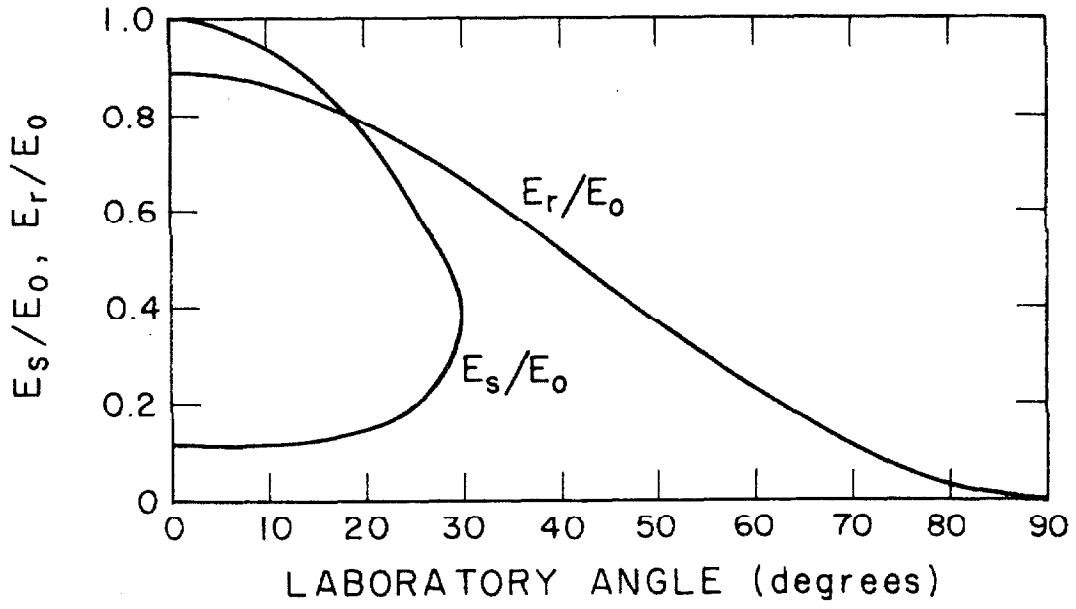
1.0
0.8
0.6
0.4
0.2
0
E_s/E_o, E_r/E_o
E_r/E_o
E_s/E_o
0 10 20 30 40 50 60 70 80 90
LABORATORY ANGLE (degrees)

Figure 10. Parameterization of the counter collimator geometry. The detection area is in the xy plane and is being illuminated from an element dB of the beam in the xz plane, a beam distance of B from the z axis. The illuminated area dS makes an angle χ with the scattered ray which in turn makes an angle θ with the incident beam which is at an angle θ_o with the z axis. The remaining parameters on the figure are self-explanatory and are treated further in the text, pp. 47ff.

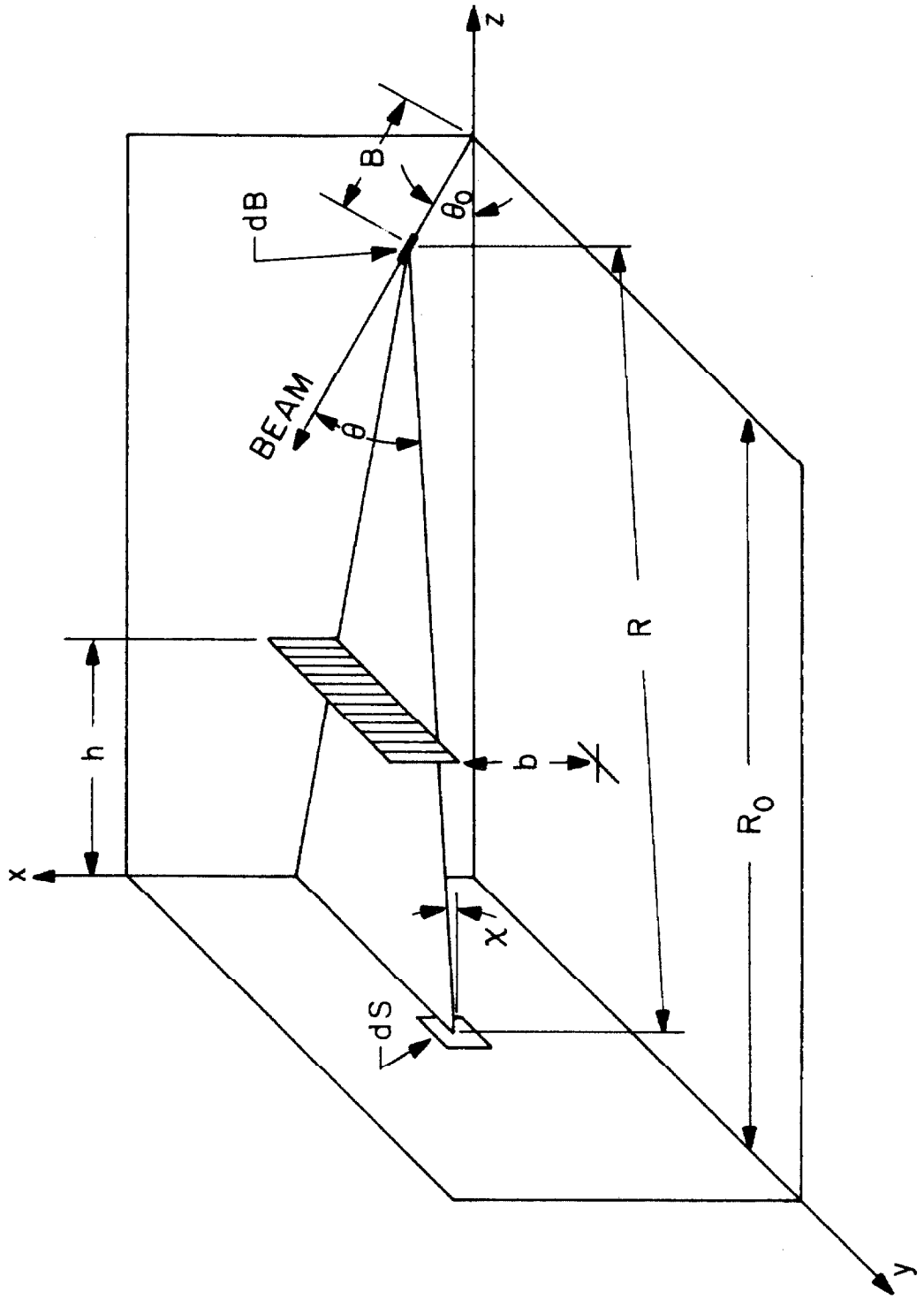
z
B
dB
θ0
BEAM
θ
R
h
b
R0
x
χ
dS
y

Figure 11. Typical spectrum from d-He^4 elastic scattering, using a lithium drifted detector. The alpha and the deuteron peaks are labeled, where

M is the number of residual counts in the alpha spectrum after background is subtracted

N is the number of background counts in the alpha spectrum

M' is the number of residual counts in the deuteron spectrum after background is subtracted

N' is the number of background counts in the deuteron spectrum

See text, p. 19.

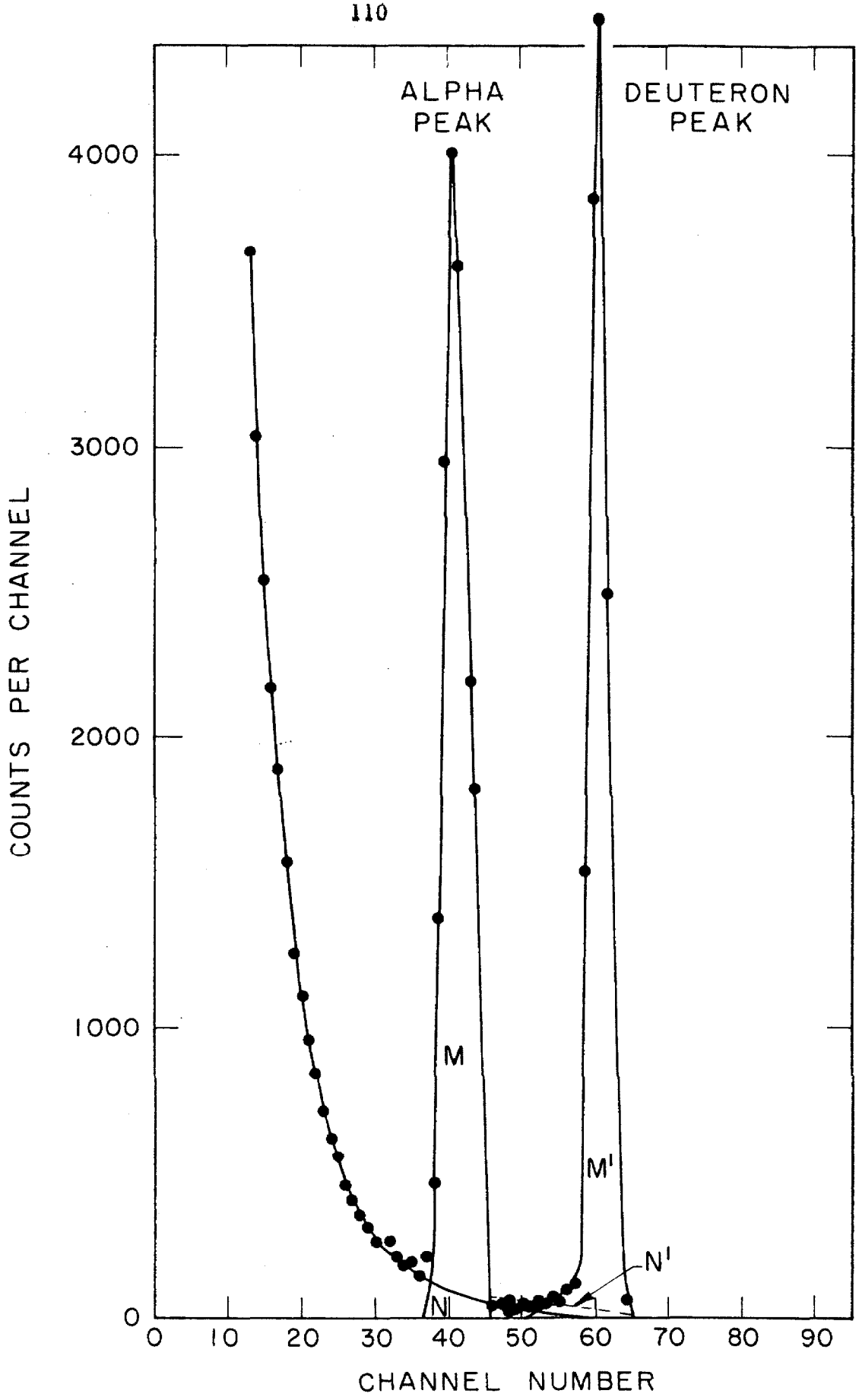
ALPHA PEAK
DEUTERON PEAK
4000
3000
2000
1000
0
COUNTS PER CHANNEL
M
M'
N
N'
0
10
20
30
40
50
60
70
80
90
CHANNEL NUMBER

Figure 12. Simplified block diagram of phase shift analysis program. A thumbnail description of the program is as follows. After choosing a case out of the nine available, the values that do not vary during the iteration are calculated starting at point 1. Then cross-sections are calculated for the various angles and a $\chi^2 = \left\{ (\sigma_e(N) - \sigma_e(N))/ \sigma_e(N) \right\}^2$ is calculated from the cross-sections. Next, slopes are calculated from which we can obtain changes in parameters according to Equation 13, and from these an rms value is calculated. The course the program then takes depends mainly on the rms value and secondarily on the value of χ^2. The rms value is compared with the previous rms value, which has been saved or is set equal to 100 radians, for the first iteration. If the rms value is larger than the previous value, the program will scan intermediate values between this set of parameters, $(\delta, \Delta\delta)$, and those of the previous iteration, $(\delta', \Delta\delta')$, and will continue on, when the rms value is less than the previous one. The choice of 100 radians insures that the program will get past this point the first time. If the rms value meets this requirement and is less than 0.1°, the program will print its calculated values after determining polarization parameters and total reaction cross-section. If $0.1° < \text{rms} \leq 3°$, the program will modify γ and compare χ^2 with the previous value after setting a control index KKW = 2. If χ^2 is larger than the previous value, another scanning is used until this requirement is met. If $3° < \text{rms} \leq 20°$, χ^2 is not checked. And in the event rms is greater than 20°, $\pm$ 3° is added in the appropriate direction to those parameters whose changes are greater than $\pm$ 10°.
See text, p. 34 and Appendix G.

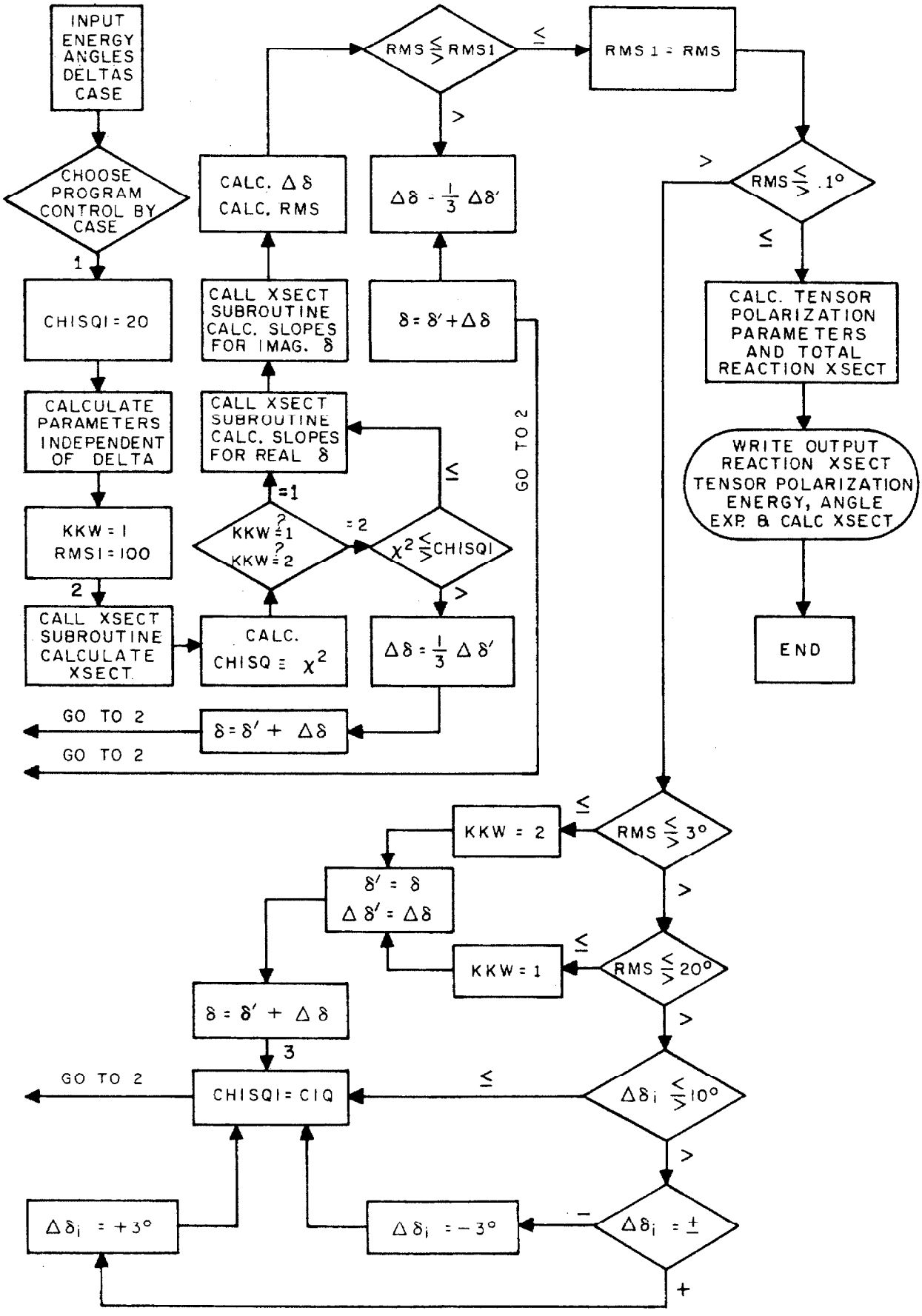
INPUT ENERGY ANGLES DELTAS CASE
CHOOSE PROGRAM CONTROL BY CASE
1
CHISQI = 20
CALCULATE PARAMETERS INDEPENDENT OF DELTA
KKW = 1
RMSI = 100
2
CALL XSECT SUBROUTINE CALCULATE XSECT
CALC. CHISQ ≡ χ²
KKW = 1 ? KKW = 2 ?
=1
=2
CALL XSECT SUBROUTINE CALC. SLOPES FOR REAL δ
CALL XSECT SUBROUTINE CALC. SLOPES FOR IMAG. δ
CALC. Δδ CALC. RMS
RMS ≶ RMS1
≤
>
RMS 1 = RMS
Δδ = 1/3 Δδ'
δ = δ' + Δδ
δ = δ' + Δδ
GO TO 2
GO TO 2
Δδ = 1/3 Δδ'
χ² ≶ CHISQI
≤
>
RMS ≶ .1°
≤
>
CALC. TENSOR POLARIZATION PARAMETERS AND TOTAL REACTION XSECT
WRITE OUTPUT REACTION XSECT TENSOR POLARIZATION ENERGY, ANGLE EXP. & CALC XSECT
END
RMS ≶ 3°
≤
>
KKW = 2
δ' = δ
Δδ' = Δδ
RMS ≶ 20°
≤
>
KKW = 1
δ = δ' + Δδ
3
Δδi ≶ 10°
≤
>
CHISQI = CIQ
GO TO 2
Δδi = ±
−
+
Δδi = −3°
Δδi = +3°

Figure 13. Real parts of $\delta_0{}^1$ and $\delta_2{}^1$ phase shifts and ϵ, the tensor coupling parameter. See text, pp. 33ff.

E (MeV)	$\delta_0{}^1$ (degrees)	$\delta_2{}^1$ (degrees)	ϵ (degrees)
2.935	100.5	- 3.0	14.0
3.441	91.5	- 4.0	8.8
3.946	84.5	3.8	5.0
4.450	79.0	15.0	2.5
4.731	76.5	22.5	1.5
4.955	74.6	29.5	0.8
5.473	71.0	44.5	-0.7
5.961	67.5	59.5	-1.0
6.476	64.5	74.2	-2.0
6.965	62.0	87.4	-2.0
7.479	60.0	100.0	-2.0
7.968	58.7	110.0	-2.0
8.481	57.0	119.5	-2.0
8.971	55.2	126.5	-2.0

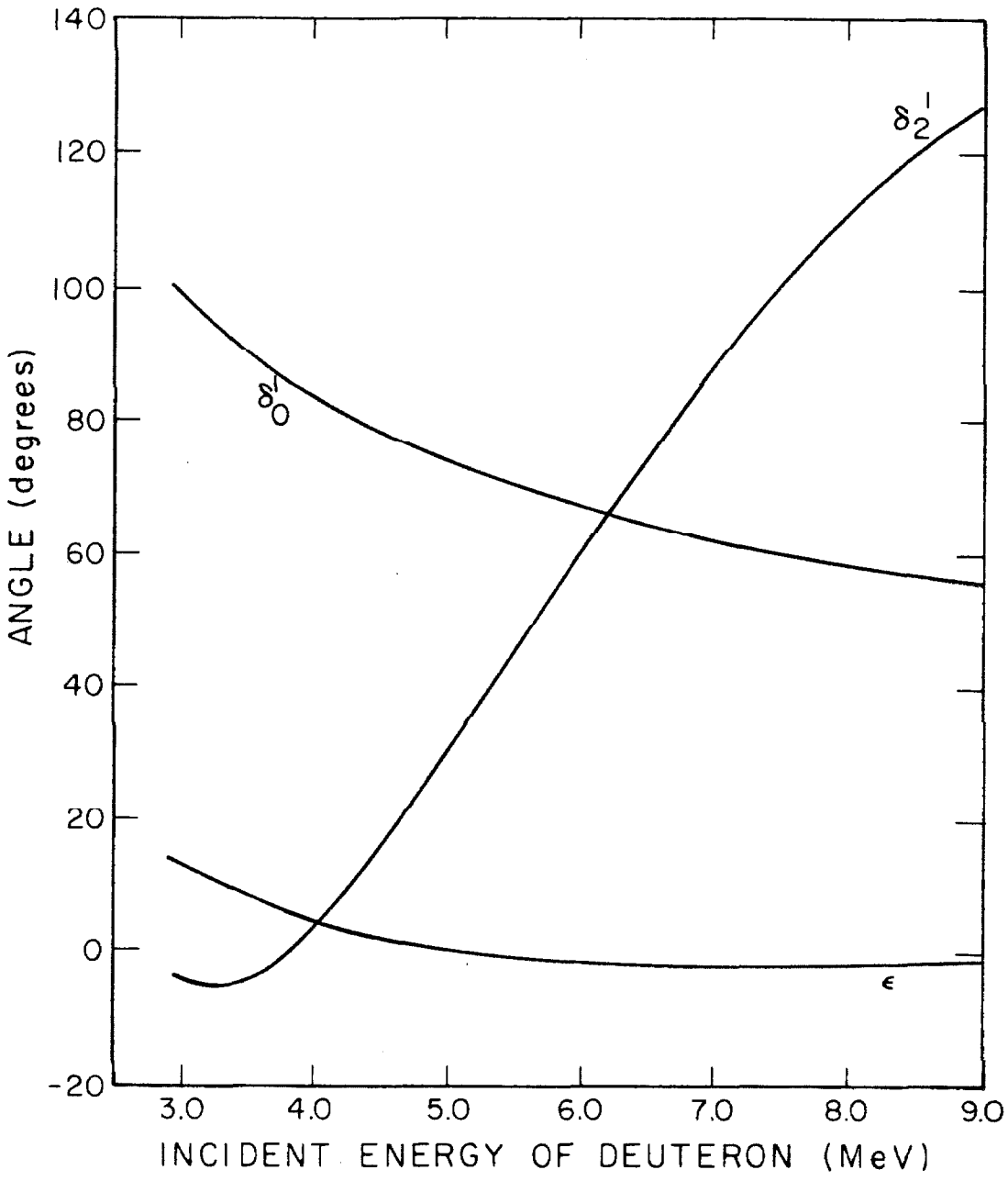
140
120
100
80
60
40
20
0
-20
ANGLE (degrees)
δ_2^1
δ_0^1
ϵ
3.0
4.0
5.0
6.0
7.0
8.0
9.0
INCIDENT ENERGY OF DEUTERON (MeV)

Figure 14. Real parts of δ_2^3, δ_2^2 and δ_2^1 phase shifts. The dashed line is that of Galonsky and McEllistrem (1955a).

See text, pp. 38ff.

E (MeV)	δ_2^3 (degrees)	δ_2^2 (degrees)	δ_2^1 (degrees)
2.935	170.0	8.0	- 3.0
3.441	170.0	20.9	- 4.0
3.946	170.0	39.5	3.8
4.450	170.0	65.0	15.0
4.731	170.0	78.5	22.5
4.955	170.0	88.0	29.5
5.473	170.0	105.2	44.5
5.961	170.0	116.5	59.5
6.476	170.0	123.6	74.2
6.965	170.0	129.1	87.4
7.479	170.0	133.5	100.0
7.968	170.0	137.0	110.0
8.481	170.0	140.2	119.5
8.971	170.0	143.0	126.5

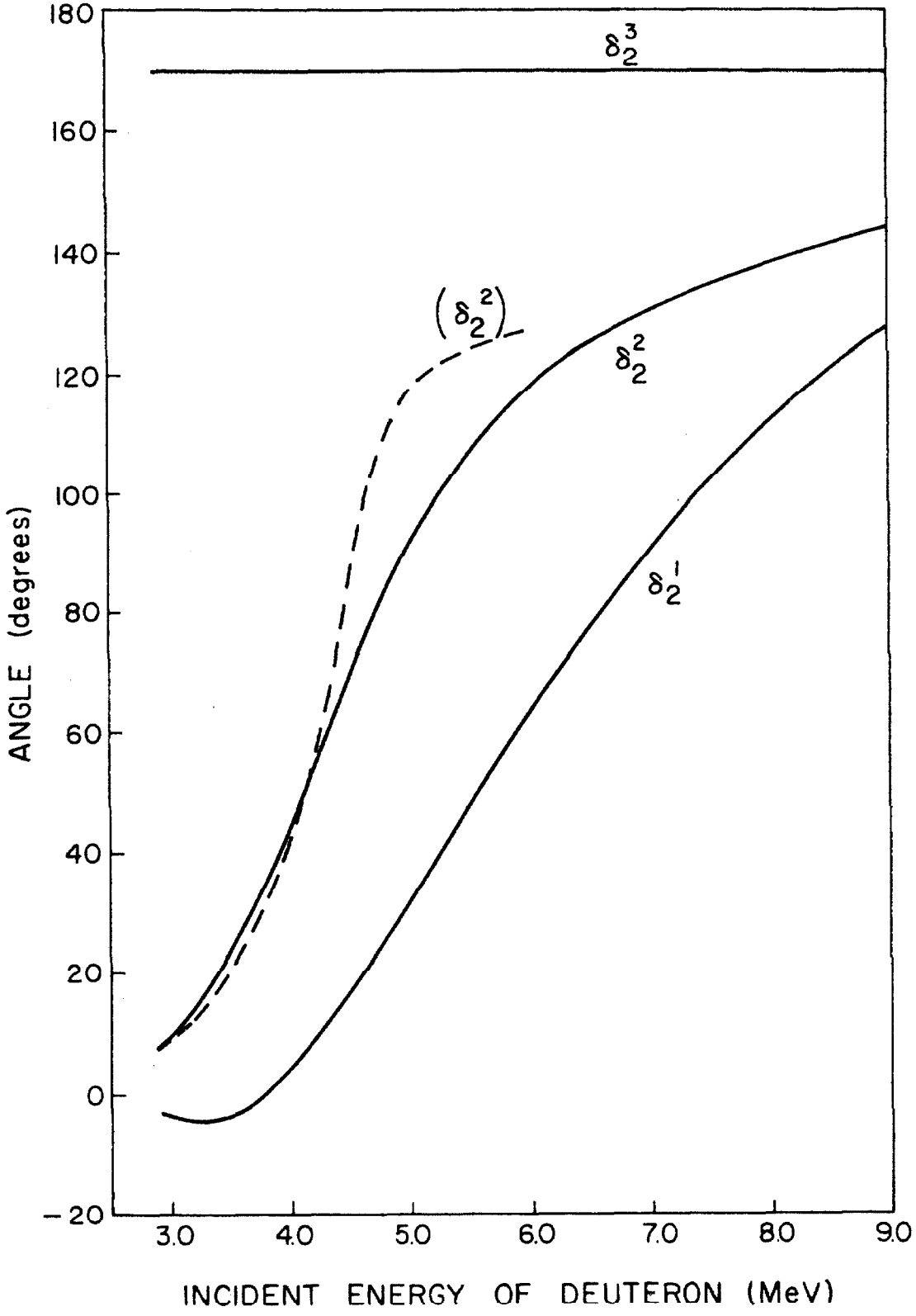
180
160
140
120
100
80
60
40
20
0
−20
ANGLE (degrees)
3.0
4.0
5.0
6.0
7.0
8.0
9.0
INCIDENT ENERGY OF DEUTERON (MeV)
δ_2^3
(δ_2^2)
δ_2^2
δ_2^1

Figure 15. Real parts of δ_1^2, δ_1^1 and δ_1^0 phase shifts.

See text, pp. 38ff.

E (MeV)	δ_1^2 (degrees)	δ_1^1 (degrees)	δ_1^0 (degrees)
2.935	- 7.0	- 7.0	- 7.0
3.441	- 9.1	-12.0	- 9.1
3.946	-11.5	-14.3	-11.5
4.450	-13.5	-10.5	-13.5
4.731	-14.0	- 7.2	-14.0
4.955	-14.8	- 4.4	-14.8
5.473	-15.8	2.4	-15.8
5.961	-16.0	8.5	-16.0
6.476	-16.2	14.7	-16.2
6.965	-16.2	21.0	-16.2
7.479	-16.0	27.7	-16.0
7.968	-15.9	33.9	-15.9
8.481	-15.8	40.0	-15.8
8.971	-15.2	46.7	-15.2

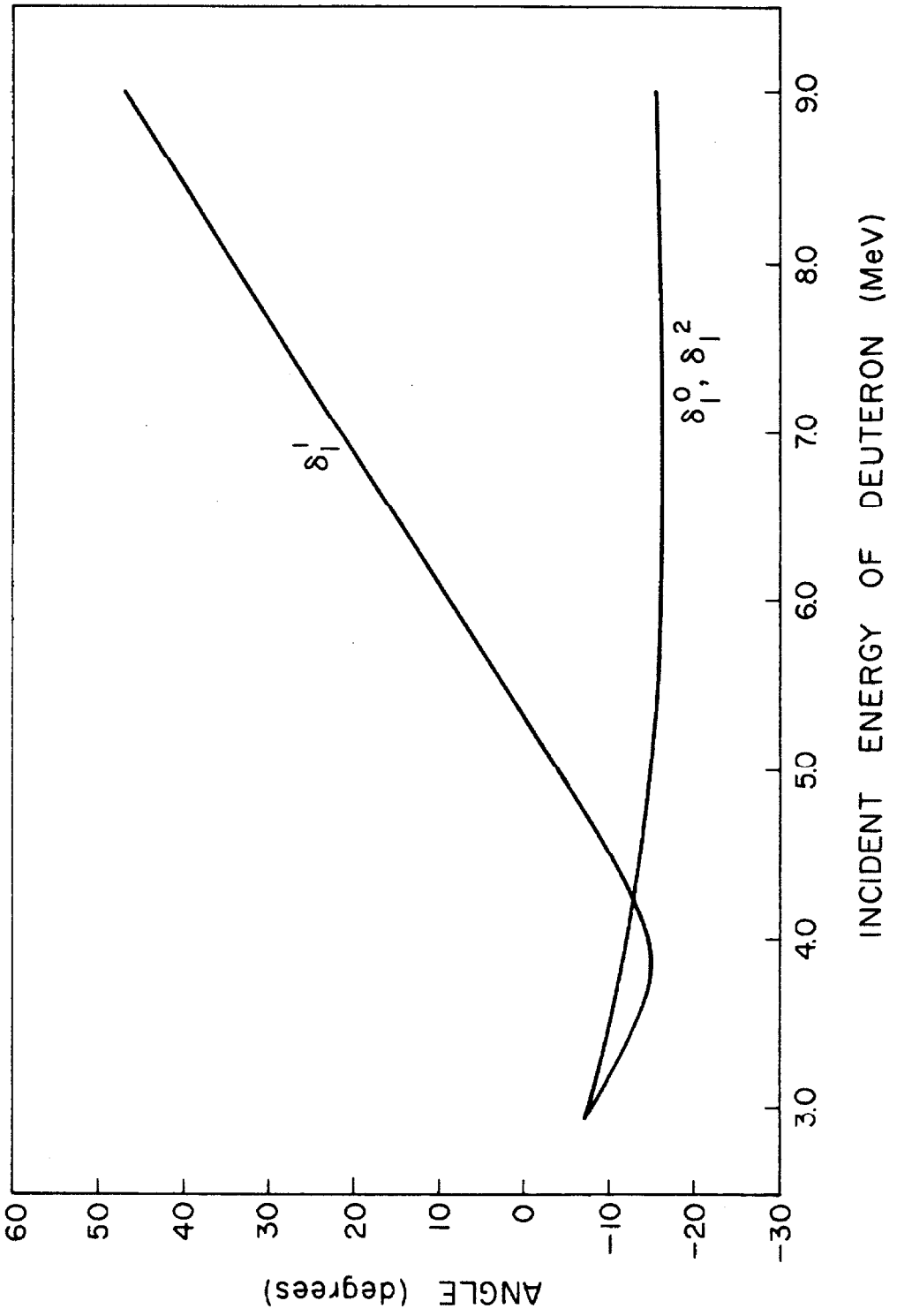
60
50
40
30
20
10
0
−10
−20
−30
ANGLE (degrees)
3.0
4.0
5.0
6.0
7.0
8.0
9.0
INCIDENT ENERGY OF DEUTERON (MeV)
δ_1^1
δ_1^0, δ_1^2

Figure 16. Imaginary parts of δ_2^3, δ_2^2 and δ_2^1.

See text, pp. 38ff.

E (MeV)	δ_2^3 (degrees)	δ_2^2 (degrees)	δ_2^1 (degrees)
2.935	0.0	0.0	0.0
3.441	0.0	0.0	0.0
3.946	0.0	0.0	0.0
4.450	0.0	0.0	0.0
4.731	0.4	0.2	0.2
4.955	0.9	0.5	0.0
5.473	2.7	1.7	0.0
5.961	5.5	3.0	0.0
6.476	10.0	4.7	0.0
6.965	15.5	6.7	0.0
7.479	22.7	8.9	0.0
7.968	30.5	11.4	0.0
8.481	40.1	14.9	0.0
8.971	51.0	18.2	0.0

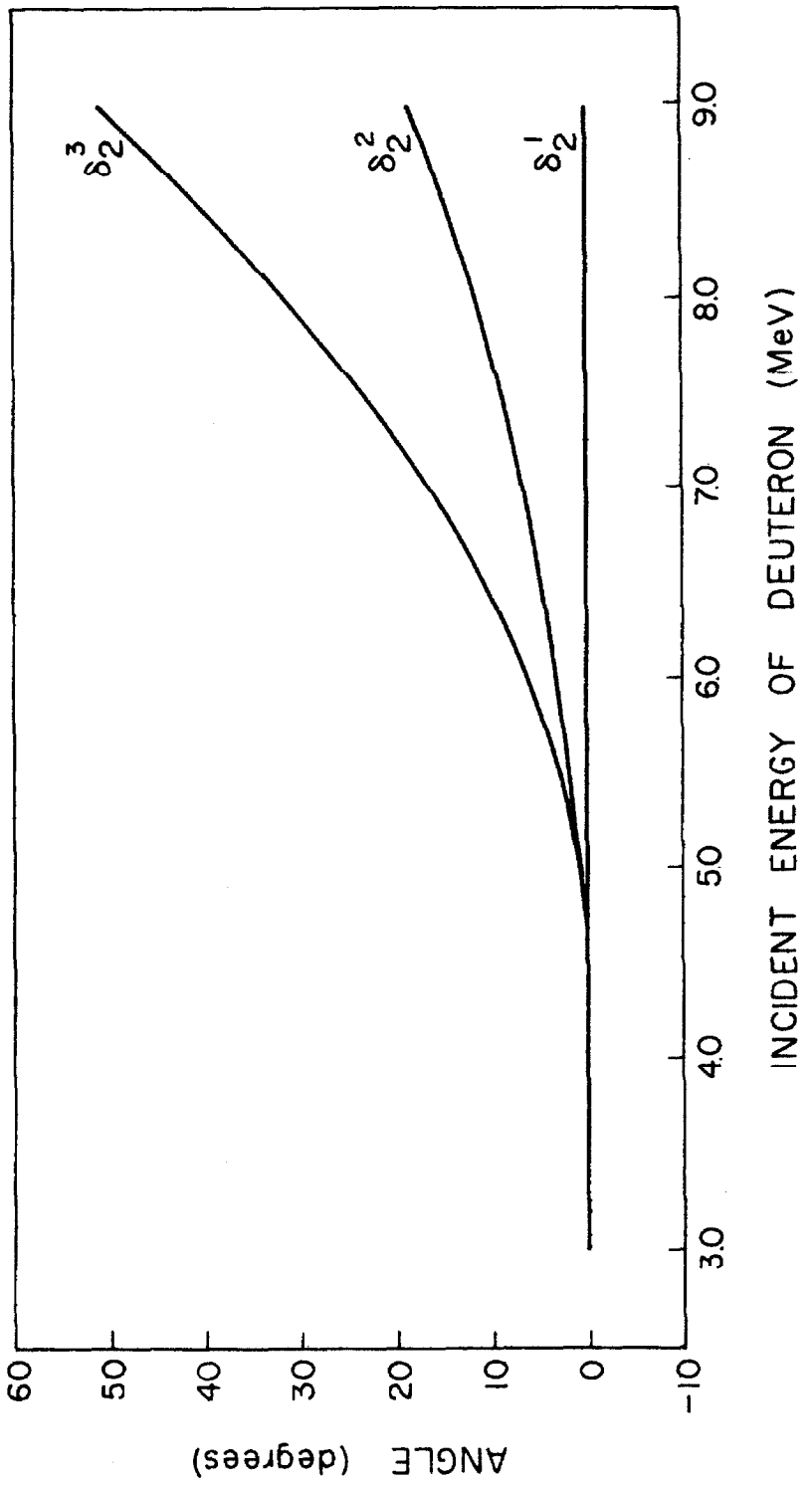
δ_2^3
δ_2^2
δ_2^1
60
50
40
30
20
10
0
-10
ANGLE (degrees)
3.0
4.0
5.0
6.0
7.0
8.0
9.0
INCIDENT ENERGY OF DEUTERON (MeV)

Figure 17. Total reaction cross-section. See text, pp. 38ff.

E (MeV)	σ_r (barns)
2.935	0.0
3.441	0.0
3.946	0.0
4.450	---
4.731	0.0137
4.955	0.0298
5.473	0.0796
5.961	0.1318
6.476	0.1879
6.965	0.2309
7.479	0.2610
7.968	0.2771
8.481	0.2867
8.971	0.2874

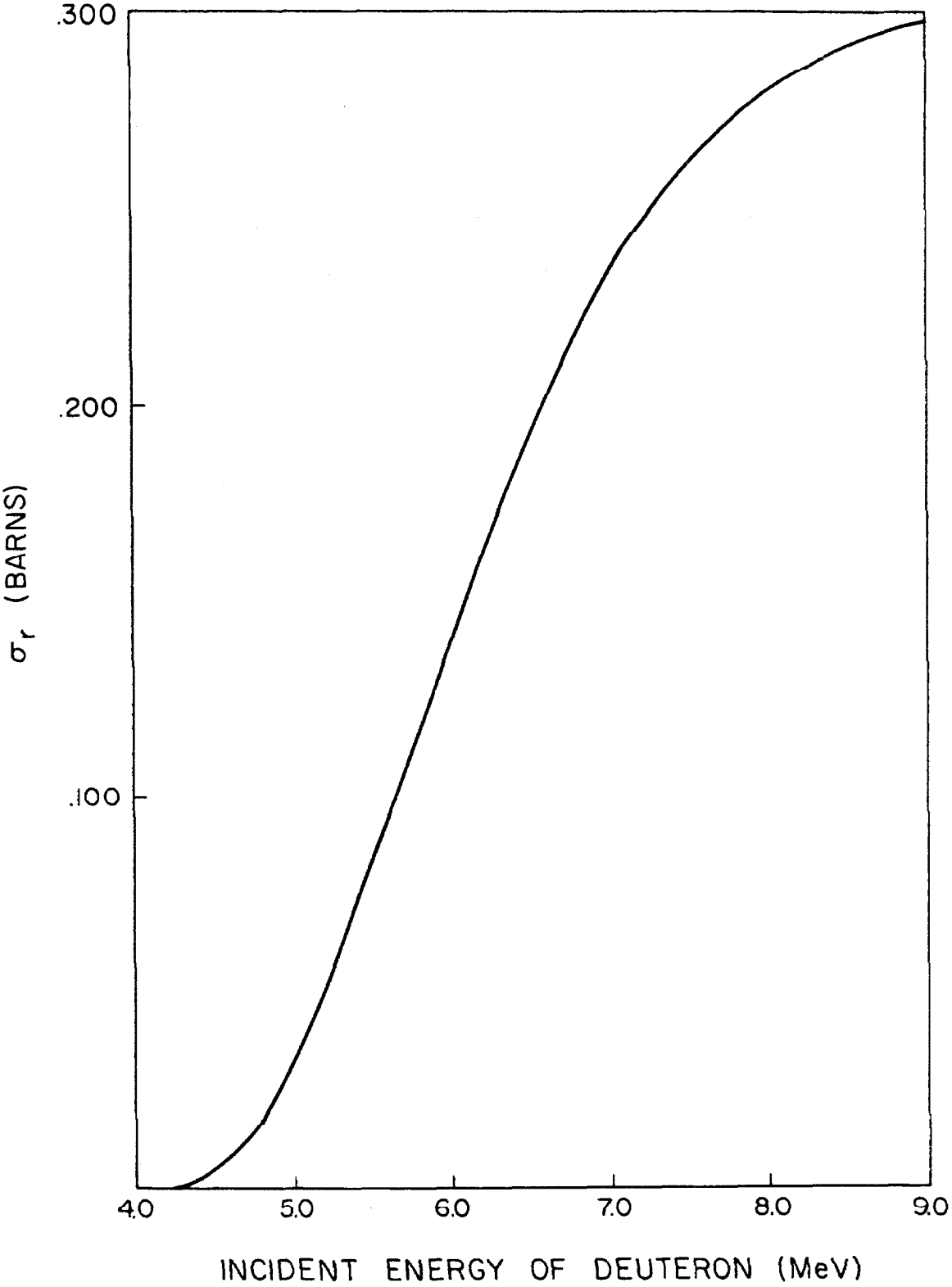
.300
.200
.100
σ_r (BARNS)
4.0
5.0
6.0
7.0
8.0
9.0
INCIDENT ENERGY OF DEUTERON (MeV)

Figure 18. Differential cross-section in the center of mass vs. center of mass angle at 2.935 ± 0.006 MeV.

$\theta_{c.m.}$ angle (degrees)	Calculated $\sigma(\theta)$ (mb/sr)	Experimental $\sigma(\theta)$ (mb/sr)	rms error (percent)
50.0	.1317	.1231	2.0
60.0	.1007	.0980	2.0
70.0	.0857	.0860	2.0
80.0	.0795	.0769	2.0
90.0	.0790	.0762	2.0
100.0	.0819	.0771	1.5
110.0	.0868	.0822	1.5
120.0	.0923	.0898	1.5
130.0	.0978	.0954	1.0

See text, p. 21 and p. 46.

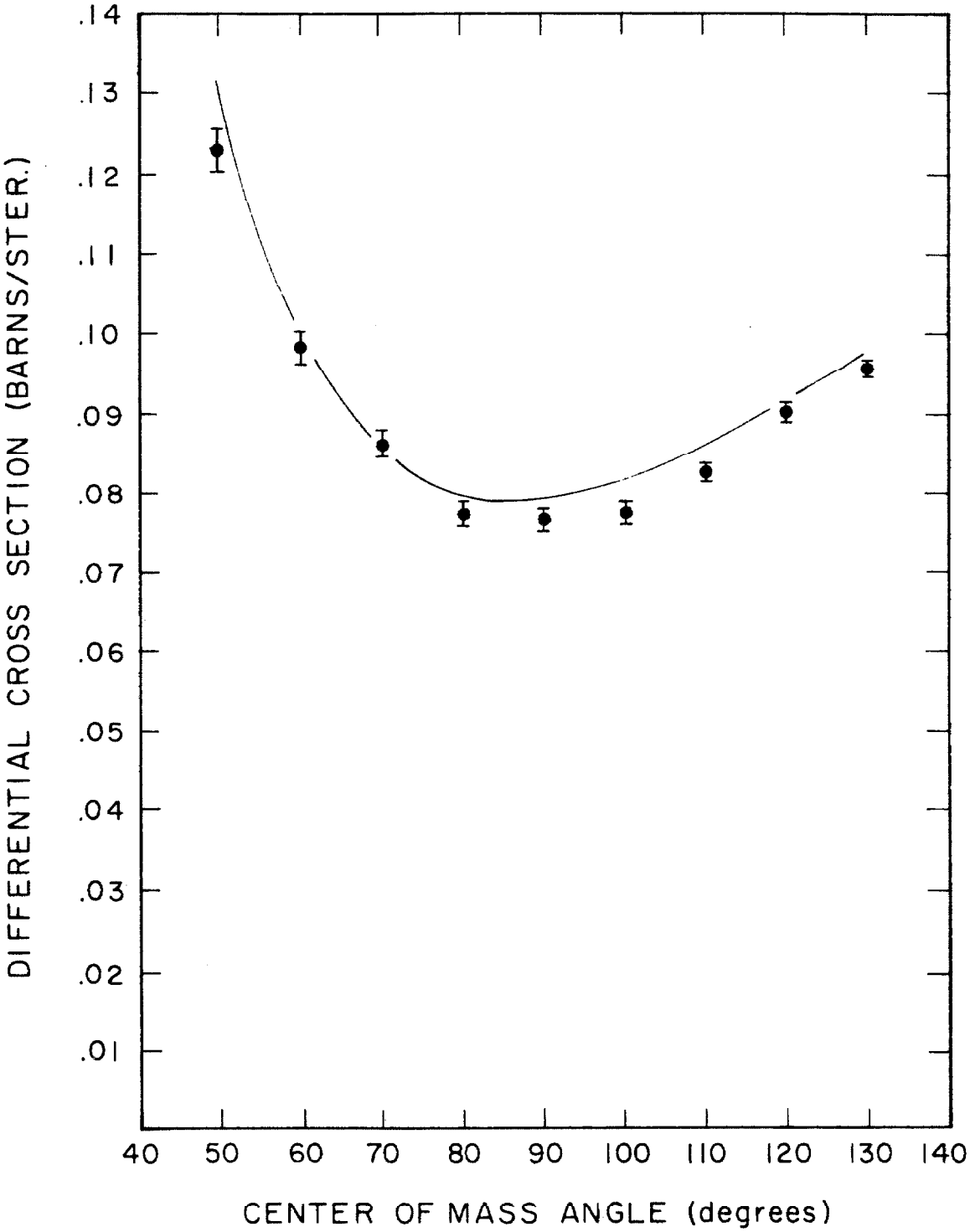
.14
.13
.12
.11
.10
.09
.08
.07
.06
.05
.04
.03
.02
.01
DIFFERENTIAL CROSS SECTION (BARNS/STER.)
40
50
60
70
80
90
100
110
120
130
140
CENTER OF MASS ANGLE (degrees)

Figure 19. Differential cross-section in the center of mass vs. center of mass angle at 3.441 ± 0.010 MeV.

$\theta_{c.m.}$ angle (degrees)	Calculated $\sigma(\theta)$ (mb/sr)	Experimental $\sigma(\theta)$ (mb/sr)	rms error (percent)
50.0	.1155	.1100	2.5
60.0	.0872	.0859	2.5
70.0	.0703	.0735	2.5
80.0	.0618	.0655	2.0
90.0	.0603	.0626	2.0
100.0	.0649	.0629	2.0
110.0	.0749	.0734	1.5
120.0	.0896	.0905	1.5
130.0	.1080	.1018	1.0

See text, p. 21 and p. 46.

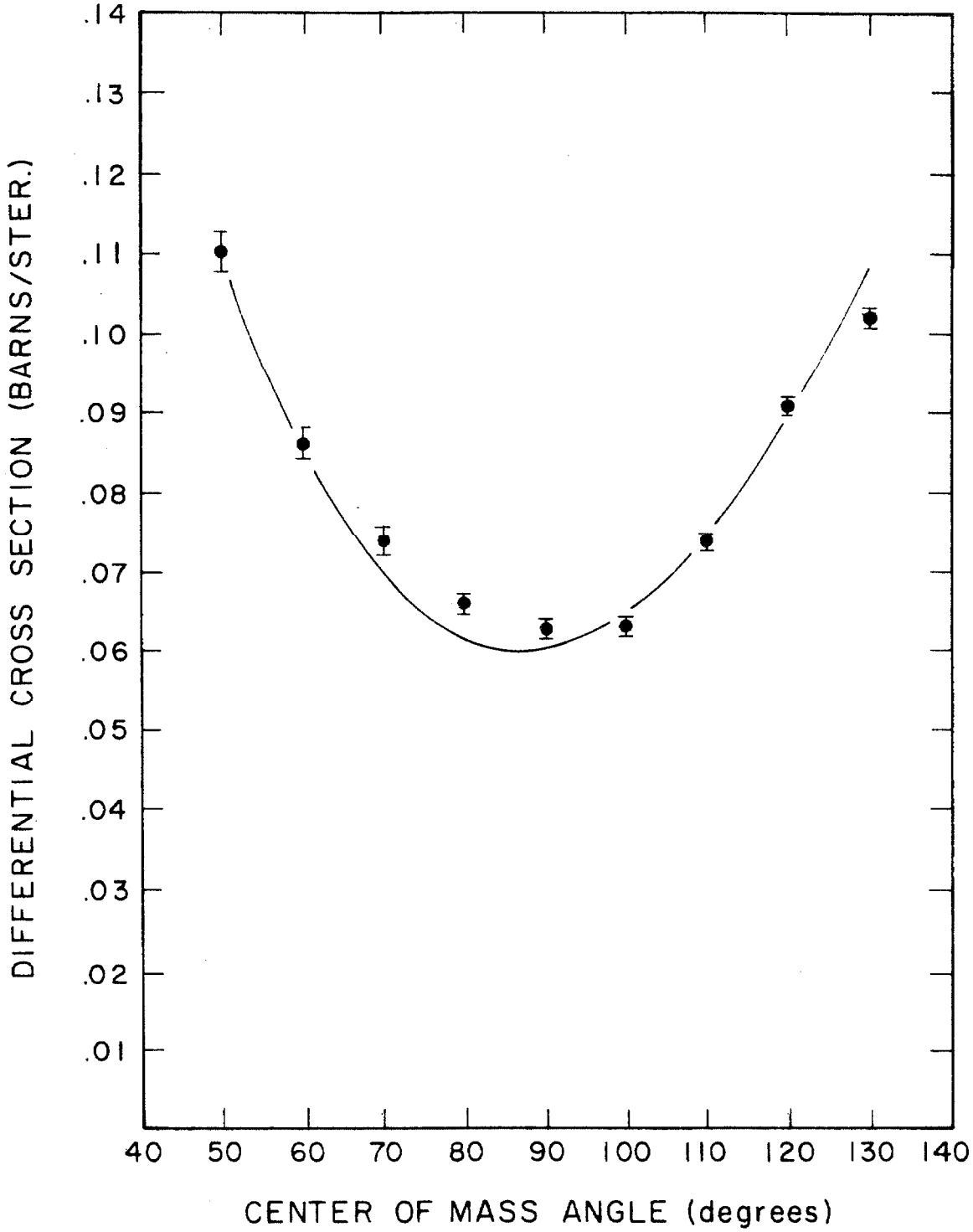
.14
.13
.12
.11
.10
.09
.08
.07
.06
.05
.04
.03
.02
.01
DIFFERENTIAL CROSS SECTION (BARNS/STER.)
40
50
60
70
80
90
100
110
120
130
140
CENTER OF MASS ANGLE (degrees)

Figure 20. Differential cross-section in the center of mass vs. center of mass angle at 3.946 ± 0.012 MeV.

$\theta_{c.m.}$ angle (degrees)	Calculated $\sigma(\theta)$ (mb/sr)	Experimental $\sigma(\theta)$ (mb/sr)	rms error (percent)
50.0	.1204	.1222	2.0
60.0	.0841	.0868	2.5
70.0	.0602	.0653	2.5
80.0	.0474	.0520	2.5
90.0	.0442	.0449	2.5
100.0	.0500	.0544	2.0
110.0	.0655	.0697	1.5
120.0	.0919	.0946	1.5
130.0	.1293	.1288	1.0

See text, p. 21 and p. 46.

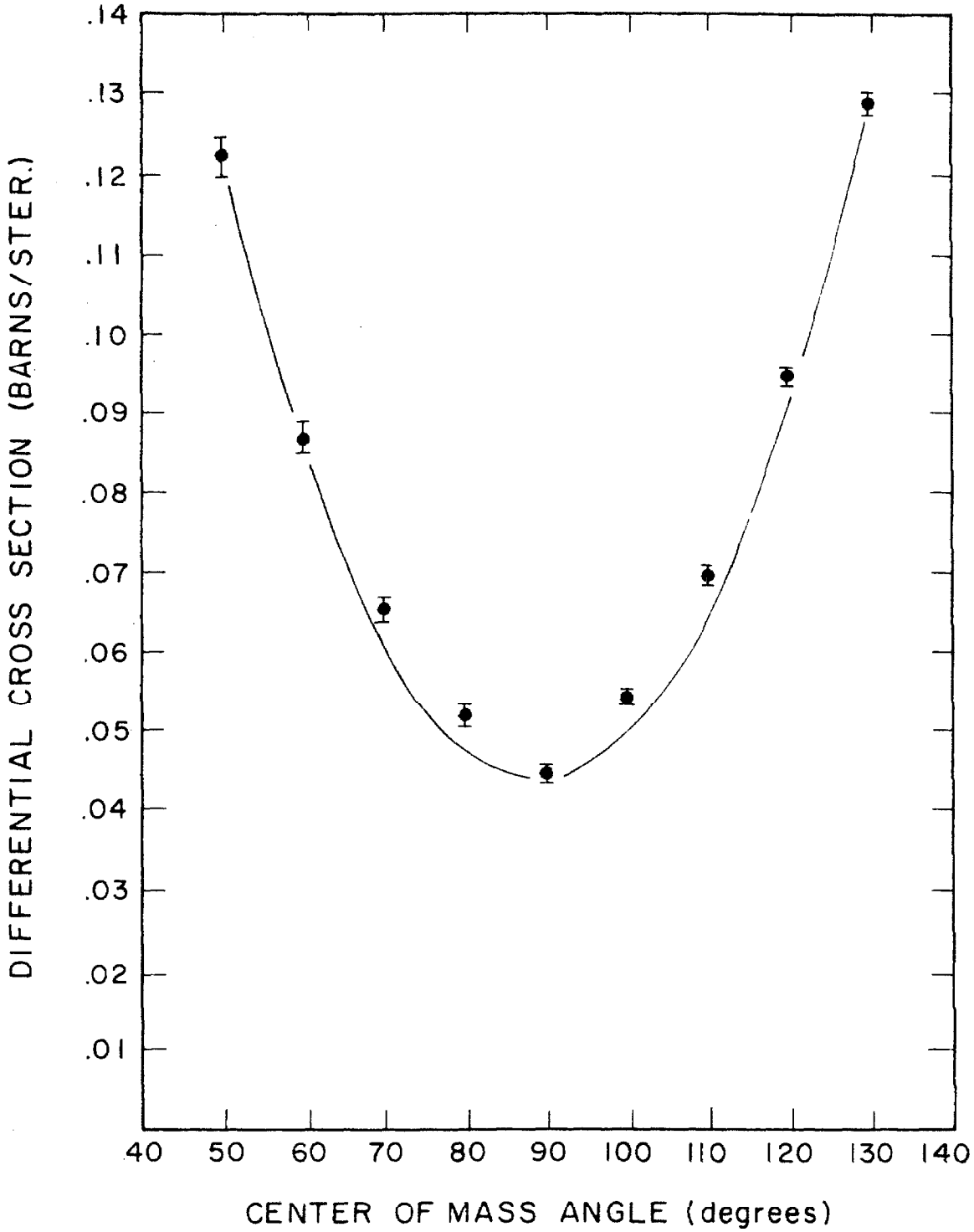
.14
.13
.12
.11
.10
.09
.08
.07
.06
.05
.04
.03
.02
.01
DIFFERENTIAL CROSS SECTION (BARNS/STER.)
40
50
60
70
80
90
100
110
120
130
140
CENTER OF MASS ANGLE (degrees)

Figure 21. Differential cross-section in the center of mass vs. center of mass angle at 4.450 ± 0.013 MeV.

$\theta_{c.m.}$ angle (degrees)	Calculated $\sigma(\theta)$ (mb/sr)	Experimental $\sigma(\theta)$ (mb/sr)	rms error (percent)
50.0	.1325	.1410	2.0
60.0	.0845	.0879	2.5
70.0	.0591	.0619	2.5
80.0	.0500	.0537	2.5
90.0	.0507	.0562	2.5
100.0	.0574	.0615	2.0
110.0	.0719	.0761	1.5
120.0	.0993	.1009	1.5
130.0	.1443	.1485	1.0

See text, p. 21 and p. 46.

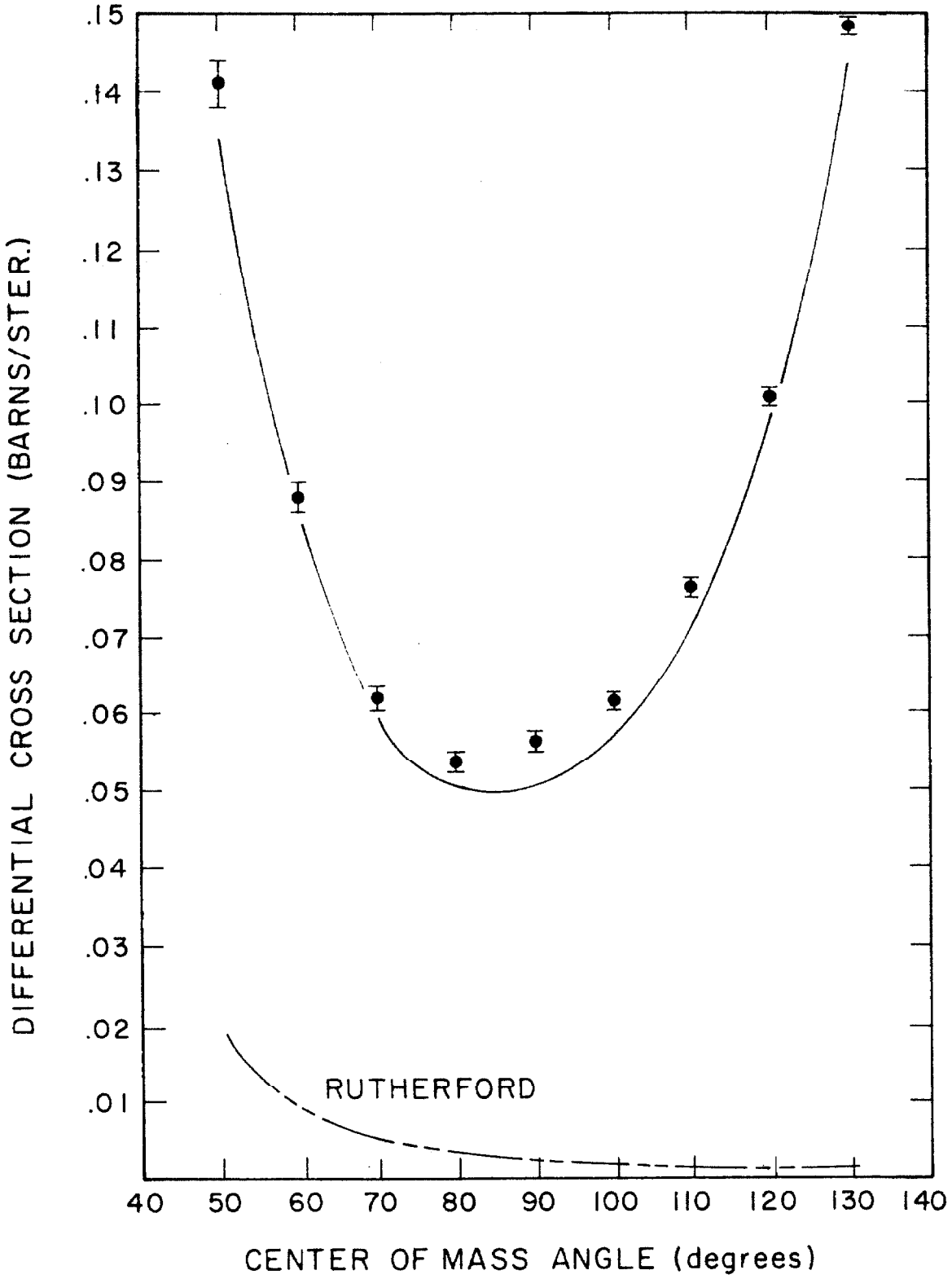
DIFFERENTIAL CROSS SECTION (BARNS/STER.)
.15
.14
.13
.12
.11
.10
.09
.08
.07
.06
.05
.04
.03
.02
.01
RUTHERFORD
40
50
60
70
80
90
100
110
120
130
140
CENTER OF MASS ANGLE (degrees)

Figure 22. Differential cross-section in the center of mass vs. center of mass angle at 4.731 ± 0.005 MeV.

$\theta_{c.m.}$ angle (degrees)	Calculated $\sigma(\theta)$ (mb/sr)	Experimental $\sigma(\theta)$ (mb/sr)	rms error (percent)	Particle Observed
17.97	.9067	.7907	3.0	d
22.44	.5406	.4770	1.5	d
29.85	.3399	.3210	1.0	d
37.20	.2415	.2260	1.0	d
44.48	.1714	.1627	1.0	d
51.67	.1200	.1131	1.0	d
58.75	.0856	.0814	1.5	d
65.70	.0656	.0661	1.5	d
72.52	.0566	.0585	1.5	d
79.18	.0547	.0580	2.0	d
85.66	.0565	.0559	2.5	d
91.95	.0600	.0620	2.5	d
98.02	.0642	.0642	3.0	d
103.88	.0694	.0654	4.0	d
110.0	.0774	.0695	3.0	α
120.0	.1005	.0911	2.0	α
130.0	.1422	.1295	1.5	α
140.0	.2042	.1995	1.5	α
150.0	.2798	.2610	1.5	α
156.0	.3256	.3030	3.0	α

See text, p. 21 and p. 46.

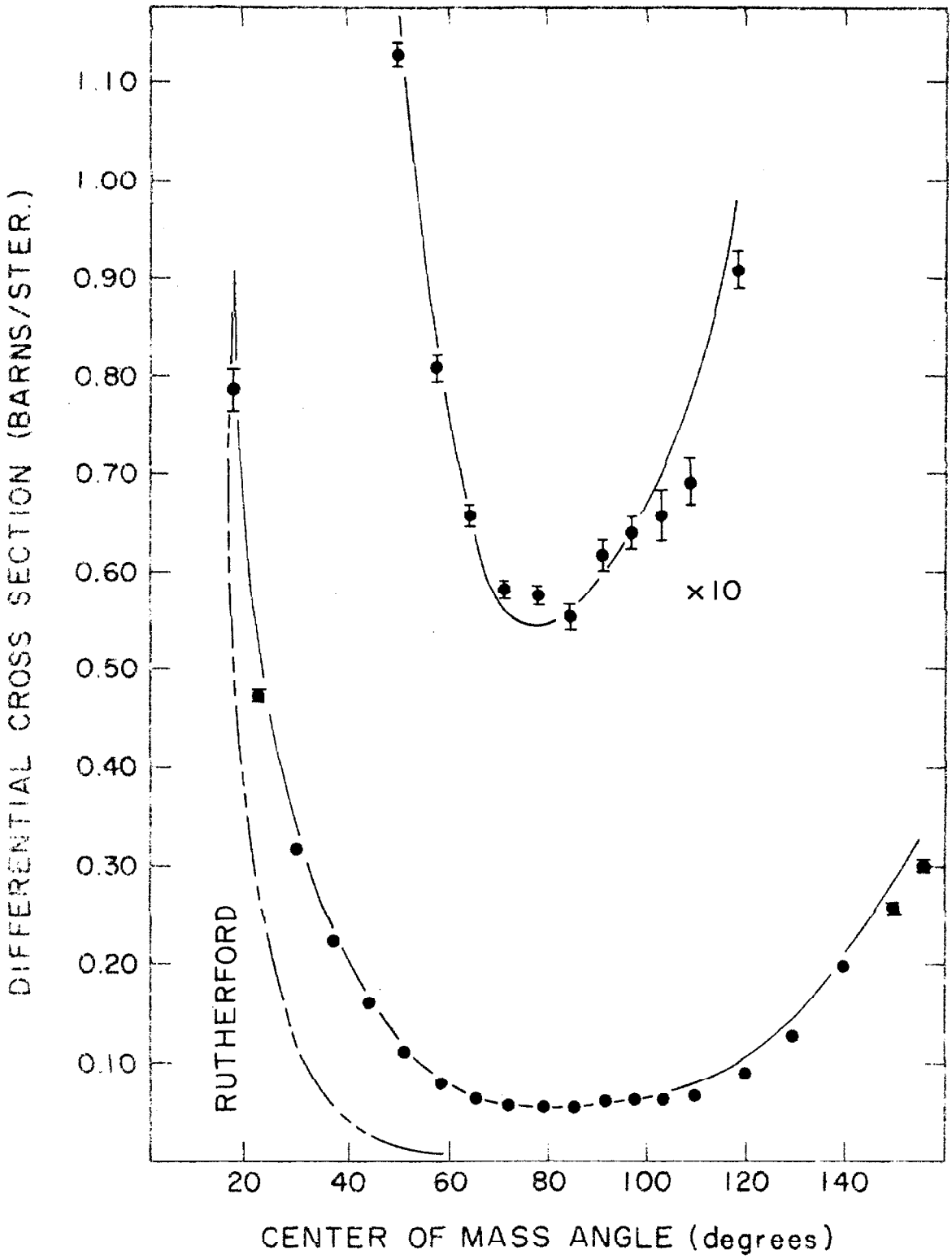
DIFFERENTIAL CROSS SECTION (BARNS/STER.)
1.10
1.00
0.90
0.80
0.70
0.60
0.50
0.40
0.30
0.20
0.10
RUTHERFORD
×10
20
40
60
80
100
120
140
CENTER OF MASS ANGLE (degrees)

Figure 23. Differential cross-section in the center of mass vs. center of mass angle at 4.955 ± 0.015 MeV.

$\theta_{c.m.}$ angle (degrees)	Calculated $\sigma(\theta)$ (mb/sr)	Experimental $\sigma(\theta)$ (mb/sr)	rms error (percent)	Particle Observed
17.97	.9020	.800	3.0	d
22.44	.5497	.489	1.5	d
29.85	.3458	.322	1.0	d
37.20	.2420	.223	1.0	d
44.48	.1685	.1577	1.0	d
51.67	.1159	.1093	1.0	d
58.75	.0818	.0772	1.5	d
65.70	.0634	.0628	1.5	d
72.52	.0564	.0554	2.0	d
79.18	.0566	.0564	2.0	d
85.66	.0601	.0576	3.5	d
98.02	---	.0691	5.0	d
110.0	.0801	.0719	2.0	α
120.0	.0999	.0922	1.0	α
130.0	.1379	.1309	1.0	α
140.0	.1968	.1857	1.5	α
150.0	.2702	.2580	1.5	α
156.0	.3153	.3020	3.0	α

See text, p. 21 and p. 46.

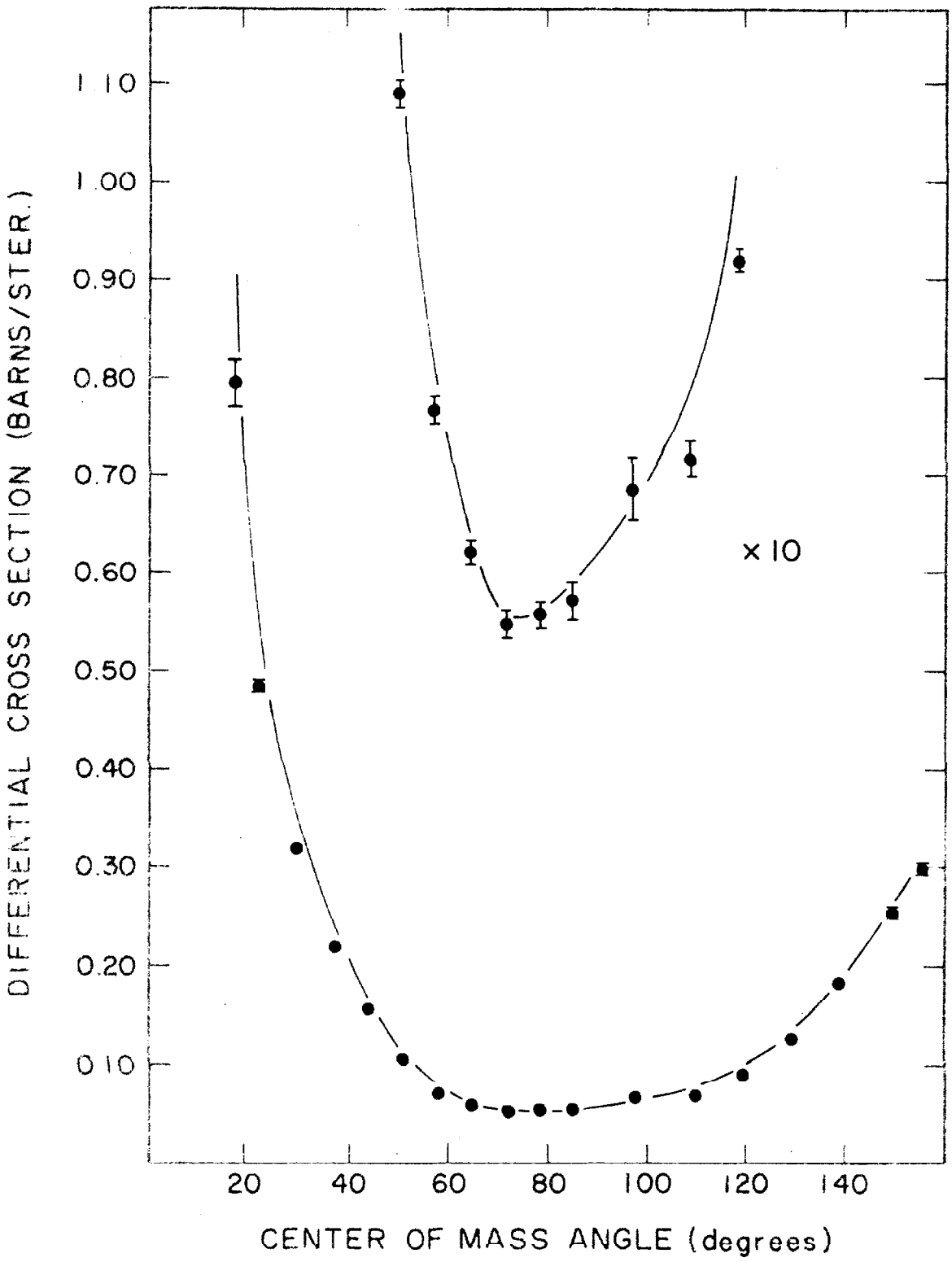
DIFFERENTIAL CROSS SECTION (BARNS/STER.)
1.10
1.00
0.90
0.80
0.70
0.60
0.50
0.40
0.30
0.20
0.10
× 10
20
40
60
80
100
120
140
CENTER OF MASS ANGLE (degrees)

Figure 24. Differential cross-section in the center of mass vs. center of mass angle at 5.473 ± 0.005 MeV.

$\theta_{c.m.}$ angle (degrees)	Calculated $\sigma(\theta)$ (mb/sr)	Experimental $\sigma(\theta)$ (mb/sr)	rms error (percent)	Particle Observed
17.97	.8421	.707	3.0	d
22.44	.5227	.449	1.5	d
29.85	.3253	.2825	1.0	d
37.20	.2220	.1956	1.0	d
44.48	.1504	.1378	1.0	d
51.67	.1011	.0948	1.5	d
58.75	.0711	.0679	1.5	d
65.70	.0568	.0540	1.5	d
72.52	.0536	.0490	2.0	d
79.18	.0568	.0519	2.5	d
85.66	.0622	.0566	2.0	d
91.95	.0675	.0608	2.5	d
98.02	.0715	.0644	2.5	d
100.0	---	.0616	1.0	α
103.88	.0747	.0656	3.5	d
110.0	.0786	.0675	2.5	α
120.0	.0918	.0831	1.5	α
130.0	.1209	.1075	1.5	α
140.0	.1700	.1578	1.5	α
150.0	.2340	.2040	1.5	α
156.0	.2741	.2520	2.5	α

See text, p. 21 and p. 46.

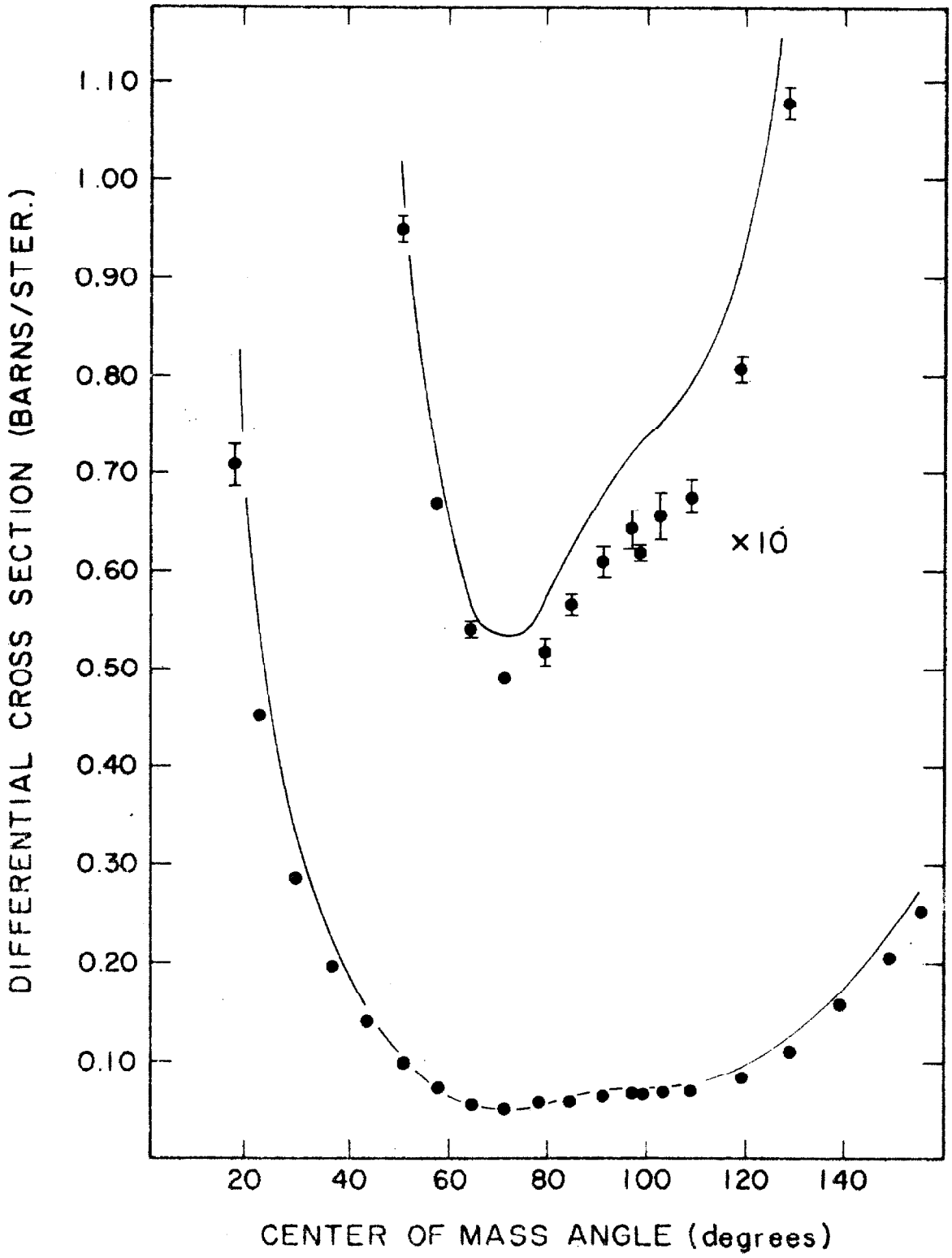
DIFFERENTIAL CROSS SECTION (BARNS/STER.)
1.10
1.00
0.90
0.80
0.70
0.60
0.50
0.40
0.30
0.20
0.10
×10
20
40
60
80
100
120
140
CENTER OF MASS ANGLE (degrees)

Figure 25. Differential cross-section in the center of mass vs. center of mass angle at 5.961 ± 0.018 MeV.

$\theta_{c.m.}$ angle (degrees)	Calculated $\sigma(\theta)$ (mb/sr)	Experimental $\sigma(\theta)$ (mb/sr)	rms error (percent)	Particle Observed
17.97	.7669	.6557	3.0	d
22.44	.4822	.4175	1.5	d
29.85	.2990	.2680	1.0	d
37.20	.2007	.1887	1.0	d
44.48	.1331	.1258	1.0	d
51.67	.0875	.0861	1.0	d
58.75	.0611	.0595	1.5	d
65.70	.0500	.0479	2.0	d
72.52	.0495	.0447	2.0	d
79.18	.0545	.0492	2.0	d
85.66	.0610	.0577	4.5	d
91.95	.0663	.0601	3.0	d
100.0	.0703	.0616	3.0	α
110.0	.0730	.0666	2.0	α
120.0	.0811	.0747	2.5	α
130.0	.1043	.0981	1.5	α
140.0	.1472	.1392	1.5	α
150.0	.2056	.1907	2.0	α
156.0	.2428	.2247	2.5	α

See text, p. 21 and p. 46.

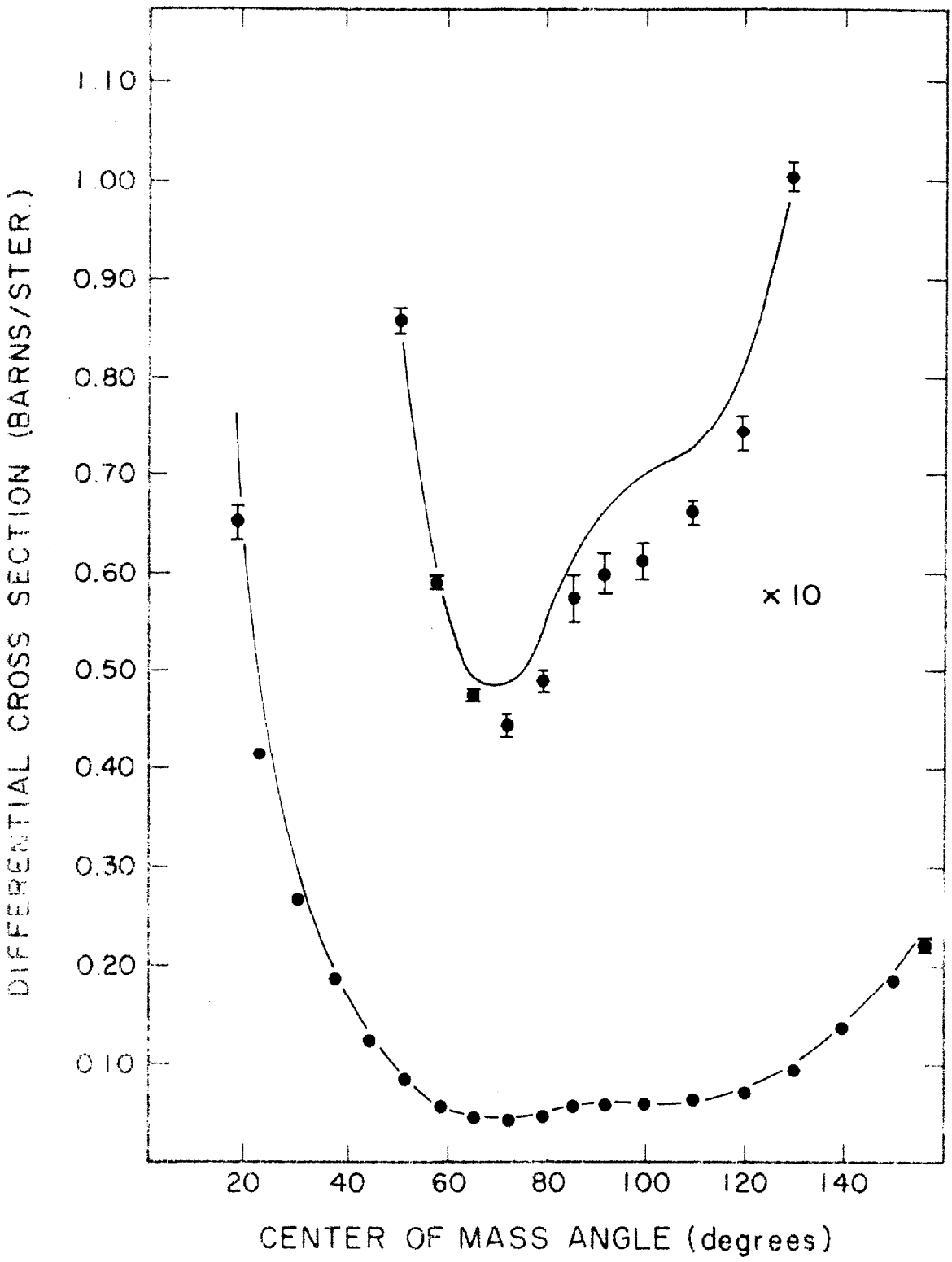
DIFFERENTIAL CROSS SECTION (BARNS/STER.)
1.10
1.00
0.90
0.80
0.70
0.60
0.50
0.40
0.30
0.20
0.10
× 10
20
40
60
80
100
120
140
CENTER OF MASS ANGLE (degrees)

Figure 26. Differential cross-section in the center of mass vs. center of mass angle at 6.476 ± 0.006 MeV.

$\theta_{c.m.}$ angle (degrees)	Calculated $\sigma(\theta)$ (mb/sr)	Experimental $\sigma(\theta)$ (mb/sr)	rms error (percent)	Particle Observed
17.97	.7033	.5930	3.0	d
22.44	.4507	.4050	1.0	d
29.85	.2798	.261	1.0	d
37.20	.1841	.1710	1.0	d
44.48	.1180	.1128	1.0	d
51.67	.0746	.0713	1.5	d
58.75	.0510	.0499	2.0	d
65.70	.0431	.0393	2.0	d
72.52	.0457	.0421	2.0	d
79.18	.0531	.0467	2.0	d
85.66	.0610	.0551	2.0	d
91.95	.0666	.0590	2.5	d
98.02	.0689	.0625	3.0	d
100.0	.0690	.0600	3.0	α
103.88	.0687	.0624	3.0	d
110.0	.0674	.0633	1.5	α
120.0	.0698	.0675	1.5	α
130.0	.0872	.0816	1.5	α
140.0	.1257	.1190	1.5	α
150.0	.1815	.1663	1.5	α
156.0	.2180	.1880	2.5	α

See text, p. 21 and p. 46.

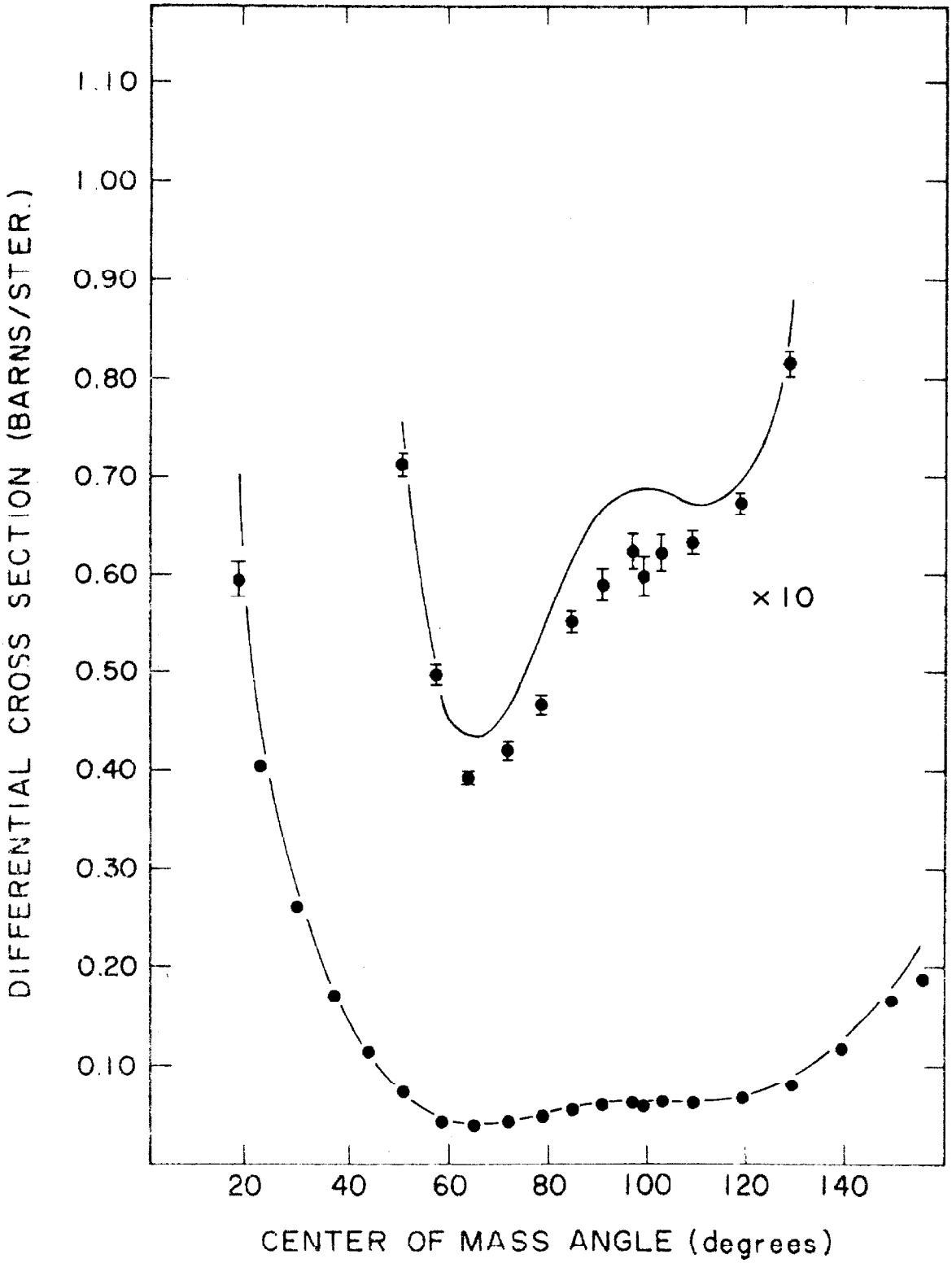
DIFFERENTIAL CROSS SECTION (BARNS/STER.)
1.10
1.00
0.90
0.80
0.70
0.60
0.50
0.40
0.30
0.20
0.10
× 10
20
40
60
80
100
120
140
CENTER OF MASS ANGLE (degrees)

Figure 27. Differential cross-section in the center of mass vs. center of mass angle at 6.965 ± 0.021 MeV.

$\theta_{c.m.}$ angle (degrees)	Calculated $\sigma(\theta)$ (mb/sr)	Experimental $\sigma(\theta)$ (mb/sr)	rms error (percent)	Particle Observed
17.97	.6506	.5940	3.0	d
22.44	.4224	.3825	1.0	d
29.85	.2614	.2505	1.0	d
37.20	.1684	.1614	1.0	d
44.48	.1043	.1039	1.0	d
51.67	.0632	.0634	1.5	d
58.75	.0425	.0411	2.0	d
65.70	.0377	.0377	2.0	d
72.52	.0432	.0401	2.0	d
79.18	.0530	.0472	2.0	d
85.66	.0623	.0557	2.5	d
91.95	.0682	.0616	2.5	d
98.02	.0697	.0655	3.5	d
100.0	.0694	.0659	1.5	α
103.88	.0677	.0639	4.5	d
109.50	.0641	.0602	4.0	d
110.0	.0638	.0621	1.5	α
120.0	.0603	.0615	1.5	α
130.0	.0715	.0686	1.5	α
140.0	.1043	.1022	1.5	α
150.0	.1560	.1438	1.5	α
156.0	.1908	.1761	2.5	α

See text, p. 21 and p. 46.

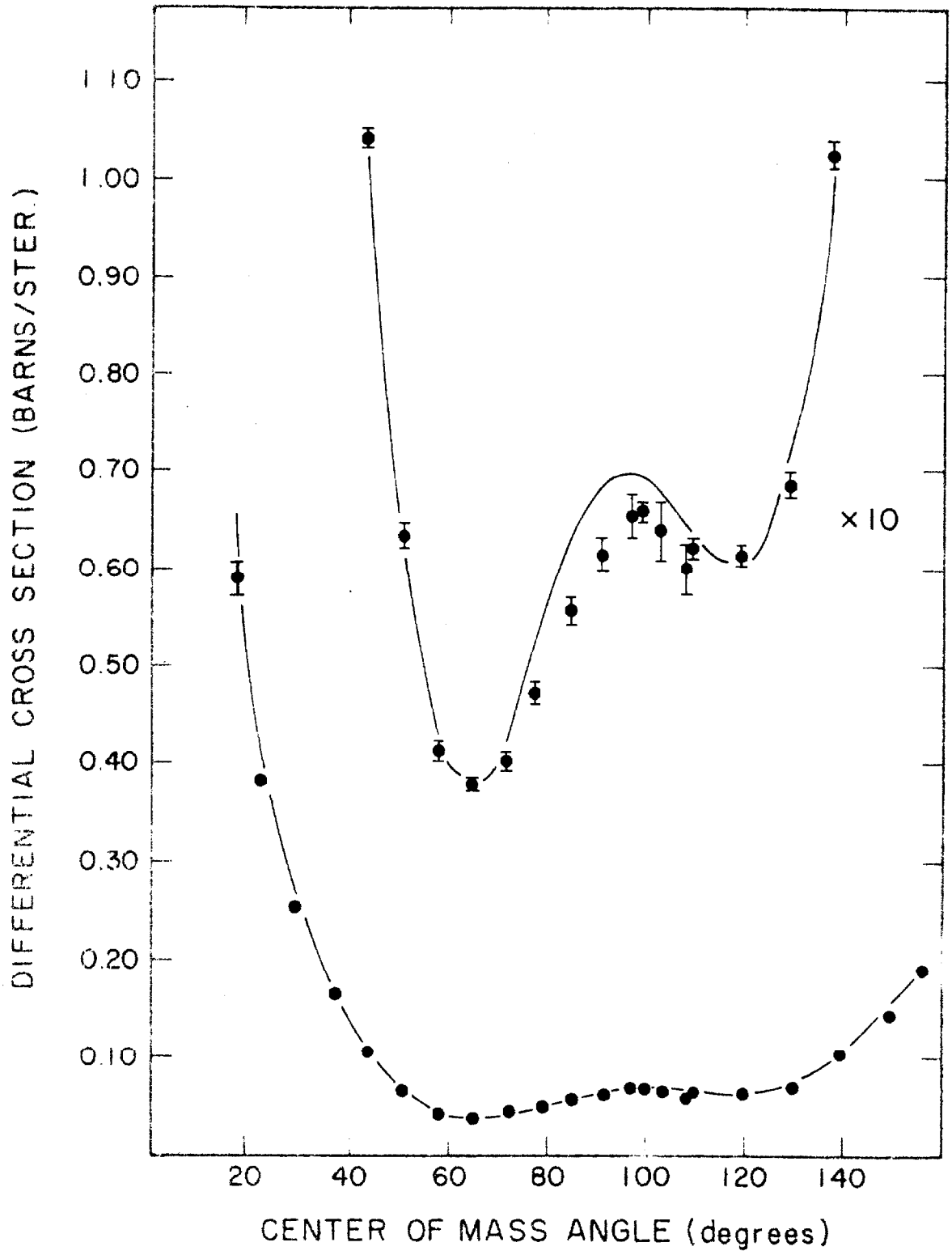
DIFFERENTIAL CROSS SECTION (BARNS/STER.)
1.10
1.00
0.90
0.80
0.70
0.60
0.50
0.40
0.30
0.20
0.10
×10
20
40
60
80
100
120
140
CENTER OF MASS ANGLE (degrees)

Figure 28. Differential cross-section in the center of mass vs. center of mass angle at 7.479 ± 0.007 MeV.

$\theta_{c.m.}$ angle (degrees)	Calculated $\sigma(\theta)$ (mb/sr)	Experimental $\sigma(\theta)$ (mb/sr)	rms error (percent	Particle Observed
17.97	.5982	.5220	3.0	d
22.44	.3930	.3540	1.5	d
29.85	.2430	.2200	1.5	d
37.20	.1541	.1404	1.5	d
44.48	.0927	.0870	1.5	d
51.67	.0541	.0501	1.5	d
58.75	.0358	.0316	2.5	d
65.70	.0334	.0301	2.5	d
72.52	.0410	.0367	2.5	d
79.18	.0524	.0489	2.0	d
85.66	.0628	.0585	2.5	d
91.95	.0689	.0634	2.5	d
98.02	.0700	.0646	2.5	d
103.88	.0669	.0634	3.5	d
109.50	.0615	.0618	4.5	d
120.0	.0529	.0540	3.0	α
130.0	.0582	.0507	2.5	α
140.0	.0847	.0782	1.5	α
150.0	.1305	.1142	2.5	α
156.0	.1623	.1357	4.0	α

See text, p. 21 and p. 46.

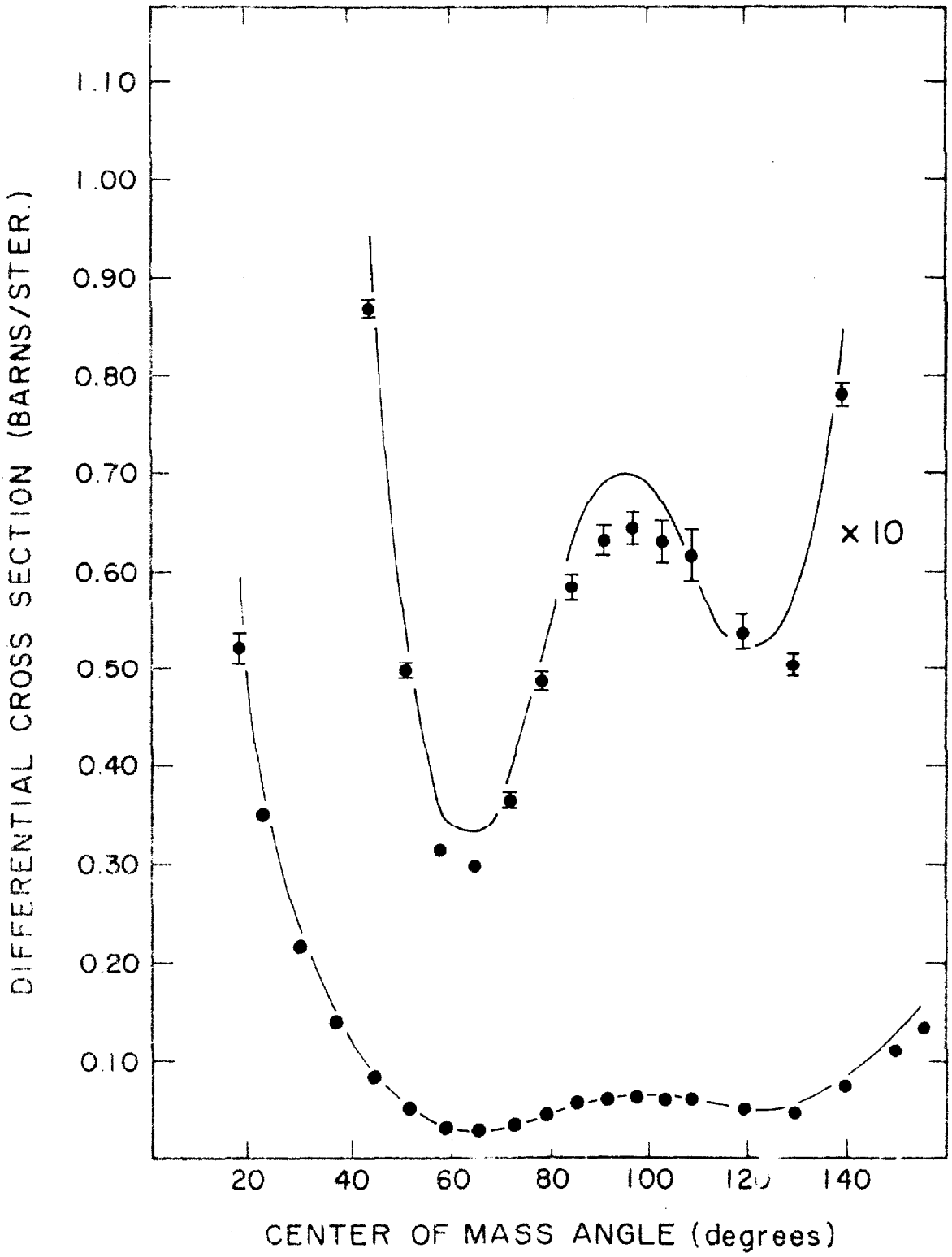
DIFFERENTIAL CROSS SECTION (BARNS/STER.)
1.10
1.00
0.90
0.80
0.70
0.60
0.50
0.40
0.30
0.20
0.10
× 10
20
40
60
80
100
120
140
CENTER OF MASS ANGLE (degrees)

Figure 29. Differential cross-section in the center of mass vs. center of mass angle at 7.968 ± 0.024 MeV. Data of Burge et al. (1952) at 8 MeV are represented by ◇.

$\theta_{c.m.}$ angle (degrees)	Calculated $\sigma(\theta)$ (mb/sr)	Experimental $\sigma(\theta)$ (mb/sr)	rms error (percent)	Particle Observed
17.97	.5487	.5310	3.0	d
22.44	.3649	.3560	1.5	d
29.85	.2273	.2220	1.0	d
37.20	.1438	.1340	1.0	d
44.48	.0856	.0787	1.0	d
51.67	.0491	.0438	1.5	d
58.75	.0321	.0279	2.0	d
65.70	.0305	.0266	2.0	d
72.52	.0385	.0349	2.0	d
79.18	.0503	.0488	2.0	d
85.66	.0609	.0592	2.0	d
90.00	.0658	.0606	4.0	α
91.95	.0673	.0665	1.0	d
98.02	.0684	.0681	2.5	d
100.0	.0678	.0656	2.0	α
103.88	.0652	.0634	3.5	d
109.50	.0593	.0608	4.5	d
110.0	.0587	.0590	1.5	α
120.0	.0485	.0482	2.5	α
130.0	.0495	.0497	1.5	α
140.0	.0700	.0703	1.5	α
150.0	.1086	.1064	1.5	α
156.0	.1362	.1316	2.5	α

See text, p. 21 and p. 46.

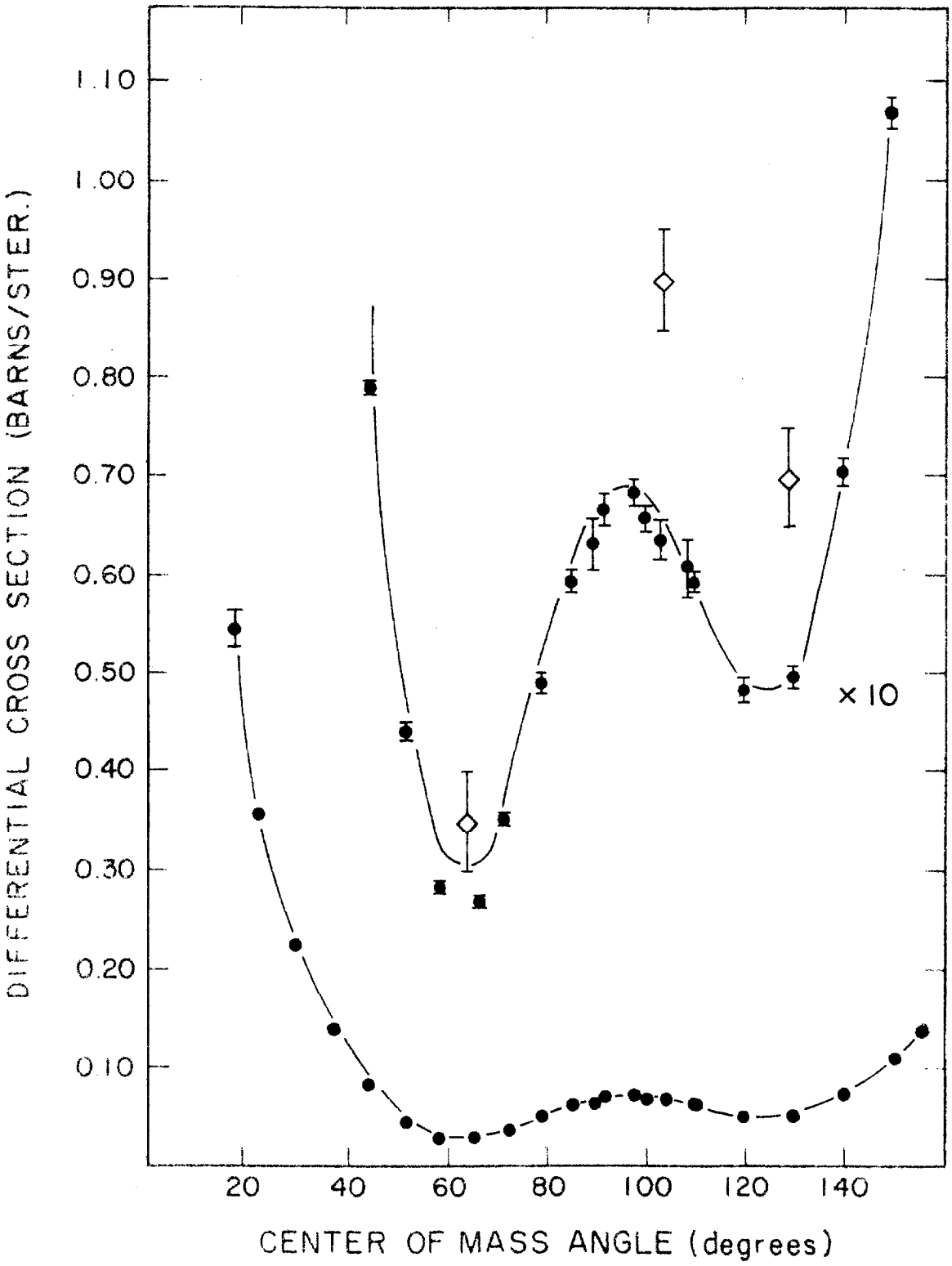
DIFFERENTIAL CROSS SECTION (BARNS/STER.)
1.10
1.00
0.90
0.80
0.70
0.60
0.50
0.40
0.30
0.20
0.10
× 10
20
40
60
80
100
120
140
CENTER OF MASS ANGLE (degrees)

Figure 30. Differential cross-section in the center of mass vs. center of mass angle at 8.481 ± 0.008 MeV.

$\theta_{c.m.}$ angle (degrees)	Calculated $\sigma(\theta)$ (mb/sr)	Experimental $\sigma(\theta)$ (mb/sr)	rms error (percent)	Particle Observed
17.97	.4972	.4707	3.0	d
22.44	.3349	.3295	1.5	d
29.85	.2111	.2067	1.0	d
37.20	.1343	.1225	1.0	d
44.48	.0800	.0670	1.5	d
51.67	.0457	.0368	2.0	d
58.75	.0295	.0224	2.5	d
65.70	.0279	.0213	3.0	d
72.52	.0355	.0325	2.5	d
79.18	.0469	.0443	2.5	d
85.66	.0574	.0570	2.5	d
91.95	.0640	.0656	2.5	d
98.02	.0656	.0652	3.5	d
100.0	.0651	.0649	5.5	α
103.88	.0629	.0649	3.5	d
110.0	.0567	.0528	5.5	α
120.0	.0457	.0423	3.5	α
130.0	.0434	.0402	3.0	α
140.0	.0576	.0574	2.0	α
150.0	.0879	.0859	3.0	α
156.0	.1102	.1049	4.5	α

See text, p. 21 and p. 46.

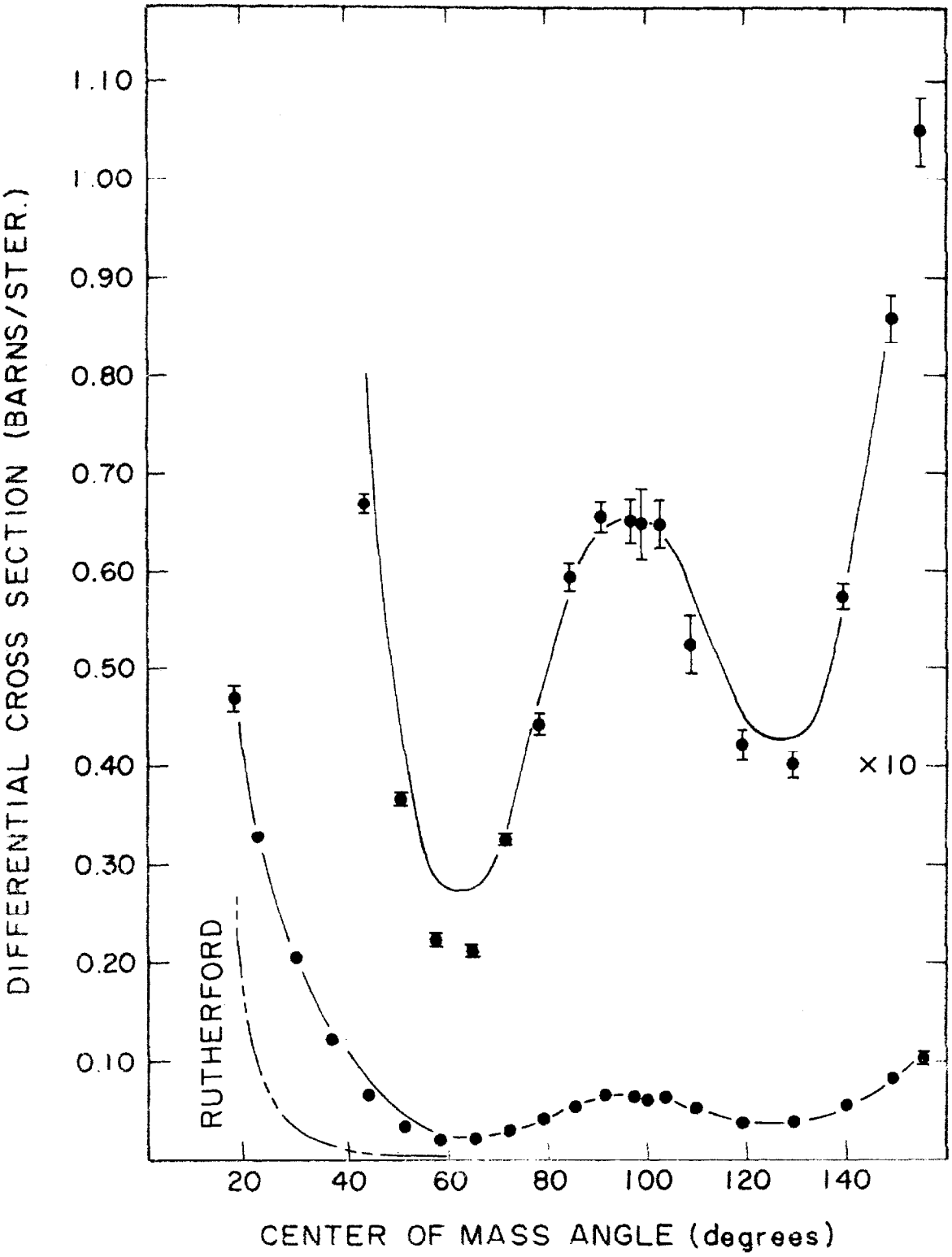
DIFFERENTIAL CROSS SECTION (BARNS/STER.)
1.10
1.00
0.90
0.80
0.70
0.60
0.50
0.40
0.30
0.20
0.10
RUTHERFORD
×10
20
40
60
80
100
120
140
CENTER OF MASS ANGLE (degrees)

Figure 31. Differential cross-section in the center of mass vs. center of mass angle at 8.971 ± 0.027 MeV.

$\theta_{c.m.}$ angle (degrees)	Calculated $\sigma(\theta)$ (mb/sr)	Experimental $\sigma(\theta)$ (mb/sr)	rms error (percent)	Particle Observed
17.97	.4528	.4680	3.0	d
22.44	.3100	.3280	1.5	d
29.85	.1992	.2023	1.0	d
37.20	.1286	.1186	1.0	d
44.48	.0776	.0614	1.0	d
51.67	.0448	.0298	2.0	d
58.75	.0288	.0173	2.5	d
65.70	.0266	.0211	2.5	d
72.52	.0333	.0318	2.0	d
79.18	.0440	.0444	2.0	d
85.66	.0541	.0580	2.0	d
90.0	.0591	.0613	3.0	d
91.95	.0607	.0663	2.0	d
98.02	.0628	.0689	2.0	d
100.0	---	.0636	2.5	α
103.88	.0607	.0681	2.5	d
103.88	.0607	.0670	2.5	d
109.5	.0557	.0587	3.5	d
110.0	.0552	.0553	2.0	α
114.87	.0497	.0493	5.5	d
120.0	.0442	.0445	2.0	α
130.0	.0397	.0395	2.0	α
140.0	.0488	.0529	2.0	α
150.0	.0719	.0794	2.0	α
156.0	.0896	.0998	3.0	α

See text, p. 21 and p. 46.

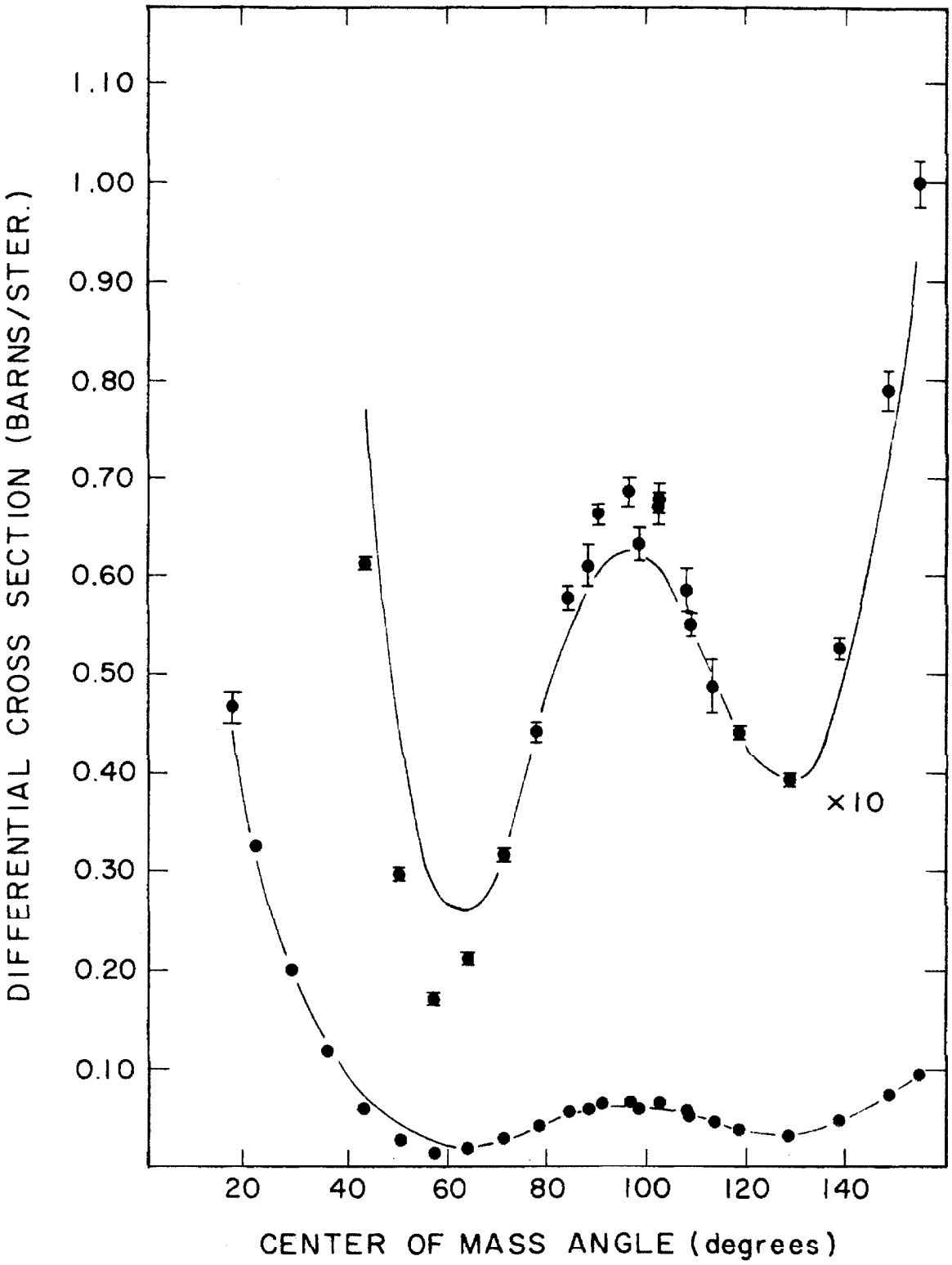
DIFFERENTIAL CROSS SECTION (BARNS/STER.)
1.10
1.00
0.90
0.80
0.70
0.60
0.50
0.40
0.30
0.20
0.10
20
40
60
80
100
120
140
CENTER OF MASS ANGLE (degrees)
×10

Figure 32. Differential cross-section in the center of mass vs. center of mass angle at 9.482 ± 0.009 MeV.

$\theta_{c.m.}$ angle (degrees)	Experimental $\sigma(\theta)$ (mb/sr)	rms error (percent)	Particle Observed
17.97	.4520	3.0	d
22.44	.3140	1.5	d
29.85	.1939	1.0	d
37.20	.1072	1.0	d
44.48	.0557	1.5	d
51.67	.0252	2.5	d
58.75	.0140	4.0	d
65.70	.0175	3.5	d
72.52	.0314	2.5	d
79.18	.0436	2.5	d
85.66	.0558	2.5	d
91.95	.0648	2.5	d
98.02	.0656	3.0	d
100.0	.0655	4.5	α
110.0	.0553	4.5	α
120.0	.0368	3.5	α
130.0	.0343	2.5	α
140.0	.0432	2.0	α
150.0	.0670	2.5	α
156.0	.0824	4.5	α

See text, p. 21 and p. 46.

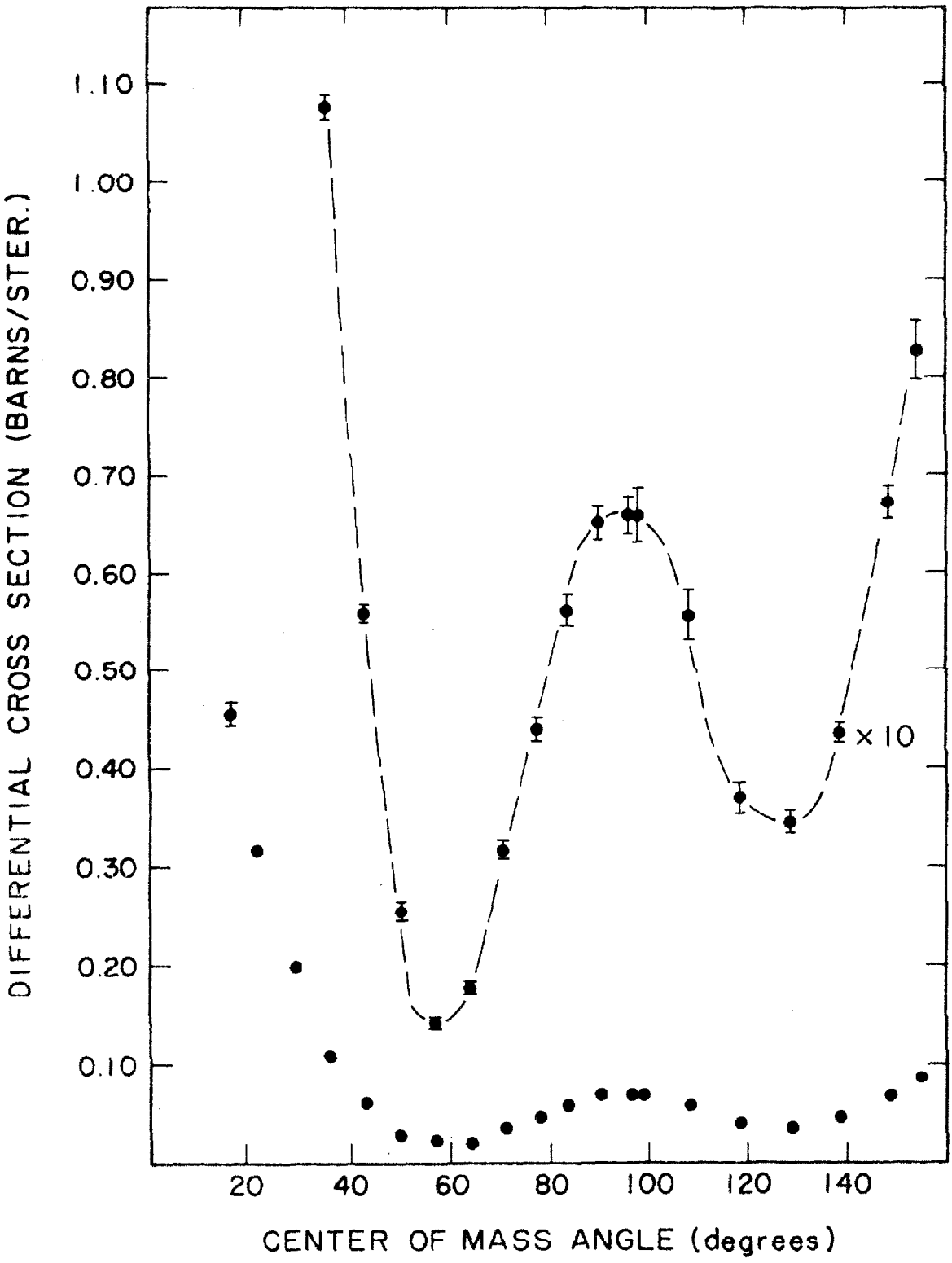
DIFFERENTIAL CROSS SECTION (BARNS/STER.)
1.10
1.00
0.90
0.80
0.70
0.60
0.50
0.40
0.30
0.20
0.10
× 10
20
40
60
80
100
120
140
CENTER OF MASS ANGLE (degrees)

Figure 33. Differential cross-section in the center of mass vs. center of mass angle at 9.973 ± 0.030 MeV.

$\theta_{c.m.}$ angle (degrees)	Experimental $\sigma(\theta)$ (mb/sr)	rms error (percent)	Particle Observed
17.97	.4420	3.0	d
22.44	.3190	1.0	d
29.85	.1913	1.0	d
37.20	.1056	1.0	d
44.48	.0509	1.5	d
51.67	.0211	2.0	d
58.75	.0123	3.0	d
65.70	.0173	2.5	d
72.52	.0287	2.5	d
79.18	.0436	2.0	d
85.66	.0563	2.0	d
90.0	.0649	2.5	α
91.95	.0645	2.0	d
98.02	.0708	2.0	d
100.0	.0670	2.0	α
103.88	.0621	2.5	d
109.50	.0554	3.5	d
110.0	.0518	3.5	α
120.0	.0415	1.5	α
130.0	.0329	1.5	α
140.0	.0411	1.5	α
150.0	.0627	2.0	α
156.0	.0782	3.0	α

See text, p. 21 and p. 46.

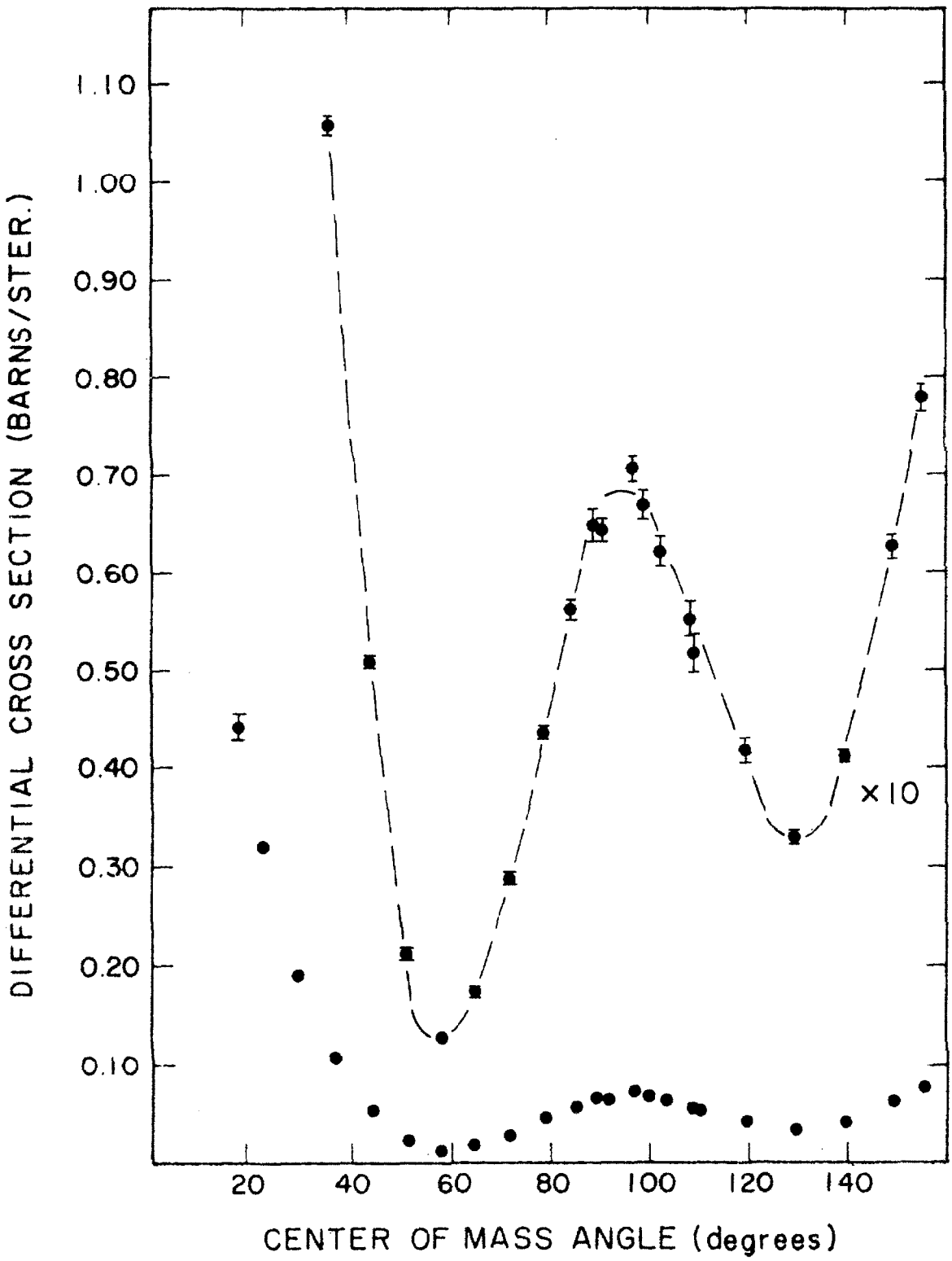
DIFFERENTIAL CROSS SECTION (BARNS/STER.)
1.10
1.00
0.90
0.80
0.70
0.60
0.50
0.40
0.30
0.20
0.10
×10
20
40
60
80
100
120
140
CENTER OF MASS ANGLE (degrees)

Figure 34. Differential cross-section in the center of mass vs. center of mass angle at 10.474 ± 0.032 MeV.

$\theta_{c.m.}$ angle (degrees)	Experimental $\sigma(\theta)$ (mb/sr)	rms error (percent)	Particle Observed
17.97	.4310	2.0	d
22.44	.2900	1.5	d
29.85	.1841	1.0	d
37.20	.1034	1.0	d
44.48	.0449	1.5	d
51.67	.0180	2.5	d
58.75	.0101	3.5	d
65.70	.0143	3.5	d
72.52	.0272	2.5	d
79.18	.0414	2.0	d
85.66	.0536	2.5	d
91.95	.0605	2.5	d
98.02	.0639	2.5	d
100.0	.0522	2.5	α
103.88	.0630	3.0	d
109.50	.0564	3.5	d
110.0	.0522	3.0	α
120.0	.0387	2.0	α
130.0	.0298	1.5	α
140.0	.0364	1.5	α
150.0	.0504	4.0	α
156.0	.0696	3.5	α

See text, p. 21 and p. 46.

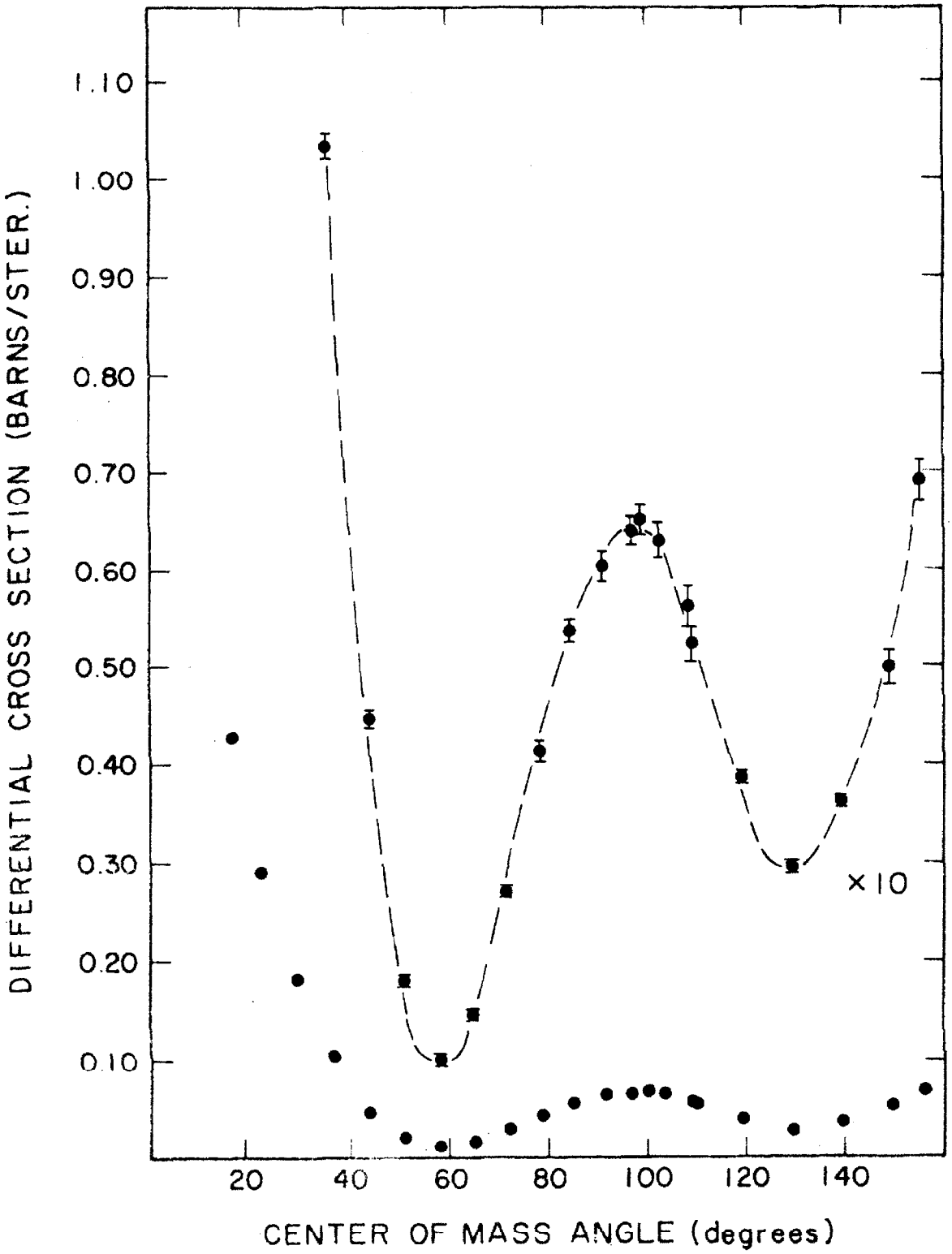
DIFFERENTIAL CROSS SECTION (BARNS/STER.)
1.10
1.00
0.90
0.80
0.70
0.60
0.50
0.40
0.30
0.20
0.10
×10
20
40
60
80
100
120
140
CENTER OF MASS ANGLE (degrees)

Figure 35. Differential cross-section in the center of mass vs. center of mass angle at 10.975 ± 0.033 MeV.

$\theta_{c.m.}$ angle (degrees)	Experimental $\sigma(\theta)$ (mb/sr)	rms error (percent)	Particle Observed
17.97	.4310	2.0	d
22.44	.3020	1.0	d
29.85	.1860	1.0	d
37.20	.0946	1.0	d
44.48	.0430	1.5	d
51.67	.0156	2.5	d
58.75	.0086	3.5	d
65.70	.0146	3.0	d
72.52	.0273	2.5	d
79.18	.0425	2.0	d
85.66	.0534	2.5	d
90.0	.0629	3.0	α
91.95	.0606	3.0	d
98.02	.0648	3.0	d
100.0	.0682	2.5	α
110.0	.0543	2.5	α
120.0	.0370	2.5	α
130.0	.0271	2.5	α
140.0	.0321	2.0	α
150.0	.0489	2.5	α
156.0	.0648	3.5	α

See text, p. 21 and p. 46.

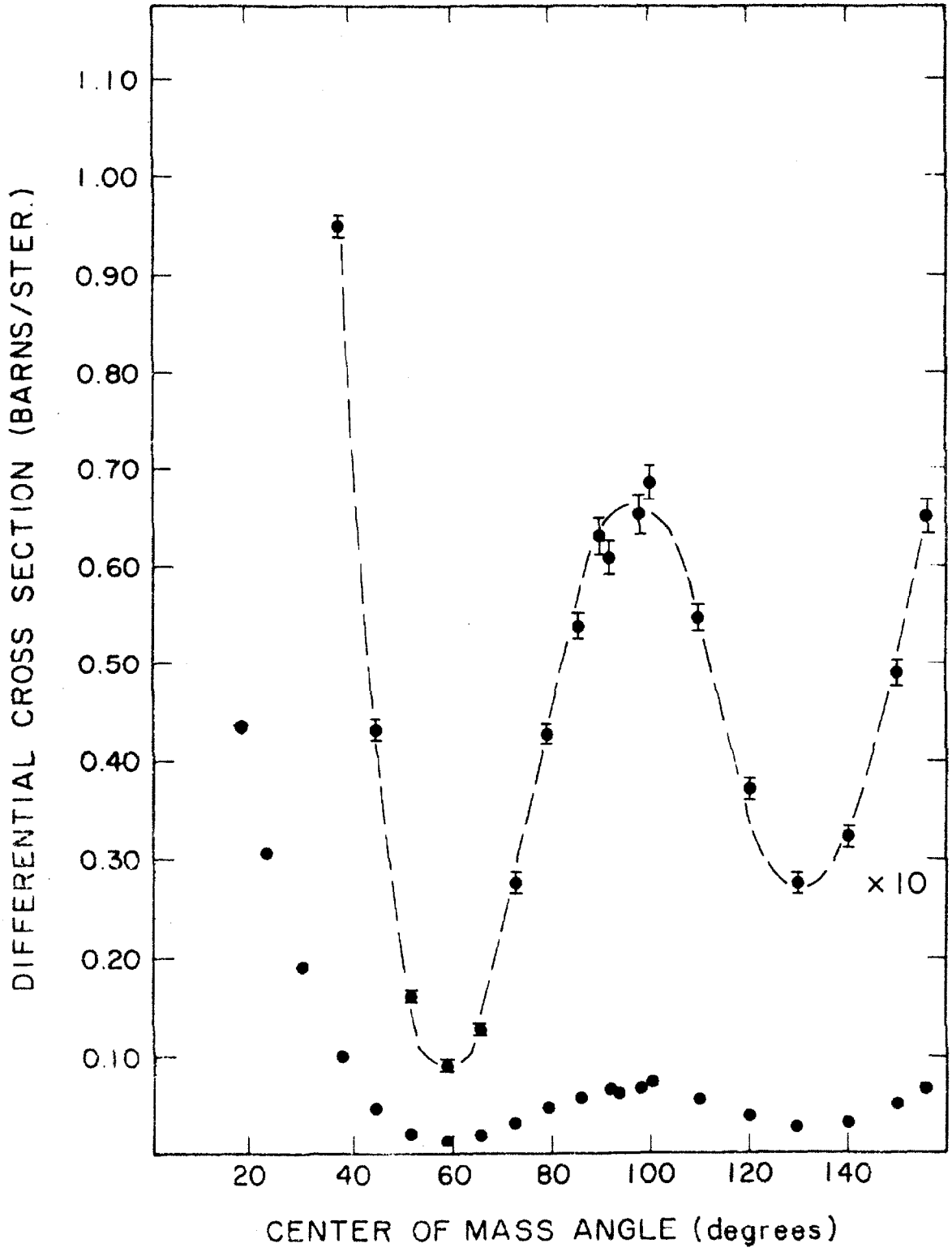
DIFFERENTIAL CROSS SECTION (BARNS/STER.)
1.10
1.00
0.90
0.80
0.70
0.60
0.50
0.40
0.30
0.20
0.10
× 10
20
40
60
80
100
120
140
CENTER OF MASS ANGLE (degrees)

Figure 36. Differential cross-section in the center of mass vs. center of mass angle at 11.475 ± 0.034 MeV.

$\theta_{c.m.}$ angle (degrees)	Experimental $\sigma(\theta)$ (mb/sr)	rms error (percent)	Particle Observed
17.97	.4150	2.0	d
22.44	.3040	1.0	d
29.85	.1823	1.0	d
37.20	.0934	1.0	d
44.48	.0392	1.5	d
51.67	.0141	2.5	d
58.75	.0072	4.5	d
65.70	.0140	3.5	d
72.52	.0241	3.0	d
79.18	.0397	2.5	d
85.66	.0509	3.0	d
91.95	.0580	2.5	d
98.02	.0590	3.5	d
100.0	.0625	3.0	α
103.88	.0544	4.0	d
109.50	.0531	4.5	d
110.0	.0528	3.0	α
120.0	.0347	3.0	α
130.0	.0263	2.0	α
140.0	.0304	1.5	α
150.0	.0443	2.5	α
156.0	.0574	3.5	α

See text, p. 21 and p. 46.

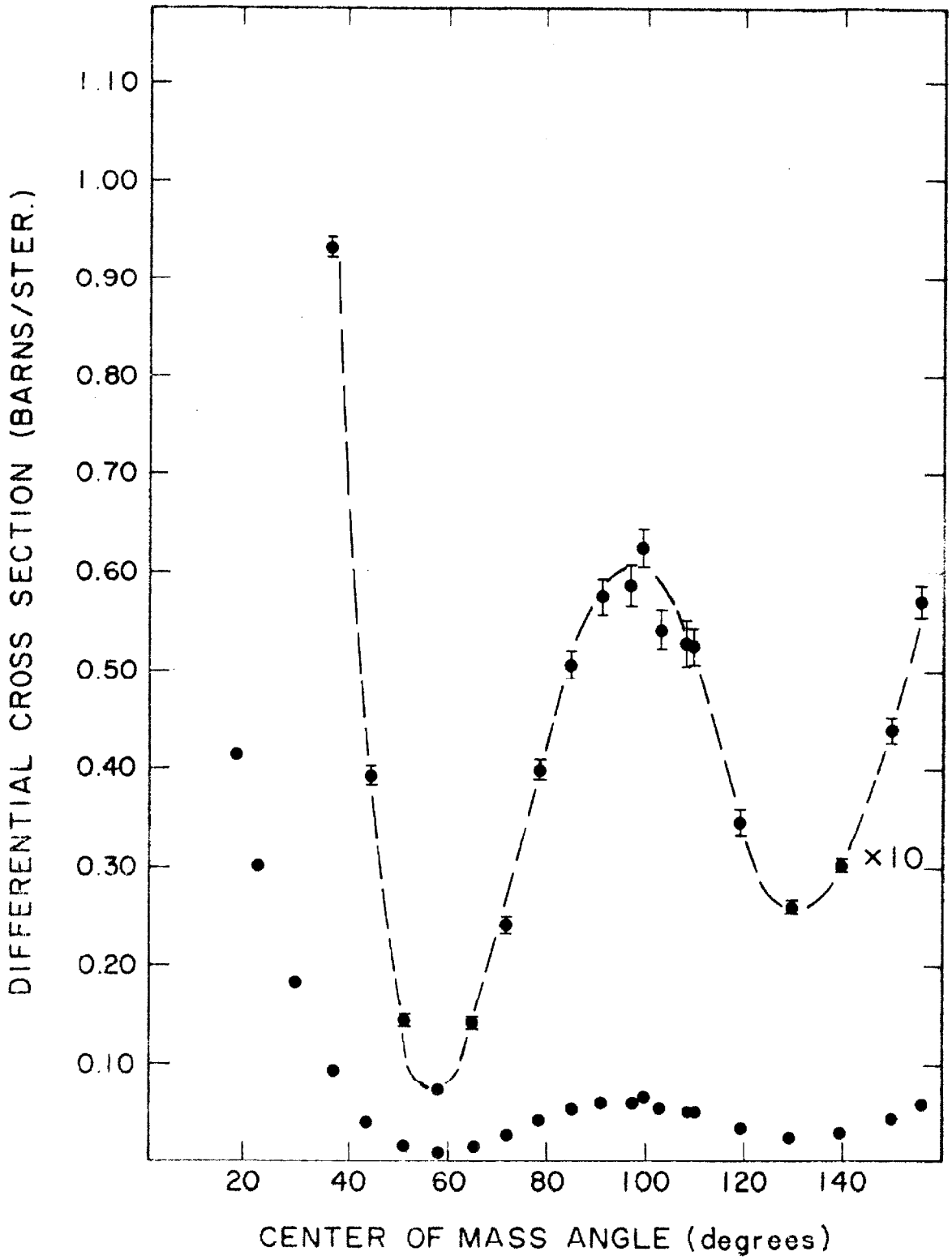
DIFFERENTIAL CROSS SECTION (BARNS/STER.)
1.10
1.00
0.90
0.80
0.70
0.60
0.50
0.40
0.30
0.20
0.10
20
40
60
80
100
120
140
CENTER OF MASS ANGLE (degrees)
×10

Figure 37. Differential cross-section in the center of mass vs. energy of incident deuteron at 17.97 $\pm$ 0.14° c.m. The values of the cross-sections are tabulated in the captions of Figures 22 through 36. The error bars plotted are the absolute instead of the relative errors listed in Figures 22 through 36. See text, p. 21 and p. 46.

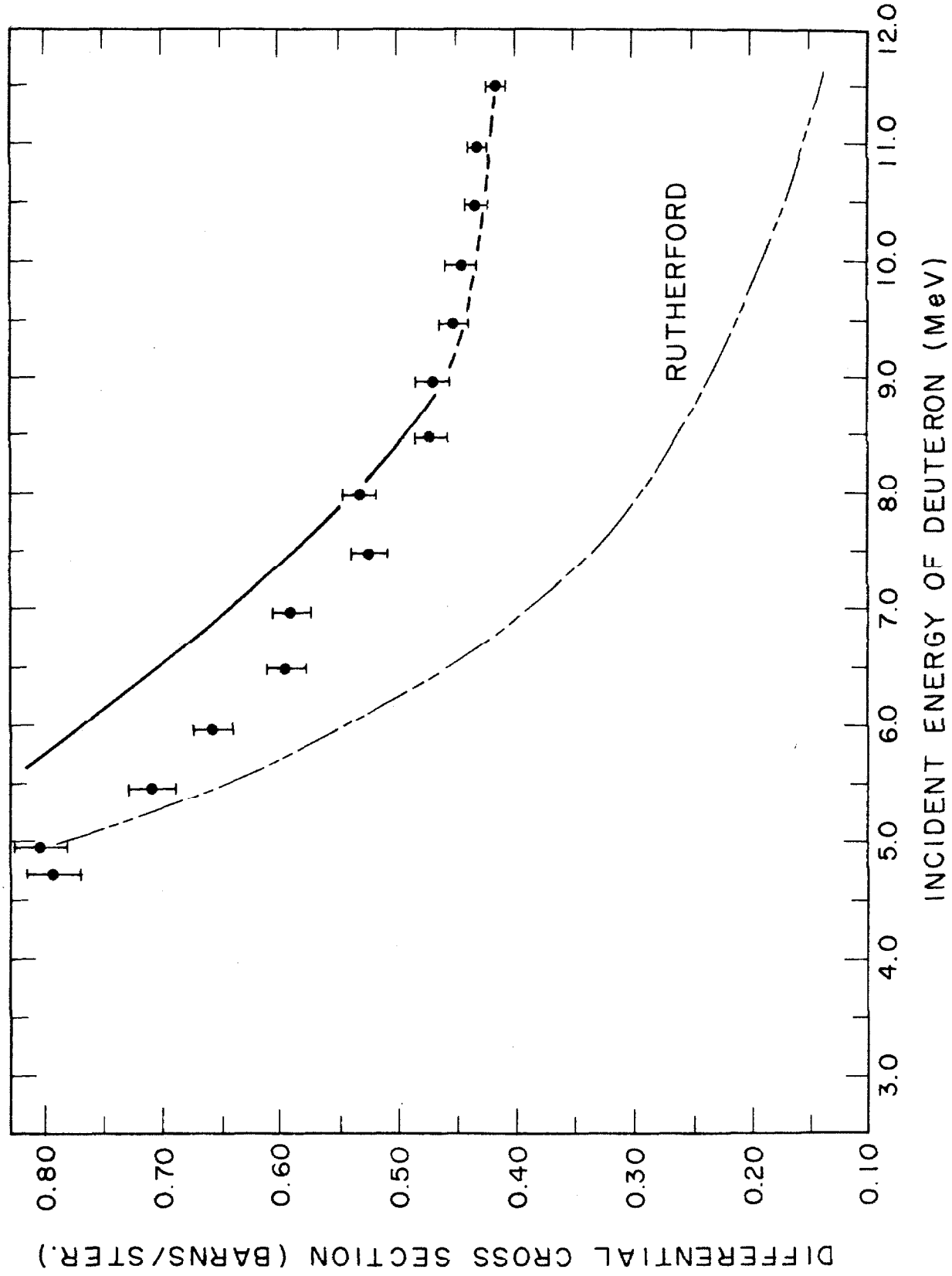
DIFFERENTIAL CROSS SECTION (BARNS/STER.)
0.80
0.70
0.60
0.50
0.40
0.30
0.20
0.10
3.0
4.0
5.0
6.0
7.0
8.0
9.0
10.0
11.0
12.0
INCIDENT ENERGY OF DEUTERON (MeV)
RUTHERFORD

Figure 38. Differential cross-section in the center of mass vs. energy of incident deuteron at 54.8 ± 0.14° c.m.

Energy (MeV)	Experiment σ(θ) (mb/sr)	rms error (percent)	Energy (MeV)	Experiment σ(θ) (mb/sr)	rms error (percent)
2.958±.009	.1032	1.5	6.179±.019	.0690	1.5
2.958±.009	.1015	1.5	6.379±.019	.0637	1.5
3.159±.009	.0987	1.5	6.780±.021	.0572	1.5
3.361±.010	.0982	1.5	6.981±.021	.0556	1.5
3.562±.011	.0945	1.5	7.181±.022	.0471	2.0
3.764±.011	.0964	1.5	7.382±.022	.0430	2.0
3.965±.012	.1005	1.5	7.582±.023	.0412	2.0
4.166±.012	.0989	1.5	7.783±.023	.0375	2.0
4.367±.013	.1077	1.0	7.983±.024	.0344	2.0
4.568±.013	.1080	1.0	8.183±.024	.0319	2.0
4.770±.014	.1000	1.0	8.383±.025	.0293	2.0
4.971±.015	.0906	2.0	8.584±.025	.0233	2.5
5.171±.015	.0885	1.0	8.784±.026	.0241	2.5
5.372±.016	.0843	1.0	8.984±.027	.0207	2.5
5.572±.016	.0796	1.0	9.186±.027	.0206	2.5
5.773±.017	.0782	1.0	9.385±.028	.0194	2.5
5.973±.018	.0733	1.0	9.585±.029	.0186	2.5
5.978±.018	.0700	1.0	9.786±.029	.0169	3.0
6.174±.018	.0693	1.0	9.986±.030	.0152	3.0

See text, p. 22.

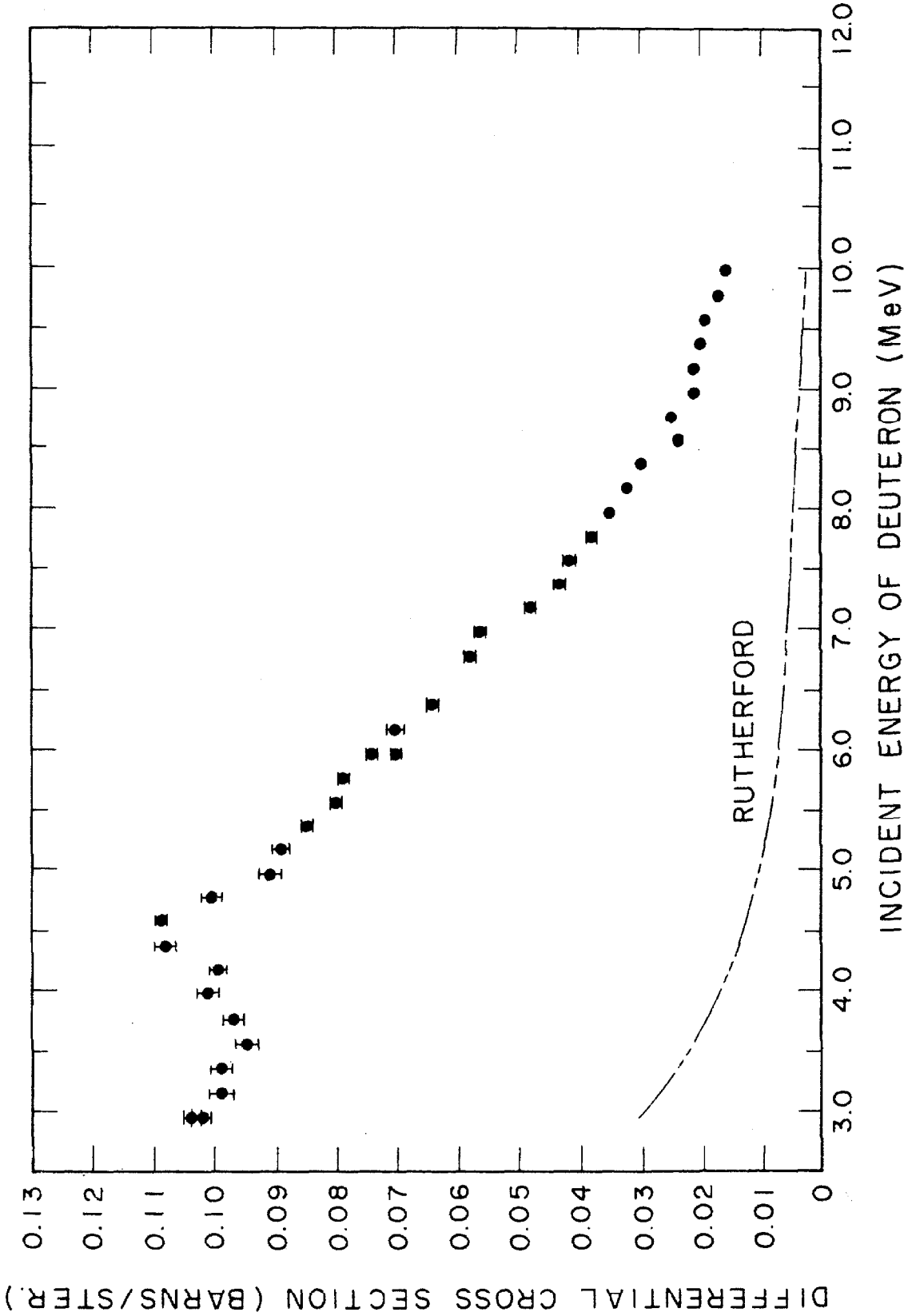
DIFFERENTIAL CROSS SECTION (BARNS/STER.)
0.13
0.12
0.11
0.10
0.09
0.08
0.07
0.06
0.05
0.04
0.03
0.02
0.01
0
3.0
4.0
5.0
6.0
7.0
8.0
9.0
10.0
11.0
12.0
INCIDENT ENERGY OF DEUTERON (MeV)
RUTHERFORD

Figure 39. Differential cross-section in the center of mass vs. energy of incident deuteron at 89.94 ± 0.14° c.m. Data of Galonsky et al. (1955) at 90.1° c.m. is represented by ◇ .

Energy (MeV)	Experiment σ(θ) (mb/sr)	rms error (percent)	Energy (MeV)	Experiment σ(θ)	rms error (percent)
2.958±.009	.0716	5.5	6.379±.019	.0595	2.5
3.159±.009	.0691	5.5	6.580±.020	.0586	2.5
3.361±.010	.0650	4.5	6.780±.021	.0627	2.0
3.562±.011	.0543	5.5	6.981±.021	.0615	2.5
3.764±.011	.0542	4.0	7.181±.022	.0627	2.5
3.965±.012	.0486	5.0	7.382±.022	.0616	2.5
4.166±.012	.0465	5.5	7.582±.023	.0627	2.0
4.367±.013	.0513	4.5	7.783±.023	.0642	2.0
4.568±.013	.0573	4.0	7.983±.024	.0651	2.0
4.770±.014	.0609	4.0	8.183±.024	.0622	2.0
4.971±.015	.0614	3.5	8.383±.025	.0614	2.5
5.171±.015	.0635	2.5	8.585±.025	.0646	2.0
5.372±.016	.0601	3.0	8.784±.026	.0626	2.0
5.572±.016	.0610	2.5	8.984±.027	.0620	3.0
5.773±.017	.0581	2.5	9.186±.027	.0634	2.0
5.973±.018	.0565	2.5	9.385±.028	.0623	2.0
5.978±.018	.0545	3.5	9.585±.029	.0643	2.0
6.174±.018	.0575	2.0	9.786±.029	.0635	2.0
6.179±.019	.0577	3.0	9.986±.030	.0632	2.0

See text, p. 21.

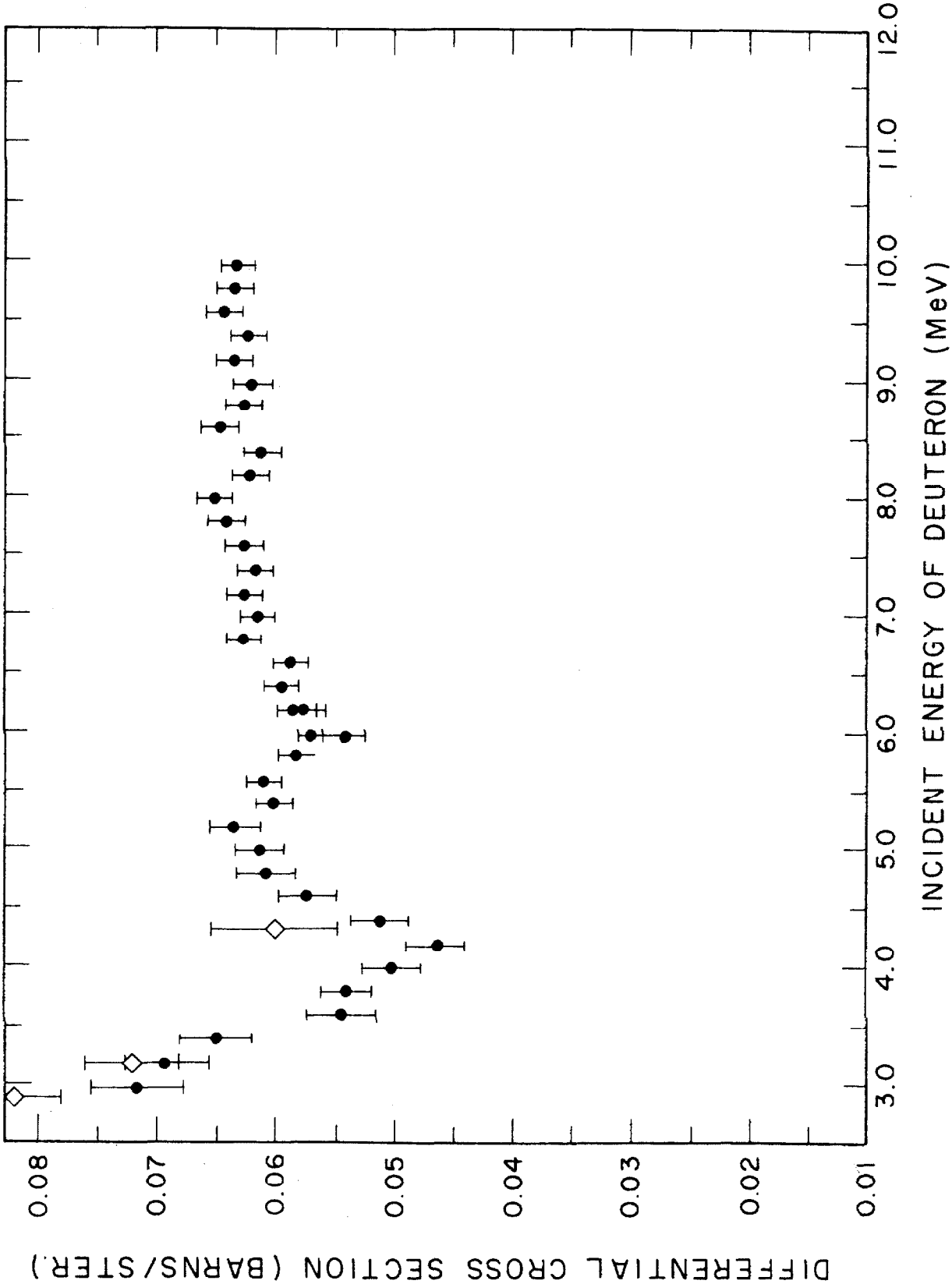
DIFFERENTIAL CROSS SECTION (BARNS/STER.)
0.08
0.07
0.06
0.05
0.04
0.03
0.02
0.01
3.0
4.0
5.0
6.0
7.0
8.0
9.0
10.0
11.0
12.0
INCIDENT ENERGY OF DEUTERON (MeV)

Figure 40. Differential cross-section in the center of mass vs. energy of incident deuteron at $90.0 \pm 0.14°$ c.m., represented by ◇ and $91.95 \pm 0.14°$ c.m., represented by • . The values of the cross-sections are tabulated in the captions of Figures 18 through 36. The error bars plotted are the absolute instead of the relative errors listed in Figures 18 through 36.

See text, p. 21.

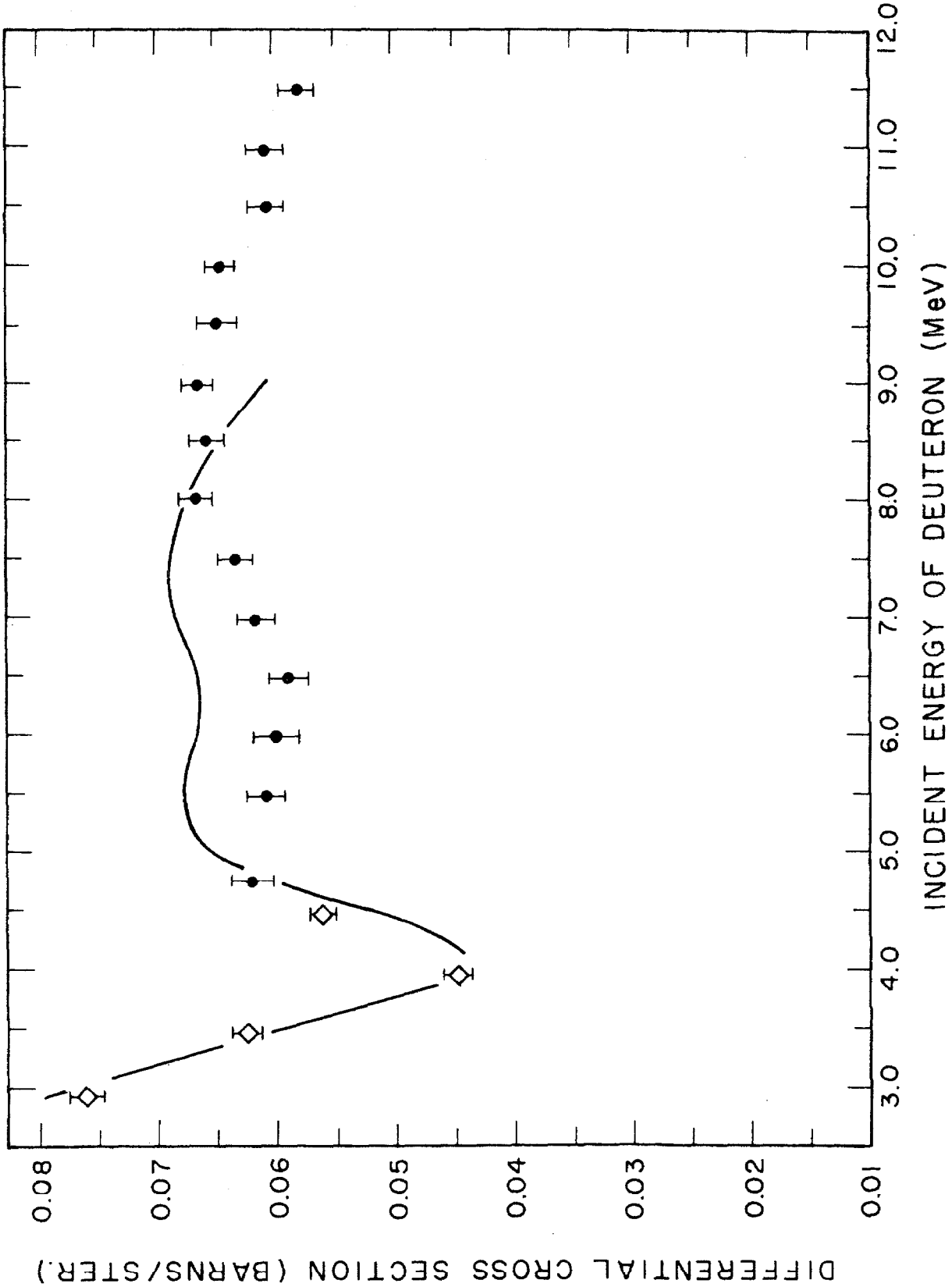
DIFFERENTIAL CROSS SECTION (BARNS/STER.)
0.08
0.07
0.06
0.05
0.04
0.03
0.02
0.01
3.0
4.0
5.0
6.0
7.0
8.0
9.0
10.0
11.0
12.0
INCIDENT ENERGY OF DEUTERON (MeV)

Figure 41. Differential cross-section in the center of mass vs. energy of incident deuterons at $130.0 \pm 0.14°$ c.m. The values of the cross-sections are tabulated in the captions of Figures 18 through 36. The error bars plotted are the absolute instead of the relative errors listed in Figures 18 through 36. Data of Stewart et al. (1962) at 129.9° and 130.0° c.m. are represented by ◇ . See text, p. 21.

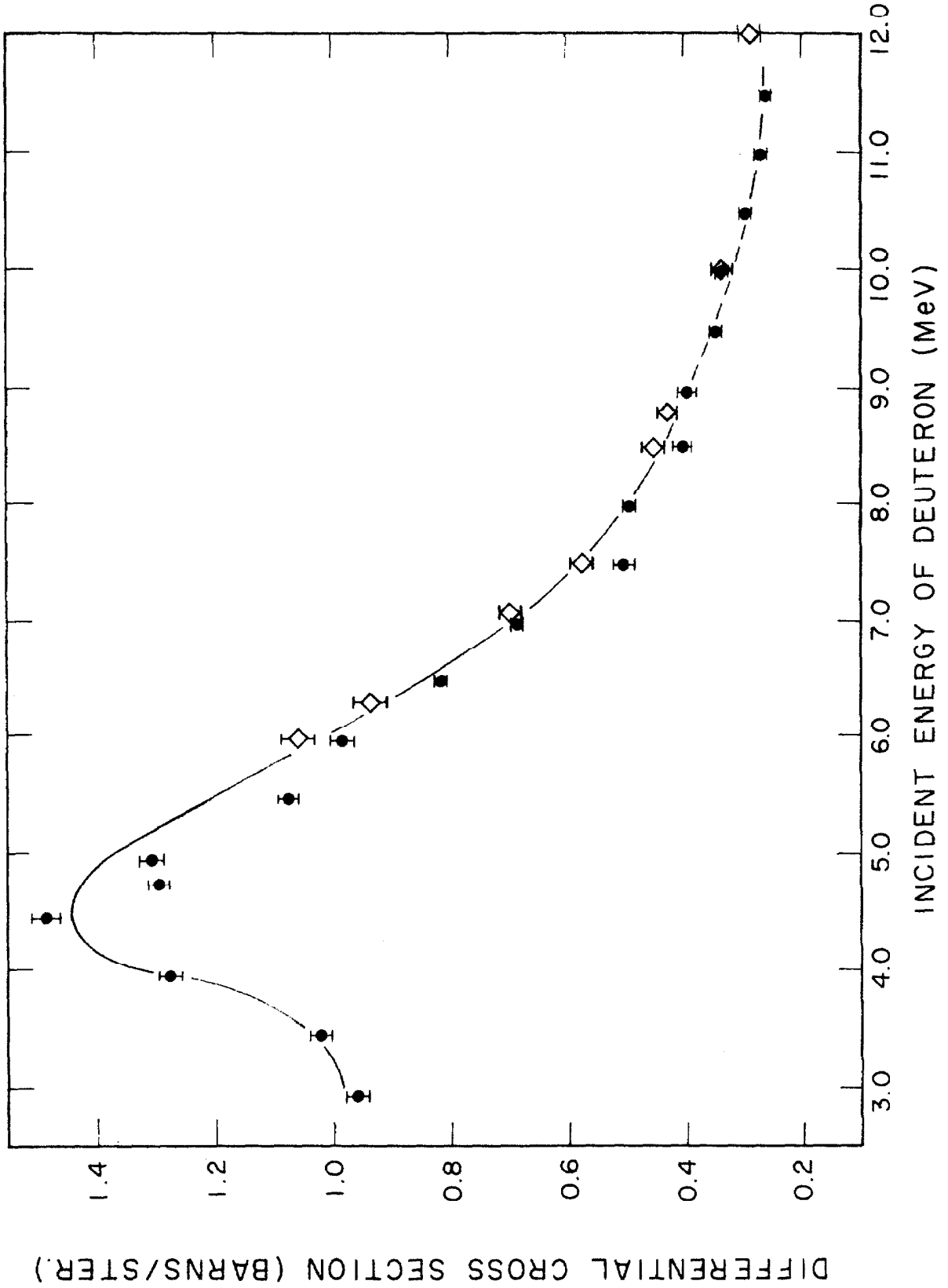
DIFFERENTIAL CROSS SECTION (BARNS/STER.)
0.2
0.4
0.6
0.8
1.0
1.2
1.4
INCIDENT ENERGY OF DEUTERON (MeV)
3.0
4.0
5.0
6.0
7.0
8.0
9.0
10.0
11.0
12.0

Figure 42. Differential cross-section in the center of mass vs. energy of incident deuterons at 156.0 $\pm$ 0.14° c.m. The values of the cross-sections are tabulated in the captions of Figures 22 through 36. The error bars plotted are the absolute instead of the relative errors listed in Figures 22 through 36. See text, p. 21.

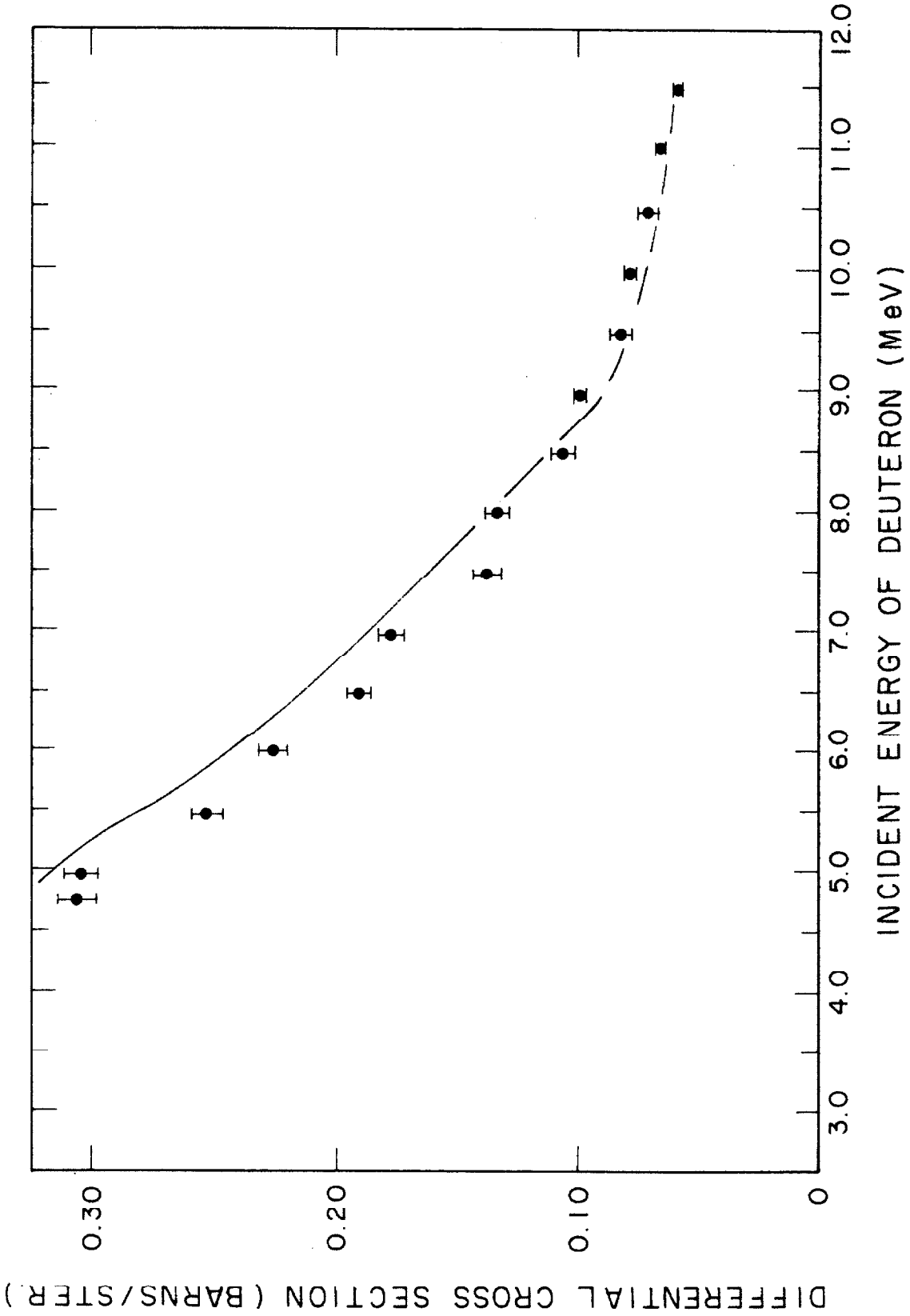
DIFFERENTIAL CROSS SECTION (BARNS/STER)
0
0.10
0.20
0.30
INCIDENT ENERGY OF DEUTERON (MeV)
3.0
4.0
5.0
6.0
7.0
8.0
9.0
10.0
11.0
12.0